Practical review & application of CFD to condensing multiphase flows in geometries relevant to Plate Heat Exchangers

L.B. van den Hoek

Technische Universiteit Delft

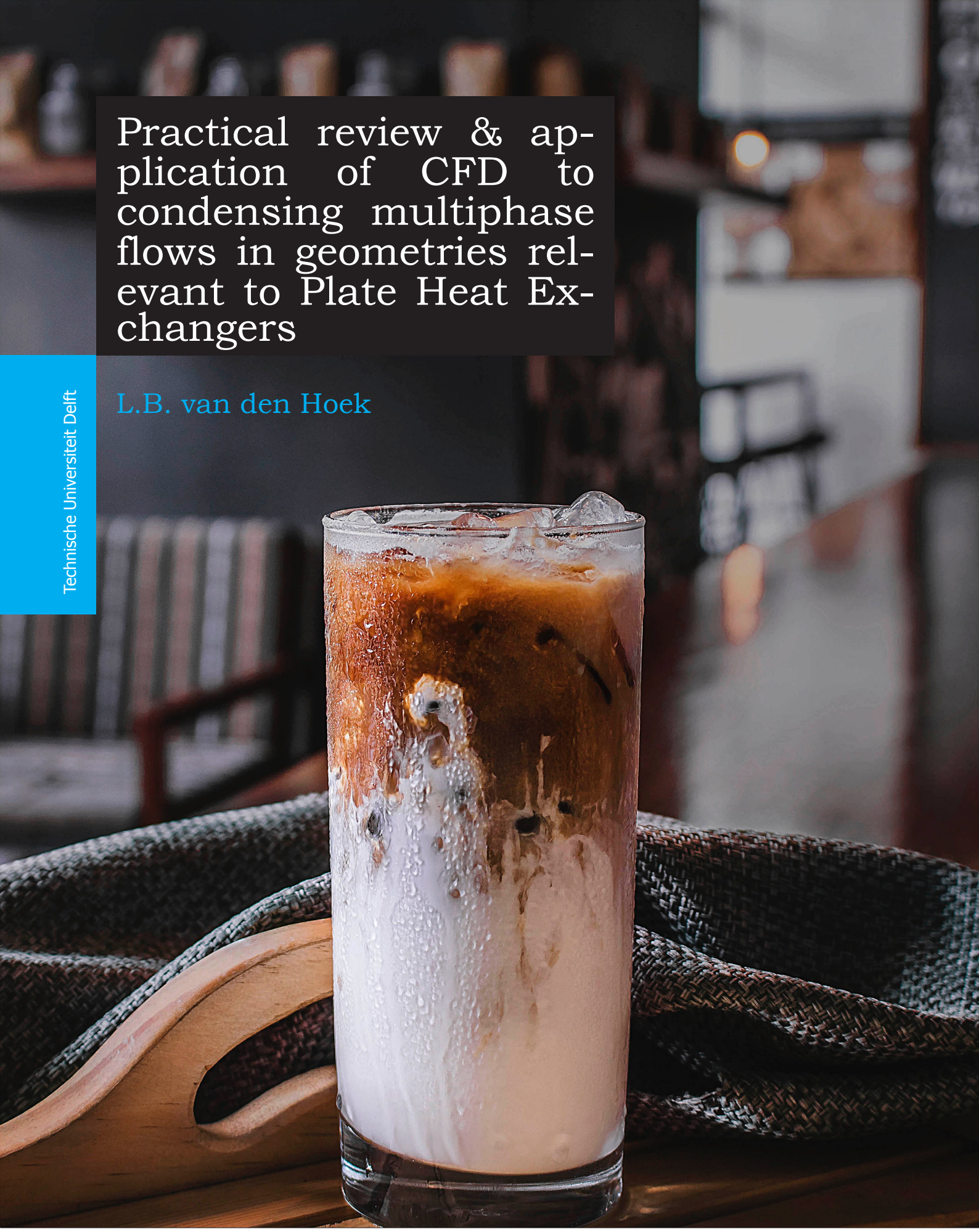

TU Delft Delft University of Technology

Challenge the future

Practical review & application of CFD to condensing multiphase flows in geometries relevant to Plate Heat Exchangers

by

L.B. van den Hoek

in partial fulfillment of the requirements for the degree of

Master of Science
in Mechancial Engineering

at the Delft University of Technology,
to be defended publicly on Monday August 27, 2018 at 15:00 PM.

Supervisor:	Dr. ir. M.J.B.M. Pourquie	
Thesis committee:	Prof. dr. ir. J. Westerweel,	TU Delft
	Dr. ir. B.W. van Oudheusden,	TU Delft
	Dr. ir. C.A. Infante Ferreira,	TU Delft
	Ir. J. Kirkenier,	Bluerise B.V.

This thesis is confidential and cannot be made public until August 27, 2023.

An electronic version of this thesis is available at http://repository.tudelft.nl/.

P&E report number 2902

TU Delft Delft University of Technology

Abstract

In the quest for renewable energy for tropical islands, Ocean Thermal Energy Conversion (OTEC) has revealed itself as one of the most promising technologies. OTEC stands or falls with the performance of the condenser. Plate Heat Exchangers (PHEs) have proven their selves as effective heat transfer equipment for low enthalpy cycles such as OTEC. Nowadays, the design of PHEs mostly relies on models based on experimental data. This is deemed time-consuming and non-generic. Enormous successes in the application of Computational Fluid Dynamics to single-phase flows have raised the interest to use CFD as a predictive and generic tool for the design of PHEs. Moreover, CFD yields a picture of the complete flow field, enabling the designer to better understand the fundamental flow structures that are relevant for the heat transfer and pressure drop performance of the PHE.

First, a comprehensive review of literature on condensation models is presented. Thereafter, the practicality of the phase change models in terms of real computation time needed is investigated. It is concluded that the stability issues associated with the vapor-liquid interface poses the biggest problem. That is, for the simple Nusselt condensation problem, an extremely long computation time is needed for reasonable accuracy. Finally, the ability of the phase change models to cope with wave evolution, flow circulation and flow separation is investigated. The multiphase model is found to properly predict the flow field. However, the heat and mass transfer predicted by the condensation models is estimated poorly.

In the end, until the stability issues of the current phase change models are solved, or a significant improvement in computational performance is made, the application of CFD to the design of condensation PHEs is questionable. Yet, using CFD only to find trends in heat transfer and pressure drop in PHEs might prove to be fruitful.

Contents

List of Figures

List of Tables

Nomenclature

Acronyms

Symbol	Description	Units
CBC	Convective Boundedness Criterion	-
CFD	Computational Fluid Dynamics	-
CICSAM	Compressive Interface Capturing Scheme for Arbitrary Meshes	-
CIP	Constrained Interpolation Method	-
CL-VOF	Coupled Level Set Volume Of Fluid	-
CPU	Central Processing Unit	-
CSF	Continuum Surface Force	-
CSS	Continuum Surface Stress	-
DA	Donor Acceptor	-
DDS	Downwind Difference Scheme	-
GPU	Graphics Processing Unit	-
HKS	Hertz-Knudsen-Schrage	-
HRIC	High Resolution Interface Capturing scheme	-
HTC	Heat Transfer Coefficient	-
LS	Level Set	-
NVD	Normalized Variable Diagram	-
ORC	Organic Rankine Cycle	-
OTEC	Ocean Thermal Energy Conversion	-
PF	Phase Field	-
PHE	Plate Heat Exchanger	-
PLIC	Piecewise Linear Interpolation Calculation	-
QUICK	Quadratic Upstream Interpolation for Convective Kinematics	-

UDF	User Defined Function	-
UDS	Upwind Difference Scheme	-
VOF	Volume Of Fluid	-
VP	Velocity Profile	-

Greek Symbols

Symbol	Description	Units
α	Volume fraction	-
$\alpha_{thermal}$	Thermal diffusivity	kg/m^3
δ	Liquid film thickness	m
δ'	Liquid film thickness corrected for vapor velocity	m
δ^*	Dimensionless film thickness	-
δ_p	Thermal penetration depth	m
δ_{max}	Maximum theoretical film thickness	m
δ_{Nu}	Theoretical Nusselt thickness	m
Γ	Mass flow rate per unit width	kg/sm
γ_{con}	Condensation coefficient	-
γ_{ev}	Evaporation coefficient	-
κ	Interface curvature	m^{-1}
λ	Wave length	m
μ	Dynamic viscosity	Pas
ν	Kinematic viscosity	m^2/s
ϕ	Arbitrary variable	-
σ	Surface tension constant	n/m
τ	Shear stress	n/m^2
θ	Angle	°
ρ	Density	kg/m^3

Roman Symbols

Symbol	Description	Units
$\dot{m}$	Mass transfer rate per unit volume	kg/m^{3}s
$\dot{m}'$	Mass flow rate	kg/s

$\dot{m}''$	Mas transfer rate per unit area	kg/m^2s
$\dot{q}$	Volumetric heat flow	J/m^3s
$\overline{h}$	Mean heat transfer coefficient	W/m^2K
$\vec{n}$	Normal vector	-
$\vec{q}''$	Heat flux vector	J/m^2s
a_c	Accommodation coefficient	-
a_i	Interfacial area density	m^2/m^3
B	Baffle height	m
b	Per unit width b	m
C	Velocity	m/s
C_p	Heat capacity	J/gK
Ca	Dimensionless Capillary number	-
D	Normal component of interface velocity	m/s
D_{sm}	Sauter mean diameter	m
f	Frequency	Hz
f'	Dimensionless frequency	-
f_0	Relaxation coefficient in the modified Lee model by Chen	$s^{-1}K^{-1}$
F_{vol}	Force per unit volume	n/m^3
g	Gravitational constant	m/s^2
h	Local heat transfer coefficient	W/m^2K
h'	Local heat transfer coefficient corrected for vapor velocity	W/m^2K
h'_{fg}	Latent heat corrected for thermal advection	J/kgK
h_{fg}	Enthalpy of phase change	J/kg
J	Mass transfer rate per unit area	kg/m^2s
Ja	Dimensionless Jakob number	-
K	Surface wave speed	cm/s
k	Thermal conductivity	W/mK

k_b	Boltzmann constant	J/K
M	Molar mass	g/mol
Nu_0	Film Nusselt number based on surface velocity	-
Nu_δ	Film Nusselt number based on bulk velocity	-
p	Pressure	N/m^2
Pe	Dimensionless Pecklet number	-
Pr	Dimensionless Prandtl number	-
q	Heat flux	W/m^2
R	Universal gas constant	J/molK
r	Relaxation coefficient in the Lee model	s^{-1}
Re_0	Film Reynolds number based on surface velocity	-
Re_δ	Film Reynolds number based on bulk velocity	-
Re_{tr}	Transition Reynolds number	-
S	Mass source term in continuity equation	kg/m^3s
S_E	Energy source term in energy equation	J/m^3s
T	Temperature	K
t	Time	s^{-1}
t^*	Dimensionless time	-
u	Velocity in x-direction	m/s
u'_w	Dimensionless surface wave speed from correlation	cm/s
u^*	Dimensionless velocity	-
u_w	Surface wave speed from correlation	cm/s
u_{max}	Maximum surface velocity at maximum theoretical film thickness	m/s
v	Velocity in y-direction	m/s
V_{cell}	Volume of computational cell	m^3
w	Velocity in z-direction	m/s

We	Dimensionless Weber number	
We_0	Film Weber number based on surface velocity	-
We_δ	Film Weber number based on bulk velocity	-
x^*	Dimensionless x-location	-

Subscripts

Symbol	Description	Units
b	bulk	-
con	Condensation	-
ev	Evaporation	-
i	Interface	-
l	Liquid phase	-
lv	From the liquid phase to the vapor phase	-
n	Normal component	-
sat	Saturated	-
suf	Surface	-
uns	Unsaturated	-
v	Vapor phase	-
vl	From the vapor phase to the liquid phase	-

1

Introduction to OTEC & Research Justification

1.1. Ocean Thermal Energy Conversion

Ocean Thermal Energy Conversion (OTEC) has emerged as one of the most promising technologies to supply tropical islands of renewable energy. As diesel generated energy is relatively more costly on islands than conventional energy sources on the main land, OTEC can be developed into a profitable and clean alternative to diesel generated electricity. Compared to other renewable energy technologies, OTEC is able to generate a so-called *baseload* energy (around the clock energy without big fluctuations) [15]. In addition, the total surface area needed for an OTEC plant is considerably less compared to either energy from sun or wind. Also, typically the sea surrounding tropical islands is deep, making it unsuitable for conventional non-floating wind parks. For OTEC it is the other way around. Namley, OTEC needs a deep sea to extract it's cold water from. Therefore islands with deap surrounding waters are extra suitable for OTEC.

Figure 1.1 shows the basic OTEC cycle. One may notice that it is very similar to a normal Rankine cycle. However, the boiler and condenser are replaced by two heat exchangers. Moreover, the working fluid is characterized by a low saturation temperature. The kind of working fluid normally used in refrigeration cycles is of an organic nature. Therefore, this cycle is also referred to as the Organic Rankine Cycle (ORC). The main advantage of an ORC compared to a water-steam Rankine cycle is it's capability of recovering heat from relatively low temperature sources. These low temperature sources are normally referred to as low enthalpy energy sources. Examples of low enthalpy energy sources are geothermal energy, bio-combustion waste heat and *ocean energy*.

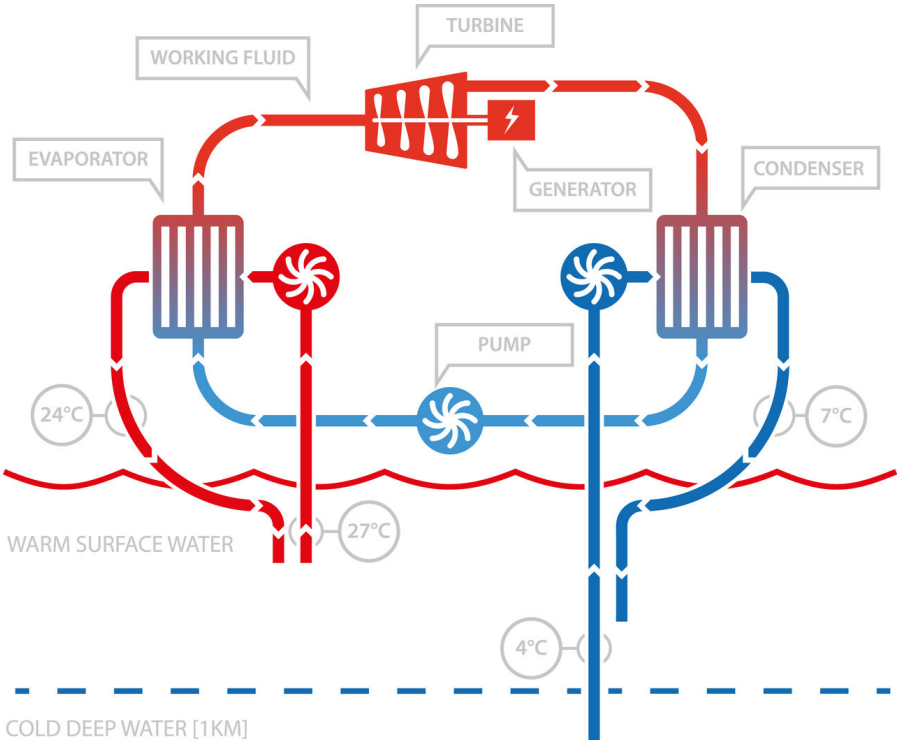

Figure 1.1: Basic OTEC cycle, from [1]

The tropical oceans are characterized by relatively high surface temperatures, while low temperature water is available at a depth of around one kilometer. The ORC is capable of using this temperature difference to generate energy. By using high temperature surface water, the organic working fluid is vaporized and (partly) superheated in the evaporator. Next, the vapor is directed to the turbine where it is expanded, and, by doing so, energy is extracted and converted to electrical energy in the generator. The saturated vapor is sent to the condenser where cold sea water is used to extract energy from the vapor and generate a phase change. Finally, the liquid working fluid is pumped to the evaporator and the cycle starts all over again. In summary, the ocean's temperature difference is the driving force for the entire OTEC cycle. Therefore, the heat exchangers used to extract the ocean's energy are of utmost importance to the cycle's efficiency.

1.2. The condenser

Almost forty percent of the total cost on an OTEC plant is due to the heat exchangers [16], where the costs of both heat exchangers costs are more or less equal. However, since the condenser uses sea water from one kilometer of depth, condenser performance is very important for sizing of the cold water pipe. Therefore, the costs of the cold water pipe is directly related to the condenser performance. Meaning that condenser optimization yields a very big potential in cost savings.

In other low enthalpy applications as geo-thermal energy or waste heat energy, it is the other way around. The performance of the evaporator is the leading factor in cost savings for the power plant. Since most low enthalpy applications have an evaporator-driven design, most research has been directed into boiling models.

So, from the OTEC point of view, it is most interesting to look into condenser performance and optimization. Additionally, since research has mostly been directed to the evaporator, the academic challenge will be big.

Basic principle

After the vapor is ideally fully expanded in the turbine, the vapor is directed towards the condenser. Condensation is needed to increase the working fluid's density. Due to the higher density of a liquid, far less work is required to transport the working fluid through the system. When the expanded vapor reached the condenser, the relatively lower condenser wall temperature cools the vapor. At some point,

the vapor temperature drops below it's *saturation temperature* and parts of the vapor molecules will stick together and start to form liquid droplets on the cooling surface. So-called *dropwise condensation* is the preferred type of condensation, since high heat transfer is obtained. However, in practice it is very hard to sustain dropwise condensation. As more vapor molecules impinge into the droplets, the droplets will grow until eventually a liquid film is formed. After a while the cooling wall is fully wetted and the heat transfer will be governed by the liquid film: so-called *filmwise condensation*. The liquid on the wall increases the heat transfer resistance between the vapor and the cooling wall, therefore when the wall is fully wetted the heat transfer will be less compared to dropwise condensation. Because dropwise condensation is hard to sustain, and is rather unpredictable, condensers designed for general purposes are mainly focused on filmwise condensation [17][18].

Depending on the quality and speed of the mixture, several flow regimes can be distinguished. These flow regimes will be thoroughly discussed in section 1.2.1. However, as is pointed out in literature *filmwise condensation* will be of most interest to industrial condensers.

Condensers for OTEC

Compared to the classical Rankine cycle where large temperature differences between the working fluids are available, the OTEC cycle is characterized by low enthalpy differences in the evaporator and condenser. As a consequence, condensers should be designed accordingly. For instance, the heat transfer per square meter is relatively lower for low enthalpy systems compared to high enthalpy systems. The effective cooling surface of the condenser can be increased to obtain the same heat transfer capabilities as high enthalpy systems. A large benefit of plate heat exchangers compared to shell and tube heat exchangers is the larger heat exchanging surface. Therefore, in organic Rankine cycle applications, mainly PHEs are employed [19]. Moreover, PHEs are easier to maintain than shell and tube heat exchangers, while they are also less prone to fouling [18]. Particularly being less prone to fouling is important since the PHEs used in OTEC will be subjected to highly contaminated sea-water.

Plate heat exchanger design

Condenser performance is mainly governed by the heat transfer capabilities of the condenser and the accompanying pressure drop across the condenser. For fully laminar film condensation Nusselt derived an analytic solution for the heat transfer across the film. In this solution, the heat transfer is entirely governed by the liquid film resistance, or so to say, by conduction. A linear temperature profile exists which can be described by Fourier's law. However, when flow rate is increased, the laminar flow regime will become turbulent. As turbulence is characterized by three-dimensional flow structures, the analytic Nusselt solution is not applicable anymore. Moreover, other flow phenomena as circulation and vortex shedding come into play. As turbulence enhances the heat transfer, the turbulent flow regime is preferred. As no analytic solution is available, heat transfer and pressure drop is mainly predicted by the fitting of experimental correlations. In the work of Garcia [20], it is pointed out that already in the modeling of single phase flow PHEs the available correlations are only applicable to a specific geometry. The large amount of combinations of geometrical parameters makes it impossible to develop a general correlation theory for the design of PHEs. For a thorough assessment of heat transfer and pressured drop correlations in PHEs, the reader referred to the work of Garcia.

1.2.1. Flow Regime

The so-called *flow regime* or *flow pattern* represents the geometrical and topological configuration of the interface between the vapour and liquid phase. Making a distinction between flow regimes helps us to describe the fundamental processes in an heat exchanger. Both heat transfer and pressure drop are directly related to the geometrical configuration of the flow. As pointed out previously, the film that forms on the wall during filmwise condensation is the main obstruction to heat transfer in laminar flow. Being able to relate other than laminar heat transfer characteristics to certain flow regimes will be of high value. But, before one can relate heat transfer characteristics to flow regimes, one should know what flow regimes exist in heat exchanges, and what defines them. The research into flow regime during condensation has mainly been focused on condensation in vertical and horizontal tubes. Therefore, first a review of flow structures present in tubes during condensation is conducted. After, the available literature of condensation in plate heat exchangers is reviewed. Finally, the flow regime of most interest will be presented.

Tubes - Vertical Upflow

According to Yadigaroglu & Hewitt [2], five main flow regimes in vertical upflow tubes can be distinguished. Namely: Bubbly flow, Slug flow, Churn Flow, Annular flow and Wispy annular flow. While according to Thome [21], also Mist flow should be considered.

- *Bubbly flow*: Bubbly flow is characterized by discrete gas bubbles dispersed in the continuous liquid phase. Different sizes may be observable, but their size is always smaller than the pipe diameter.
- *Slug flow*: As the void fraction increases and multiple bubbles coalesce, the slug flow pattern can be witnessed. The coalesced bubbles form the typical shape some refer to as a bullet. As the diameter of the bullet is almost the same as the tube diameter only a small liquid film is present between the bullet and the tube wall.
- *Churn flow*: When slug flow becomes unstable due to a velocity increase, the slugs break up and churn flow will develop. The instability is caused by a balance between the shear force and the gravitational force acting on the liquid film in opposite direction. Churn flow also characterizes a transition between a flow where gas and liquid are axially separated to a flow where gas and liquid are radially separated.
- *Annular flow*: Annular or film flow is developed when the shear force on the liquid film starts to dominate the gravitational force and therefore pushes all liquid to the outer region. A further increase in velocity causes large amplitude waves at the liquid-gas interface. The waves may break-up and form little bubbles that move into the core, are driven out again and redeposit on the film.
- *Wispy annular flow*: Again an increase in gas velocity causes the flow pattern to change. Due to the amplitude waves more droplets will dispatch from the liquid film and form transient coherent structures also known as wisps.
- *Mist flow*: Very high gas flow induces a high shear on the liquid film until it becomes unstable and subsequently destroyed.

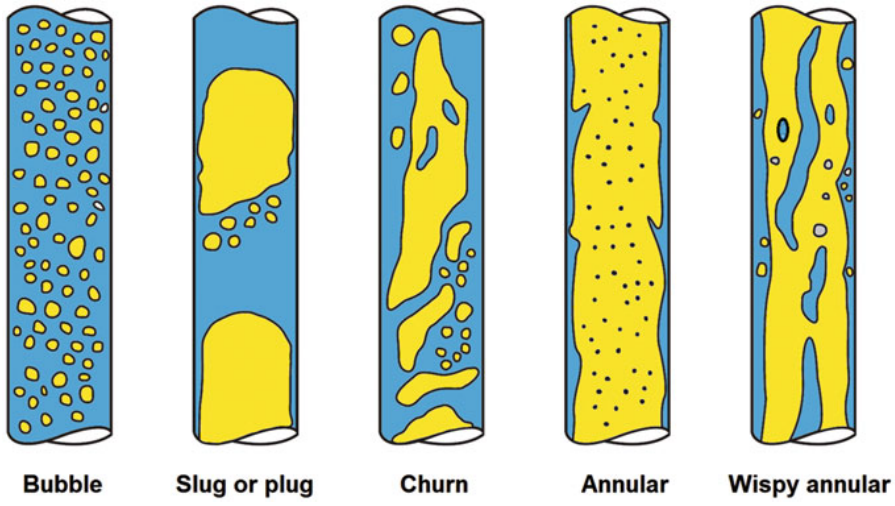

Figure 1.2: Schematic visualization of flow regimes in vertical upflow, from [2].

Tubes - Horizontal Flow

The flow patterns in horizontal flow will be different than the ones in vertical upflow. The apparent reason is the change in the effect of the gravitational force. For instance, the gravitational force causes the liquid and gaseous phase to separate in a way that the liquid is in the bottom part of the tube and the gas in the upper part. This is also referred to as *stratified flow*. As the velocity of the gas increases and the inertial forces start to dominate the gravitational forces, the gravitational effect will become less important and the flow patterns will be similar to those of vertical flow.

- *Bubbly flow*: Bubbly flow is still characterized by discrete bubbles dispersed into a continuous liquid phase. However, due to buoyancy, more bubbles will be present in the upper half of the tube.

- *Stratified flow*: Stratified flow is characterized by a complete separation of the liquid and gas phase, with the liquid in the bottom part of the tube. This flow regime is mainly witnessed at low flow rates. When the flow rate increases, the interface will become wavy.

- *Plug flow*: Plug flow occurs when the flow rate is relatively small and elongated bubbles form in the upper part of the tube. The liquid phase stays continuous along the bottom part of the tube. Plug flow is also referred to as *elongated bubble flow*.

- *Slug flow*: Due to a velocity increase, the flow becomes more chaotic causing gas bubbles to be dispersed throughout the liquid phase while also liquid bubbles will be present in the gaseous phase.

- *Annular flow*: At high velocities the tube core will be dominated by gas while a liquid film will form on the tube wall. The main difference with annular flow in vertical tubes is that the liquid film in the bottom part will be thicker than in the top part.

- *Mist flow*: At very high velocities, all liquid will detach from the wall and form a mist throughout the tube. Similar as in vertical upflow

Tubes - Vertical Downflow

Compared to vertical upflow and horizontal flow, less work has been done to investigate the flow regime in vertical downflow. However, according to [22] and [23] , the flow regimes show similar behavior as in vertical upflow and can be divided into bubble, annular, plug, and churn flow. [22] stated that at high flow rates also *mist flow* can be observed. Finally, [23] mentions the existence of *falling film flow*, where films move along the wall and gently flow over one another as sheets. According to Gou et all [24], the condensation of pure downflow starts from the annular flow regime. This regime is characterized by a thin liquid film that flows on the pipe surface while the vapor flows in the core region. Also it is stated that a transition from laminar to turbulent film flow occurs when the thickness of the film increases.

Flow regime in PHEs

While the two-phase flow regime in tubes has has been thoroughly investigated, much less work has been done in plate heat exchangers (PHEs). One of the first steps towards flow visualization in PHEs has been done by Focke and Knibbe [25]. They studied the flow path of a one-phase liquid flow in parallel-plate ducts with corrugated walls. It was concluded that at high chevron angles the flow will continue to the side walls (unidirectional flow), while at lower angles the flow is reflected at the crossing furrow (helical flow). The main reason for the reflection presented in the paper is the high interaction level between the main flow and the flow in the crossing furrow. Later, Gaiser & Kottke [26] show similar results. The first step towards qualitative flow regime definition was made by Gradeck & Lebouché [27]. They did a flow visualization study of a two-phase gas liquid flow in horizontal corrugated channels. The working fluids they used were water and nitrogen. In the end they identified two main flow regimes: for low liquid mass fluxes the stratified flow regime was observed, while for greater mass fluxes they witnessed the bubbly flow regime. The work of Tribbe & Muller-Steinhagen [28] is particularly interesting. They were the first to investigate the flow patterns in an industrial type PHE. In this paper five different flow patterns are proposed and described in order of increasing gas flow rate: regular bubbly flow, irregular bubbly flow, churn flow, film flow, and partial film flow. In more recent work by Tao et al (2017) [29], a comprehensive overview of multiphase downward vertical flow patterns present in plate heat exchangers is given. In this paper, four main flow regimes are distinguished: bubbly flow, slug flow, churn flow and film flow. The four flow regimes are depicted from left to right in Figure 1.3.

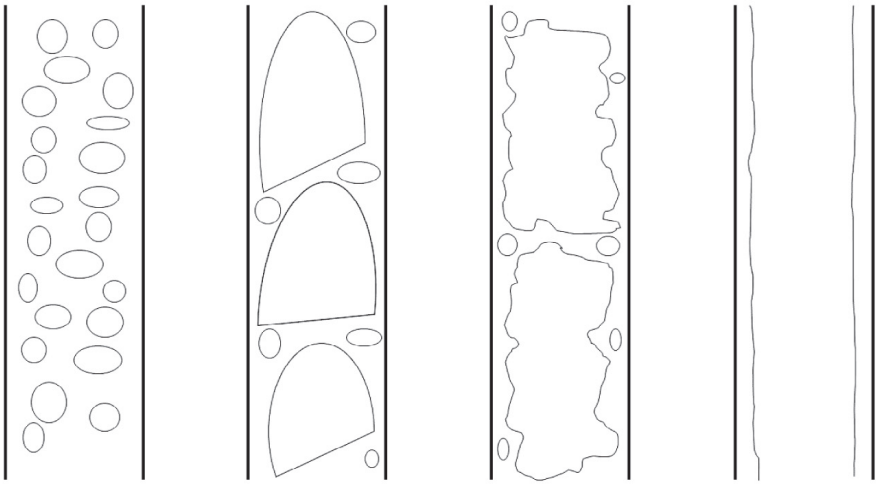

Figure 1.3: Four main flow regimes in downward two-phase flows in PHEs. From left to right: bubbly flow, slug flow, churn flow and film flow.

Flow regime consideration

As one can imagine, the widely varying flow regimes pose many different problems in terms of numerical modeling. For this reason, modeling of a full PHE should be taken step by step. As will become clear later on in this report (see Section 3.5), condensation phase change modeling is still in it's "infancy". As many authors focus on the modeling of the falling film flow regime, in this work this flow regime will also be taken as a starting point. Moreover, as continuous dropwise condensation is very hard to sustain, most condensers are designed under the assumption of film-wise condensation [17]. This also attributes to the consideration of modeling filmwise condensation.

1.3. Research Focus

Developing case-specific correlations for condenser design has been proven very time consuming. In addition, the correlation restricts the designer to work within a certain set of geometrical parameters. While the restrictions to condenser design using correlations are very apparent, no real alternative has presented itself yet. From a practical point of view, a designer wants to have a model at his disposal that is capable of modeling any condenser configuration. This means being able to change geometrical parameters as well as inlet and outlet conditions or working fluids. In other words, we are looking for a *generic* way of modeling.

A model can only be generic when the leading physics are described in a fundamental manner. One approach to fundamental modeling is so-called Computational Fluid Dynamics (CFD). In CFD, the model aims to numerically solve the fundamental equations of flow, heat and mass transfer. By doing so, the model will not only be generic, but also the complete solution of the flow field will be known to the designer. Imagine that you know exactly what a flow is doing up to the millimeter or micrometer scale. New insights in condenser design may be developed, and optimization will be easy.

So what is the status quo in CFD modeling in general, and in particular to condenser modeling? These are the first two questions that need to be answered. Chapter 2 will be devoted to the basic concepts of multi-phase modeling. That is, the numerical models available in the software package Fluent will be discussed. Hereafter, chapter 3 will focus on one of the most challenging aspects of this topic: phase change. Available phase change models will be discussed. In addition, a comprehensive review on literature will be presented. Subsequently, findings of chapter 3 will be leading in the next two chapters. In any case, chapters 4 and 5 will assess the state of the art CFD models applied to condenser modeling. The distinction between chapter 4 and 5 is made by focusing chapter four on the practicality of the models, while chapter five will focus on the models' capability of modeling fundamental flow structures and accompanying heat transfer. Finally, chapter 6 will present the overall conclusions & recommendations for future studies.

2

Numerical modeling of multiphase flows

2.1. Introduction

This chapter aims to explain the basic concepts in the modeling of multiphase flows using the commercial soft-ware package Fluent. Other basic models of CFD employed in this work will not be discussed. For an explanation of the basic models, the reader is referred to the Fluent user manual [30] or the Fluent theory guide [3].

2.2. Governing equations

The present work is restricted to the numerical modeling of two-dimensional incompressible condensate film flow with constant fluid properties evaluated at a reference temperature (see section 4.2.2). Two-dimensional film flow can be evaluated as a boundary layer flow (see Appendix B). The governing equations for 2D incompressible film flow are the 2D continuity equation (2.1), the 2D Navier-Stokes equations and the energy equation (2.4) and are taken from [11]:

$$\frac{\partial u^*}{\partial x^*} + \frac{\partial v^*}{\partial y^*} = 0 \tag{2.1}$$

$$\frac{\partial u^*}{\partial t^*} + u^*\frac{\partial u^*}{\partial x^*} + v^*\frac{\partial u^*}{\partial y^*} = -\frac{\partial p^*}{\partial x^*} + \frac{1}{Re_0}\left(\frac{\partial^2 u^*}{\partial {x^*}^2} + \frac{\partial^2 u^*}{\partial {y^*}^2}\right) + \frac{1}{Fr_{x,0}} \tag{2.2}$$

$$\frac{\partial v^*}{\partial t^*} + u^*\frac{\partial v^*}{\partial x^*} + v^*\frac{\partial v^*}{\partial y^*} = -\frac{\partial p^*}{\partial y^*} + \frac{1}{Re_0}\left(\frac{\partial^2 v^*}{\partial {x^*}^2} + \frac{\partial^2 v^*}{\partial {y^*}^2}\right) + \frac{1}{Fr_{y,0}} \tag{2.3}$$

$$\frac{\partial T^*}{\partial t^*} + u^*\frac{\partial T^*}{\partial x^*} + v^*\frac{\partial T^*}{\partial y^*} = \frac{1}{Re_0 Pr}\left(\frac{\partial^2 T^*}{\partial {x^*}^2} + \frac{\partial^2 T^*}{\partial {y^*}^2}\right) \tag{2.4}$$

where u^*, v^*, p^*, x^*, y^*, t^* represent the dimensionless x-velocity, y-velocity, x-distance, y-distance, pressure and time, respectively. The variables are non-dimensionalized using a reference film thickness δ_0 and reference film velocity u_0, according to:

$$x^* = \frac{x}{\delta_0},\ y^* = \frac{y}{\delta_0},\ u^* = \frac{u}{u_0} v^* = \frac{v}{u_0},\ p^* = \frac{p - p_v}{\rho u_0^2},\ t^* = \frac{t}{\delta_0/u_0} \tag{2.5}$$

The dimensionless temperature T^* is non-dimensionalized using the wall temperature T_w and the saturation temperature T_{sat} according to:

$$T^* = \frac{T - Tw}{T_{sat} - Tw} \tag{2.6}$$

The important dimensionless number are the Reynolds number, Froude numbers, Weber number and Prandtl number:

$$Re_0 = \frac{u_0 \delta_0}{\nu_l} \tag{2.7}$$

$$Fr_{x,0} = \frac{u_0^2}{\delta_0 g sin\theta} \tag{2.8}$$

$$Fr_{y,0} = \frac{u_0^2}{\delta_0 g cos(\pi - \theta)} \tag{2.9}$$

$$We_0 = \frac{\rho u_0^2 \delta_0}{\sigma} \tag{2.10}$$

$$Pr = \frac{C_p \mu}{k} \tag{2.11}$$

where μ represents the dynamic viscosity, C_p the specific heat, k the thermal conductivity, σ the surface tension and where θ represents the inclination angle and $\theta = 90°$ corresponds to a vertical plate in alignment with the gravitational acceleration g. When u_0 is considered the film surface velocity, the following relation exists between the surface velocity and the film thickness:

$$u_{s,0} = \frac{g\delta^2 sin\theta}{2\nu_l} \tag{2.12}$$

When u_0 is considered the film bulk velocity, the following relation exists between the surface velocity and the film thickness:

$$u_{b,0} = \frac{g\delta^2 sin\theta}{3\nu_l} \tag{2.13}$$

An alternative version of the film Reynolds number used by Incropera [9] and by Mills[31] is adopted in this work:

$$Re_\delta = \frac{4u_{b,0}\delta}{\nu_l} \tag{2.14}$$

2.3. Governing equations in Fluent

In FLuent [3], the governing equations of mass, momentum and energy are discretized using a fininte volume method. The governing equations are cast in integral Cartesian form for an arbitrary control volume V with differential surface dA according to:

$$\frac{\partial}{\partial t}\int_V W dV + \oint [F - G] \cdot dA = \int_V S dV \tag{2.15}$$

where the vectors W, F and G are defined as follows: $W = \begin{pmatrix} \rho \\ \rho u \\ \rho v \\ \rho w \\ \rho E \end{pmatrix}$ $F = \begin{pmatrix} \rho v \\ \rho vu + p\hat{i} \\ \rho vv + p\hat{j} \\ \rho vw + p\hat{k} \\ \rho vE + pv \end{pmatrix}$ $G = \begin{pmatrix} 0 \\ \tau_{xi} \\ \tau_{yi} \\ \tau zi \\ \tau_{ij} v_j + q_i \end{pmatrix}$

where τ represents the viscous stress tensor, E the total energy per unit mass and q the heat flux. The vector S contains source due to external forces or energy. The total energy E is found with the help of the total enthalpy H:

$$E = H - p/\rho \tag{2.16}$$

$$H = h + \frac{|v|^2}{2} \tag{2.17}$$

2.4. The Volume Of Fluid method

Instead of solving conservation equations for multiple phases, often only one set of conservation equations is solved for the entire flow field. Color functions are employed to reconstruct the interface

between the two phases. The color function is advected by the flow. This way of representing a two-phase flow is also known as the ”one-fluid” method [32]. Well known methods which are based on this principle are the Volume Of Fluid method (VOF), Level Set methods (LS), Coupled Level Set Volume Of Fluid method (CLSVOF), the Phase-Field method (PF) and the Constrained Interpolation method (CIP). Fluent only provides sharp interface modeling with the ability of mass transfer between the phases for the VOF method. Therefore only the VOF method will be discussed.

The VOF method makes use of a color function C to track the interface position. The color function represents the volume fraction α and therefore the color value is between zero and one. Using the color function for the volume fraction allows one to use the material properties in a volume averaged manner:

$$\rho = \alpha_2\rho_2 + (1-\alpha_2)\rho_1 \tag{2.18}$$
$$k = \alpha_2 k_2 + (1-\alpha_2)k_1 \tag{2.19}$$
$$\mu = \alpha_2\mu_2 + (1-\alpha_2)\mu_1 \tag{2.20}$$

Where ρ, k and μ represent the volume averaged density, volume averaged thermal conductivity and volume averaged dynamic viscosity, respectively. For incompressible flow without phase change a simple advection equation for the color function is solved, hence.

$$\frac{\partial}{\partial t}C + \nabla\cdot(\vec{u}C) = 0 \tag{2.21}$$

A major advantage resulting from the use of the color function is its conservative nature.

The VOF method originates from the famous work by Hirt & Nichols[33]. The time evolution of the volume fraction is calculated using the advection equation of 2.21. For the integration of the second term (the advective term) cell-face values of the volume fraction are needed. The determination of these cell-face volume fraction values can be approached in two ways. Either in an *algebraic* approach, or a *geometrical approach*.

In the algebraic approach, the face volume fractions have to be interpolated. The basic scheme for interpolation of the volume fraction face values and subsequently the face volume flux is the so-called Donor Acceptor scheme (DA). In this scheme a ’donor’ cell and an ’acceptor’ cell are identified, as shown in Figure 2.1.

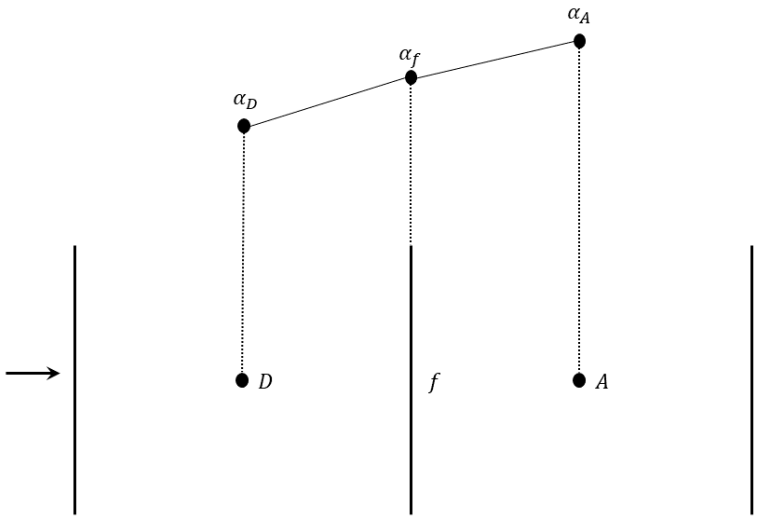

Figure 2.1: Schematic representation of the Donor Acceptor interpolation scheme, Donor cell (left), face (middle) and Acceptor cell (right).

The allocation of donor or acceptor cell is dependent on the normal velocity at the face, i.e. the normal velocity at the face is always pointing from the donor to the acceptor. By introducing the limitation that the accepted volume fraction never exceeds the donated volume fraction or vice versa, the conservation of volume is satisfied. In order to know the maximum volume fraction to be donated, the scheme needs to know the minimum available void to be filled (downwind data). Additionally, the scheme needs to know the maximum amount of volume that is available in the upwind cell. Therefore, the DA-scheme is said to use a combination of upwind and downwind schemes. Nowadays, the classical DA-scheme is considered obsolete, yet this scheme still forms the basis of widely used VOF-discretization schemes as the CICSAM scheme (Compressive Interface Capturing Scheme for Arbitrary Meshes [34]) or HRIC scheme (High Resolution Interface Capturing [35]).

In the geometrical approach, the face volume fluxes are simply calculated using the geometrical data from the reconstructed interface. One way of geometrically inferring the interface is by a Piecewice Linear Interpolation Calculation (PLIC). The exact steps of PLIC are discussed in Section A.1. The physical interface, the interface yielded by the Donor-Acceptor (DA) scheme, and the interface yielded by a Piecewise Linear Interpolation Calculation (PLIC) scheme is shown in Figure 2.2, respectively.

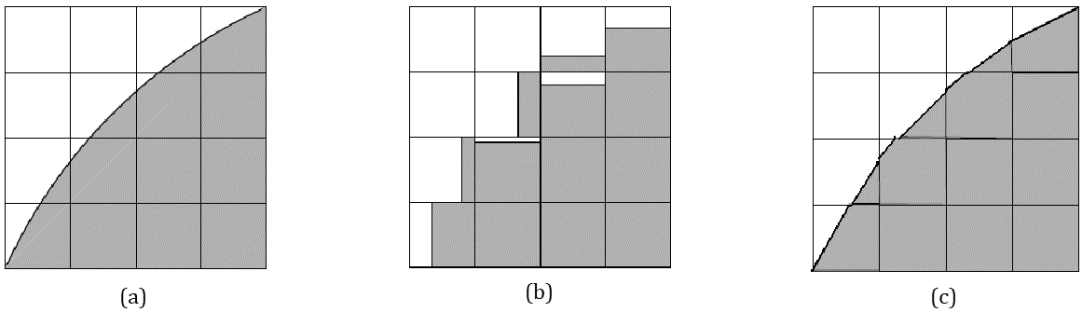

Figure 2.2: (a) Actual interface, (b) Interface representation in DA-schemes, (c) Interface representation by PLIC, from [3]

In addition, Figure 2.3 shows on the left hand side a DA-scheme yielded interface, and on the right hand side a PLIC yielded interface. Due to the discontinuity in the interface yielded by the DA scheme, an interpolation between the two cells is needed to extract the cell face value. In the case of the PLIC scheme, the volume fraction is known at each point on the line. Therefore, also the face volume fraction is known. Thus no interpolation is needed. Due to the interpolation step in the DA scheme no interface reconstruction is needed. The user simply infers the interface position by identifying where the volume fraction equals 0.5. In the geometrical approach, the interface has to be reconstructed in each time step. Appendix A.1 gives a step by step overview of the geometrical interface reconstruction. List 2.1 and List 2.2 show the steps involved during one time step for the algebraic approach and the geometrical approach, respectively.

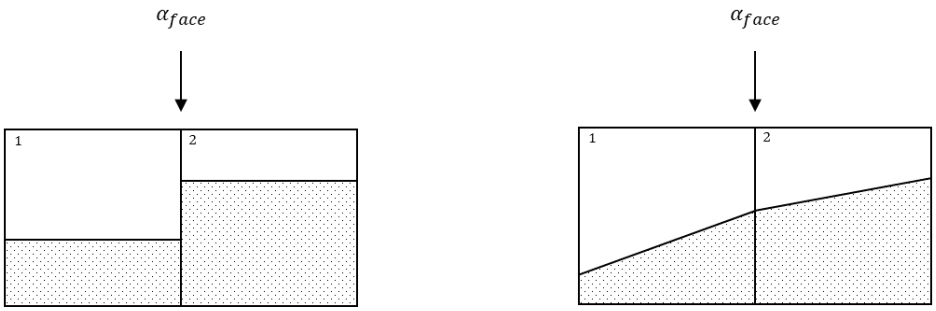

Figure 2.3: Left: Interface representation in DA-based schemes. Face volume fraction has to be interpolated. Right: Interface representation in PLIC schemes. Face volume fraction is known.

List 2.1: Calculation steps during one time step in algebraic approach

1. Volume fraction gradient is used to infer if the interface in the cell is either vertical or horizontal
2. The face volume fractions are interpolated
3. The advection equation is integrated and solved, yielding the new volume fractions

List 2.2: Calculation steps during one time step in geometrical approach

1. Face volume fractions are known from reconstructed interface
2. Geometric interface is discarded
3. The advection equation is integrated and solved, yielding the new volume fractions
4. Reconstruction of interface using the new volume fractions

2.4.1. Normalized Variable Diagram

In order to find the face values of the volume fraction needed to solve the transport equation for the volume fraction, many discretization schemes can be employed. In the original article by Hirt & Nichols, α_f is approximated using a second order central difference scheme. However, since the central difference scheme does not care about the flow direction, this representation may pose some problems (does not satisfy transportiveness). *Trasportiveness* indicates the ability of the scheme to 'sense' in what direction the solution is traveling. This can be illustrated by the simple example of a small particle traveling (advecting) with a constant velocity from left to right in an equidistant grid, as shown in Figure 2.4. When the particle has reached point 'P', the flux through 'e' can be interpolated

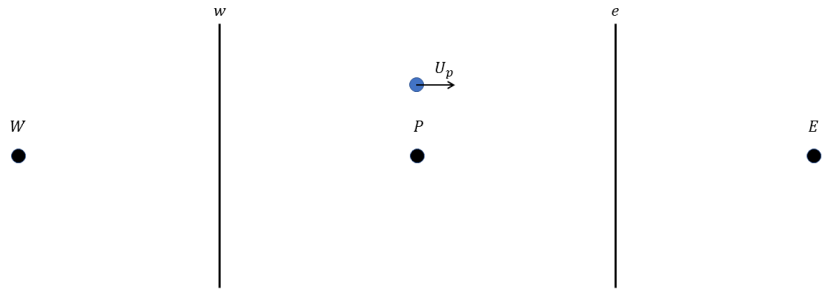

Figure 2.4: Schematic representation of equidistant computational grid

using a central difference scheme (2.22) or a first order upwind scheme (2.23), hence

$$\phi_e = \frac{\phi_P + \phi_E}{2} \tag{2.22}$$

$$\phi_e = \phi_P \tag{2.23}$$

Thus, the velocity yielded by the central difference scheme will be the average of the velocity in point 'E' and point 'P'. This seems a reasonable approximation. However, due to the spatial dependency of the particle's velocity, the velocity in point 'E' is zero. Subsequently, the velocity will be interpolated

as the average of its original value and zero. Therefore, an error is introduced that is defined by the difference between the value from the previous iteration, in this case the eastern value, and the boundary conditions. Depending on the Peclet (Pe) number the error will reduce or grow indefinitely. The Peclet number tells us the ratio of advective transport to diffusive transport and this case will be infinity (no diffusive transport), hence:

$$Pe = \frac{\rho U \Delta x}{\nu} \tag{2.24}$$

In short, a Peclet number above two indicates that using a central difference scheme will pose stability issues.

With the upwind scheme this problem is solved by simply setting the flux equal to the 'upwind' (the opposite direction of the velocity) value. However, by doing so an artificial diffusion is added tot the solution. This phenomenon is also called *numerical diffusion*. When the flow direction is aligned with the grid the transport of entities is overpredicted in the flow direction. When the flow is not aligned with the grid, the error also spreads diffusively through the domain. This process is depicted in Figure 2.5. For this reason, many authors switched to higher order upwind schemes or a combination of

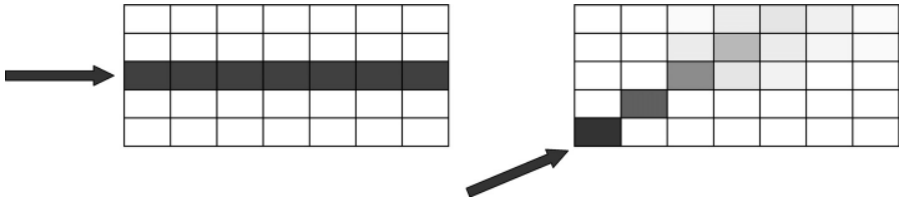

Figure 2.5: Schematic illustration of numerical diffusion (right), from [4]

upwind and downwind schemes, the so-called QUICK scheme, for the discretization of α_f. Although, higher order schemes do address the artificial smearing (caused by numerical diffusion) of the interface, they do not preserve a monotonic distribution of the volume fraction. Therefore, they are said to be non-monotonic. *Monotonicity* is explicitly defined as:

"The numerical solution should have a monotone behavior, whereby the new solution ϕ_i^{n+1} at time index $(n+1)$ should not reach values outside the range (ϕ_{i+j}^n) at time step n."[36]

In general, experience showed that the first order upwind scheme is extremely artificially diffusive depending on the flow to grid angle. Second order upwinding solves this issue, but exhibits high overshoots at some flow to grid angles. Although QUICK gives a steeper resolution of discontinuous profiles, it still introduces angle dependent overshoots and oscillations [37].

Now, lets return to the example of the DA-scheme and add an upwind cell as depicted in Figure 2.6. For the purpose of checking monotonicity, a Convective Boundedness Criterion (CBC) is formulated as:

$$\phi_D \leq \phi_f \leq \phi_A \tag{2.25}$$

Where ϕ represents any convected variable and *boundedness* previously is referred to as monotonicity. In addition normalized variables are introduced:

$$\tilde{\phi}_f = \frac{\phi_f - \phi_U}{\phi_A - \phi_U} \tag{2.26}$$

$$\tilde{\phi}_D = \frac{\phi_D - \phi_U}{\phi_A - \phi_U} \tag{2.27}$$

Using the normalized variables, a schematic representation of schemes that satisfy CBC is constructed in Figure 2.7.

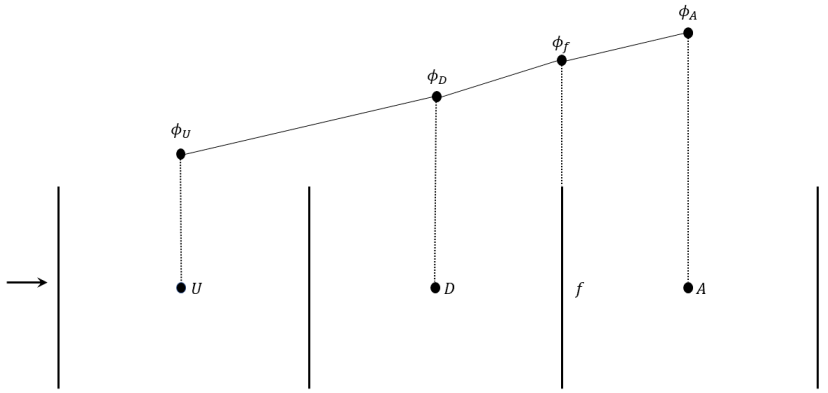

Figure 2.6: Schematic representation of Donor Acceptor scheme with extra upwind cell. Upwind cell (left), Donor cell (middle-left), face (middle-right) and Acceptor cell (right).

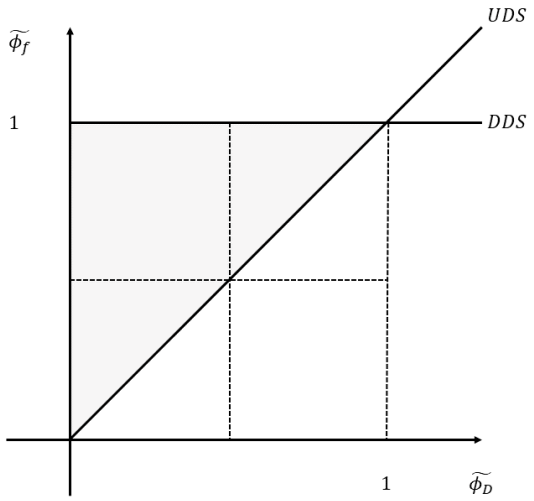

Figure 2.7: Normalized Variable Diagram, grey area indicates CBC satisfaction.

The diagram of Figure 2.7 is also referred to as the Normalized Variable Diagram (NVD) and aims to continuously connect the upwind and downwind schemes. By doing so, the diffusive behavior of the first order upwind schemes can be minimized. The NVD-diagram is used to check whether the combination of downwind and upwind schemes satisfy the CBC-criterion. Switching to higher order upwind schemes decreases the degree of numerical diffusion, while the downwind schemes are used to counteract the numerical diffusion, also called *anti-diffusion*. Moreover, the first order upwind scheme forces the solution to remain monotonic. In practice, the aim is to produce sharp, but also monotonic solutions. The grey area represents the region where CBC is satisfied.

One of the most widely employed NVD-schemes is the High Resolution Interface Capturing scheme. This scheme is also available in Fluent. For extra elaboration on this scheme, the reader is referred to Appendix A.2.

2.4.2. Setting up the VOF model in Ansys Fluent

Throughout this work the explicit time integration VOF formulation is used. Fluent provides a sharp interface modeling, a dispersed interface modeling and a combination of both. Since the annular flow regime is assumed, a sharp interface between the vapor and liquid phase is expected. Therefore, the sharp interface model is chosen. When using the sharp modeling type, the option of interfacial anti-diffusion can be enabled. This option tempers the numerical diffusion originating from the volume fraction advection schemes and therefore enhances accuracy. However, using this treatment also leads to convergence problems. It is recommended by Fluent to use the *implicit* body force formulation. This formulation will enhance convergence speed. In multiphase flows, often the body forces due to surface tension and gravity as well as the pressure gradient are large compared to the forces due to convection and viscosity. Therefore, most of the time the body forces are almost in equilibrium with the pressure gradient. Taking this partial equilibrium into account enhances convergence speed. For the discretization of volume fraction transport, either the modified HRIC scheme or the Geo-Reconstruct scheme are used in this work. Extra information on both schemes can be found in Appendix A.2 and Appendix A.1, respectively. In addition, some elaboration on the modeling options in Fluent is given in Appendix A.3.

2.5. Surface tension effects

Surface tension stems from the fact that liquid molecules attract each other, also referred to as *cohesion*. However, only at an interface cohesion results in tension. In the bulk of the liquid, all molecules attract each other with the same force and therefore the net result is zero. However, at the interface the the difference between the adhesive forces (attraction force between molecules of different sort) and cohesive forces results in so-called *surface tension*.

Dimensionless numbers are helpful in estimating if the surface tension will be important. First, the Reynolds number (the ratio between the inertial and viscous forces) will define if one needs to check either the Weber number or the Capillary number. The Weber number represents the influence of inertial forces to those of the surface tension forces. The capillary number is the ratio between the viscous forces and the surface tension forces. From this one can conclude that if $Re << 1$ the capillary number will be important, while the Weber number will be of significance if $Re >> 1$.

$$We = \frac{\rho L U^2}{\sigma} \tag{2.28}$$

$$Ca = \frac{\mu U}{\sigma} \tag{2.29}$$

Many authors have investigated the effect of surface tension on the liquid film behavior. In the study performed by Liu et al[38], the surface tension effects on a liquid film in the wavy laminar regime was investigated. This study showed that the magnitude of the surface tension has a significant effect on the surface wave formation. Since surface waves play an important role in the heat transfer performance, the surface tension coefficient σ has to be chosen carefully.

2.5.1. Continuum Surface Force model

One of the most widely used surface tension models, is the Continuum Surface Force model developed by Brackbill [39]. In Fluent, this model is available in combination with the VOF model. The extra force as the result of surface tension is included in the momentum equations using a source term. Key features of this model consist of no need of interface reconstruction and accurate modeling of two- and three- dimensional flow driven by surface forces. Moreover, no restrictions are set to the number, complexity, or dynamic evolution of fluid interfaces.

From theory we know that the surface tension force normal to the interface depends on the radii of the curvature of the interface according to Equation 2.30

$$p_2 - p_1 = \sigma\kappa \tag{2.30}$$

$$\kappa = \frac{1}{r_1} + \frac{1}{r_2} \tag{2.31}$$

As shown in Equation 2.30, the force is actually a pressure drop across the interface, $p_2 - p_1$. By making use of the volume fractions to determine the surface interface curvature, there is no need for interface

reconstruction. First, the interface normal n is determined by taking the gradient of the volume fraction α_i. Where i represents the phase-indice. Thereafter, the curvature of the interface κ is deduced as the divergence of the normal interface unit vector.

$$\vec{n} = \nabla \alpha_q \tag{2.32}$$

$$\hat{\vec{n}} = \frac{\vec{n}}{|\vec{n}|} \tag{2.33}$$

$$\kappa = \nabla \cdot \hat{\vec{n}} \tag{2.34}$$

Now the force is defined as volume force using the divergence theorem.

$$F_{vol} = \Sigma_{i<j} \sigma_{ij} \frac{\alpha_i \rho_i \kappa_j \nabla \alpha_i + \alpha_j \rho_j \kappa_i \nabla \alpha_i}{\frac{1}{2}(\rho_i + \rho_j)} \tag{2.35}$$

When there are only two phases, $\kappa_i = -\kappa_j$ and $\nabla \alpha_i = -\nabla \alpha_j$. Therefore Equation 2.35 can be written as:

$$F_{vol} = \sigma_{ij} \frac{\rho \kappa_i \nabla \alpha_i}{\frac{1}{2}(\rho_i + \rho_j)} \tag{2.36}$$

Another surface tension model available in Fluent is the Continuum Surface Stress (CSS) model by Lafaurie et al [40]. The considerable advantage of this model over the CSF method is the conservative nature of the surface tension force definition when surface tension σ is variable. However, since surface tension is taken as a constant throughout this work, only the CSF model is discussed. One of the major setbacks of surface tension models is the development of *spurious currents*. These currents are the result of an imbalance of the surface tension force and the pressure drop across the interface. The currents are characterized by non-physical vortexes close to the interface, and cause the interface to take unrealistic deformations [41].

2.5.2. Wetting behavior,contact angle and wall adhesion

As stated in [42] the wetting behavior of liquids can be classified as *non-wetting* ($90° < \theta < 180°$), *partially wetting* ($0° < \theta < 90°$) or *completely wetting* ($\theta = 0°$). The wettability of a liquid can have a considerate influence on the heat transfer. This is shown in an article by H. El Mghari et al. [43], where the influence of the contact angle (wettability) of the liquid film is assessed for flow condensation in square micro-channels. The trend is found that increasing the contact angle form $6°$ to $15°$ enhances the heat transfer up to 100%. In [10] this is also shown for film condensation on a vertical short plate. In this paper the contact angle θ is varied from $0°$ to $10°$ yielding heat transfer coefficient increasing from $\approx 2500 W/m^2K$ to $\approx 2575 W/m^2K$. The wetting behavior also depends on the interaction of the material of the contact surface with water. The material can either be *hydrophilic* or *hydrophobic*. When a material is hydrophilic, it has an affinity for water and allows the water to form a film while hydrophobic materials have a natural tendency to repel water. This results in the formation of multiple droplets on the surface.

Throughout this work the liquid films flowing over the walls will be thicker than a few computational cells thick. Meaning that wall adhesion effects can be neglected. However, when not, wall adhesion is taken into account by enabling the wall adhesion model in conjunction with setting the contact angle (θ_w). The contact angle determines the near wall shape of the interface by imposing a dynamic boundary condition. The dynamic boundary condition is constructed by adjusting the interface curvature of Equation 2.34 trough the wall surface normal according to:

$$\hat{\vec{n}} = \hat{\vec{n}}_w cos(\theta_w) + \hat{\vec{t}}_w sin(\theta_w) \tag{2.37}$$

Where $\vec{n}_w$ and $\vec{t}_w$ are the unit vectors normal and tangential to the wall, respectively.

As shown by Ishikawa [13],where a wavy liquid film is flowing over a corrugated wall, wall contact angle does not influence the flow field when fully wetted. However, at the inflow or outflow boundary the contact angle might have an effect.

3

Phase Change Modeling

3.1. Introduction

In this section results from a literature study to phase change modeling focused on condensation in plate heat exchangers is presented. The main purpose of this section is to present the status quo in phase change modeling and the theory behind it. First, phase change models widely employed in literature will be discussed. Secondly, modeled geometries and accompanying flow features reviewed. Finally, a short summary and remaining questions will be presented.

3.2. Heat Flux Balance approaches

3.2.1. Theory

The energy jump condition stems from the Hugeniot jump condition for shocks. The first jump condition states that the mass flux J must be constant across the shock front:

$$\rho_1 C_{n1} = \rho_2 C_{n2} = J \tag{3.1}$$

Where C_n represents the velocity component normal to the shock. Now, one can imagine the vapor-liquid interface as a shock front. The only difference with a shock front is that the density now changes due to phase change instead of a shock. Now, when the interface is considered to be non-quiescent, the jump condition reads as follows:

$$\rho_l(C_{n,l} - D) = \rho_v(C_{n,v} - D) = J \tag{3.2}$$

Where l and v represent the liquid and vapor phase respectively and D represents the normal component of the interface velocity. Now consider the interface in Figure 3.1. In this figure, a simple heatflux balance across the interface is depicted according to:

$$\vec{q}_l'' \cdot \hat{\vec{n}} = \vec{q}_v'' \cdot \hat{\vec{n}} \tag{3.3}$$

$$\rho_l h_l(C_{n,l} - D) - k_l \nabla T_l \cdot \hat{\vec{n}} = \rho_v h_v(C_{n,v} - D) - k_v \nabla T_v \cdot \hat{\vec{n}} \tag{3.4}$$

Reorganization of 3.4 and substitution of 3.2 yields the following energy jump condition for the mass flux:

$$J = \frac{k_v \nabla T_v \cdot \hat{\vec{n}} - k_l \nabla T_l \cdot \hat{\vec{n}}}{h_{fg}} \tag{3.5}$$

where $h_{fg} = h_v - h_l$ represents the latent heat of phase change. In order to obtain the mass transfer per unit volume $(\dot{m})$, the mass transfer rate per unit area (J) has to be multiplied by absolute volume fraction:

$$\dot{m}_{lv} = J|\nabla\alpha| \tag{3.6}$$

$$\hat{\vec{n}} = \frac{\nabla\alpha}{|\nabla\alpha|} \tag{3.7}$$

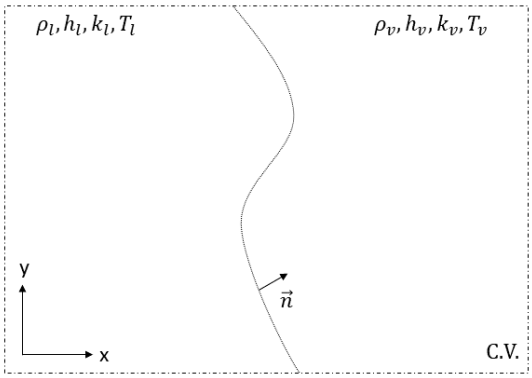

Figure 3.1: Control volume considered in an heat flux balance approach.

$$\dot{m}_{lv} = \frac{k_v \nabla T_v \nabla \alpha_v - k_l \nabla T_l \nabla \alpha_l}{h_{fg}} \tag{3.8}$$

where $\dot{m}_{lv}$ represents the volumetric mass transfer in $kg/m^3 s$. The heat flux balance across the interface is often written as:

$$\overrightarrow{q''}_i = \left(k_l \frac{\partial T}{\partial n}\bigg|_l - k_v \frac{\partial T}{\partial n}\bigg|_v \right) \vec{n} \tag{3.9}$$

Nichita and Thome [44] simplified the model relating the temperature gradient to the liquid volume fraction gradient. Resulting in the following definition for the mass source term:

$$\dot{m}_{lv} = \frac{(\alpha_l k_l + \alpha_v k_v)(\nabla T \cdot \nabla \alpha_l)}{h_{fg}} \tag{3.10}$$

According to Sun, the mass transfer at the interface should only depend on the conductivity of the unsaturated phase. For the reason that the entire energy flow only interacts with the unsaturated phase, lying between the saturated phase and the wall. In line with this theory, Sun [45] further simplified the model by assuming one of the phases is completely in saturation state. For this reason, no change in temperature is expected and hence the heat conduction in the saturated phase is zero. In addition two extra assumptions were made:

- The thermal conductivity k_{uns} and specific heat $C_{p,uns}$ of the unsaturated phase are considered physical parameters.
- Since the temperature throughout the saturated phase is constant, the specific heat of the saturated phase is assumed equal to the specific heat of the unsaturated phase: $C_{p,s} = C_{p,uns}$

Now, equation 3.9 is written as:

$$\overrightarrow{q''}_i = k_{uns} \frac{\partial T}{\partial n}\bigg|_{uns} \vec{n} \tag{3.11}$$

With $\vec{n}$ pointing towards the saturated phase. This results in the redefinition of Equation 3.10:

$$\dot{m}_{lv} = \frac{(2k_l)(\nabla T \cdot \nabla \alpha_l)}{h_{fg}} \tag{3.12}$$

Although a mass source term based on Fourier's law does not take into account kinetic effects, the physical base of the model makes it a popular method throughout the literature.

3.3. Kinetic Gas Theory based models

3.3.1. Schrage model

The kinetic theory of gases states that the macroscopic properties of a gas are a result of the microscopic random collisions of the gas its molecules. Before the kinetic theory of gasses can be applied to evaporation or condensation, several assumptions have to be done. First the particles considered are assumed to interact as rigid not attracting spheres with a finite diameter. Also it is assumed that all particles move randomly in each direction. The water vapor molecules are assumed to act like an ideal gas. In addition, the vapor is assumed to be in equilibrium except for a small region near the liquid phase. This region has the dimension of few molecular mean free path thick and is also referred to as the Knudsen layer, and is the physical domain considered.

Boltzmann used statistical analysis to describe that the probability that any one molecule has an energy E decreases exponentially with energy. Since the number of possible energy states decrease when a molecule has an energy state higher than average and the probability an energy state exists is proportional to the number of possible energy states, energy states lower than average are favored. The mathematical form of the Boltzmann distribution is:

$$f(E) = Ae^{-E/k_bT} \tag{3.13}$$

$f(E)$ represents the probability function that a particle (molecule) has an energy E, A is a normalization constant, k_b is the famous Boltzmann constant and T is the temperature.

The velocity distribution function for molecules stems from the situation where molecules move randomly in a container. In this container exchange of momentum and energy happens through collisions. Also it is assumed that the system is in thermodynamic equilibrium. Therefore all macroscopic quantities will be constant with respect to the surroundings of the container. When a system of molecules is considered as an ideal gas and the only energy is considered kinetic energy, the velocity distribution function, $f(c_j, x_j, t)$, can be obtained from the Boltzmann equation:

$$\frac{\partial f}{\partial t} + c_j \frac{\partial f}{\partial x_j} = S(f) \tag{3.14}$$

Where c_j and x_j represent the speed and position of the jth molecule. $S(f)$ represents the collision term. If one assumes that the interface does not influence the molecular velocity, the distribution function for the velocity near the interface can be considered Maxwellian and the Maxwell-Boltzmann distribution is obtained[46]:

$$f(c) = n\Big[\frac{m}{2\pi k_b T}\Big]^{3/2} e^{-\frac{m}{2k_bT}(c_j-\overline{c})^2} \tag{3.15}$$

We can write Equation 3.14:

$$\beta = \sqrt{\frac{M}{2RT}} \tag{3.16}$$

$$(c_j - \overline{c})^2 = C^2 = \left[(u-\overline{u})^2 + (v-\overline{v})^2 + (w-\overline{w})^2\right] \tag{3.17}$$

$$f(c) = n\Big[\frac{\beta^3}{\pi^{3/2}}\Big]e^{-\beta^2 C^2} \tag{3.18}$$

Where n represents the number density of the molecules, R the gas constant, m the mass of a molecule and M the mass of the molecules per mole.

Considering the Knudsen layer in Figure 3.2, the net mass flux J across the interface can be determined according to:

$$J = J_{lv} - J_{vl} \tag{3.19}$$

And the rate of vaporization:

$$J = \int_{\infty}^{-\infty}\int_{\infty}^{-\infty}\int_{0}^{-\infty} muf_l dudvdw \tag{3.20}$$

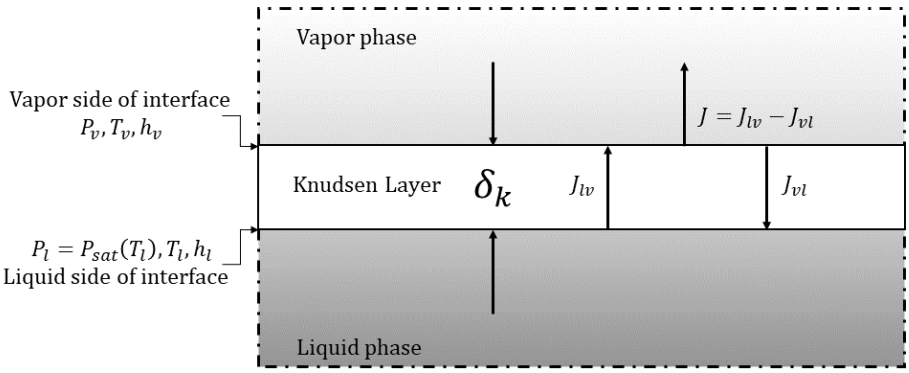

Figure 3.2: Physical domain considered with boundary conditions in derivation of the Hertz-Knudsen equation. Modified from [5]

Now, since the particles move randomly in all directions:

$$\overline{u} = \overline{v} = \overline{w} = 0 \tag{3.21}$$

And using the error function:

$$erf(\eta) = \frac{2}{\sqrt{\pi}} \int_0^{\eta} e^{-y^2} dy = \frac{1}{\sqrt{\pi}} \int_{-\eta}^{\eta} e^{-y^2} dy \tag{3.22}$$

$$erf(\infty) = 1 \tag{3.23}$$

equation 3.20 can be written as:

$$J_{lv} = \int_{\infty}^{-\infty} \int_{\infty}^{-\infty} \int_{0}^{-\infty} mn \frac{\beta^3}{\pi^{3/2}} u e^{-\beta^2(u^2+v^2+w^2)} du dv dw \tag{3.24}$$

$$J_{lv} = \int_{\infty}^{-\infty} e^{-\beta^2 w^2} dw \int_{\infty}^{-\infty} e^{-\beta^2 v^2} dv \int_{0}^{-\infty} mn \frac{\beta^3}{\pi^{3/2}} u e^{-\beta^2 u^2} du \tag{3.25}$$

Using the error function and $mn = \rho_l$:

$$J_{lv} = \frac{\rho_l \beta}{\sqrt{\pi}} \int_0^{\infty} u e^{-\beta^2 u^2} du \tag{3.26}$$

$$J_{lv} = \frac{\rho_l}{2\sqrt{\pi}\beta} \tag{3.27}$$

Using the ideal gas law, Equation 3.27 can be written as:

$$J_{lv} = \sqrt{\frac{M}{2\pi R}} \frac{p_{sat}(T_l)}{\sqrt{T_l}} \tag{3.28}$$

For net evaporation to take place, there has to be a small departure from equilibrium. Since a departure from equilibrium resulting in evaporation will only take place as a result of a change in liquid properties, the Maxwellian distribution of the vapor phase is assumed to be dependent on the pressure and temperature of the liquid near the interface. Hence, the leaving molecules are not affected by the vapor phase or interchange of mass, energy and momentum by the phases.

For the condensation rate the same procedure results in:

$$J_{vl} = \sqrt{\frac{M}{2\pi R}} \frac{p_v}{\sqrt{T_v}} \tag{3.29}$$

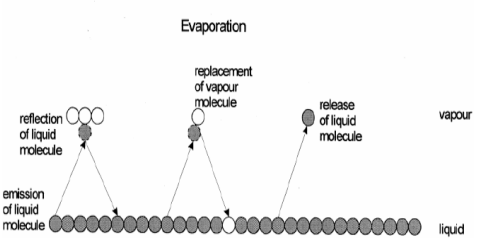

Figure 3.3: Evaporation [5]

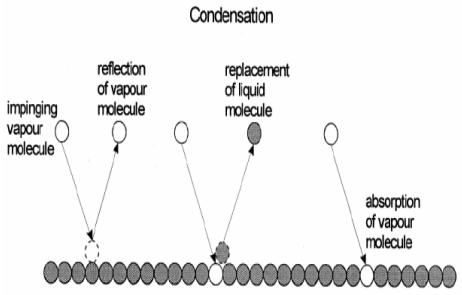

Figure 3.4: Condensation [5]

At higher pressures than the vapor pressure, there is a departure from thermodynamic equilibrium and water condenses. Since in a thermodynamic equilibrium the vapor pressure equals the saturation pressure the vapor pressure is assumed to be the saturation pressure.

Now the net mass flux becomes:

$$J = J_{lv} - J_{vl} = \sqrt{\frac{M}{2\pi R}}\left[\frac{p_{sat}(T_l)}{\sqrt{T_l}} - \frac{p_v}{\sqrt{T_v}}\right] \tag{3.30}$$

Results from calculations using the above equation turned out higher than results obtained from experiments . This implies that not all emitted particles (molecules) from the first phase are absorbed by the other phase. This is shown in Figure 3.3 and Figure 3.4 for evaporation and condensation, respectively. In order to match experiments, two coefficient need to be added to the equation for the net mass flux. The coefficients represent the number of molecules absorbed by phase B divided by the number of molecules released by phase A and are commonly known as the evaporation and the condensation coefficient:

$$\gamma_{ev} = \frac{number\ of\ molecules\ transferred\ to\ the\ vapor\ phase}{number\ of\ molecules\ emitted\ from\ the\ liquid\ phase} \tag{3.31}$$

$$\gamma_{con} = \frac{number\ of\ molecules\ transferred\ to\ the\ liquid\ phase}{number\ of\ molecules\ emitted\ from\ the\ vapor\ phase} \tag{3.32}$$

In thermodynamic equilibrium the condensation coefficient and the evaporation coefficient are equal. However, when there is a departure from equilibrium the coefficients do not necessarily have to be equal [46][47]. However, this is exactly what was assumed by Schrage [48]: $\gamma_{ev} = \gamma_{con} = \gamma$. Now Equation 3.30 is rewritten as:

$$J = \gamma\sqrt{\frac{M}{2\pi R}}\left[\frac{p_{sat}(T_l)}{\sqrt{T_l}} - \frac{p_v}{\sqrt{T_v}}\right] \tag{3.33}$$

In addition, in order to be able to account for kinetic effects of the vapor phase, a bulk velocity was assigned to the vapor particles according to:

$$\overline{u} \neq \overline{v} = \overline{w} = 0 \tag{3.34}$$

Resulting in:

$$J = J_{lv} - J_{vl} = \frac{2}{2-\gamma_{con}}\sqrt{\frac{M}{2\pi R}}\left[\gamma_{ev}\frac{p_{sat}(T_l)}{\sqrt{T_l}} - \gamma_{con}\frac{p_v}{\sqrt{T_v}}\right] \tag{3.35}$$

$$= \frac{2\gamma}{2-\gamma}\sqrt{\frac{M}{2\pi R}}\left[\frac{p_{sat}(T_l)}{\sqrt{T_l}} - \frac{p_v}{\sqrt{T_v}}\right] \tag{3.36}$$

Which is also referred to as the Hertz-Knudsen-Schrage relation. The previous derivation is taken and modified from P. Sharma [5]. A similar derivation is found in Tanasawa [49]. The volumetric mass source term is given by:

$$S_v = -S_l = J|\nabla \alpha_v| \tag{3.37}$$

On the evaporation/condensation coefficient

The evaporation and condensation coefficient of substances as water and mercury have been thoroughly investigated in the past. Many authors conclude that the coefficients not necessarily have to be equal. Barret and Clement [50] state a possible explanation: the evaporation coefficient depends only on the wall temperature and the pressure of the liquid surface. The condensation coefficient, however, depends on the wall temperature but also on the temperature of the vapor just of the absorbing surface. The reason for this difference in dependency is not further clarified.

One of the difficulties posed by measuring the coefficients is the measurement of the interface temperature. Since the temperature jumps across an interface of thickness of a few molecules, this measurement is not possible, while extrapolating the temperature from bulk temperatures of vapor and liquid is extremely prone to errors [14]. Marek and Straub [14] conducted a thorough review about the evaporation and condensation coefficient of water. For different experimental setups and measuring methods the evaporation coefficient can range from 0.001 to 1, while the condensation coefficient lies in the range of approximately 0.01 to 1. Because of the extreme variation of both coefficients, it was concluded that: "A unique determination of evaporation and condensation coefficients as typical property of water dependent on temperature and pressure is not possible". However, two main categories could be identified.

$$0.1 \leq \gamma < 1.0 \ (Group\ I) \tag{3.38}$$

$$\gamma < 0.1 \ (Group\ II) \tag{3.39}$$

Most of the evaporation coefficient data falls in group II while the data of the condensation coefficient tends to fall into group I. This finding clearly indicates that the condensation coefficient is generally larger than the evaporation coefficient. In addition Marek & Straub conclude that both coefficients decrease with increasing temperature and increasing pressure. Finally Marek & Straub state that, due to dynamic surface tension and a reduced sensitivity to impurities, γ (for both condensation and evporation) lies in group I for jets and moving films, while γ will be in group II for quasi-static stagnant films.

Marek & Straub summarized the reviewed literature very clear in a table. The published experiments relevant for film condensation are depicted below in Table 3.1. In general, there is no clear consensus

Table 3.1: Studies on the condensation coefficient during condensation on dynamically renewing surfaces, from [14]

Year	Author(s)	γ	$T°C$	Method
1961	Berman [51]	1	10	Film condensation on horizontal tube, no details about temperature measurement
1963	Nabavian & Bromely [52]	0.35-1	7-50	Film condensation on horizontal grooved tube, measurement of vapour temperature with a thermometer
1967	Mills & Seban [53]	0.45-1	7.6-10.2	Film condensation on vertical copper plate, measurement of temperature distribution in the plate
1968	Tanner et al [54]	>0.1	22-46	Dropwise condensation on vertical copper plate, measurement of block temperature with thermocouples
1969	Wenzel [55]	1.0	22-46	Film condensation experiments of Tanner et al. [54] measurement of block temperature with thermocouples
1986	Hatamiya & Tanaka [56]	0.2-0.6	6.9-26.9	Dropwise condensation on vertical copper cylinder, no details about temperature measurement

about the condensation coefficient but that this coefficient is bigger than 0.1. The condensation coefficient proves to be very case dependent. Subsequently the application of the Schrage model will be a tedious process. The coefficient needs to be tuned with experimental data exactly representing the modeled configuration. Hence, when the correct value for γ_{vl} is finally found, the coefficient will not necessarily be usable in up-scaled configurations.

3.3.2. Tanasawa model

In 1991, Tanasawa [49] developed a modification of the model by Schrage for condensation. Tanasawa stressed that the difference between the liquid-vapor interface temperature (T_i, corresponding to T_l in Schrage's formulation) and the vapor temperature is very small except at low pressures. But, for condensation to take place, there has to be a finite difference. This leads to the following assumption:

$$\frac{T_v - T_i}{T_v} << 1 \tag{3.40}$$

The mass transfer of Equation 3.36 is defined in the way that net evaporation has a positive magnitude. Now, when condensation is the desired positive outcome, the equation can be rearranged according to:

$$J = J_{ev} = -J_{con} \tag{3.41}$$

$$J_{con} = \frac{2\gamma}{2-\gamma}\sqrt{\frac{M}{2\pi R}}\left[\frac{p_v}{\sqrt{T_v}} - \frac{p_{sat}(T_l)}{\sqrt{T_l}}\right] \tag{3.42}$$

Using the assumption of 3.40, Equation 3.42 is written as:

$$J_{con} = \frac{2\gamma}{2-\gamma}\sqrt{\frac{M}{2\pi R}}\frac{p_v}{\sqrt{T_v}}\left[\frac{p_v - p_{sat}(T_l)}{p_v} - \frac{T_v - T_l}{2T_v}\right] \tag{3.43}$$

According to Tanasawa [49], the pressure term between the brackets is normally way higher than the temperature term, even for very low pressures. This is a feasible assumption since the pressure jump across the interface can be considerably higher due to the curvature of the interface. For this reason the temperature term is neglected and we arrive at:

$$J_{con} = \frac{2\gamma}{2-\gamma}\sqrt{\frac{M}{2\pi R}}\left[\frac{p_v - p_{sat}(T_l)}{\sqrt{T_v}}\right] \tag{3.44}$$

Now the Clausius-Clapyeron relation can be employed to rewrite Equation 3.44

$$\frac{p_v - p_{sat}(T_l)}{T_v - T_l} \approx \frac{\rho_v h_{fg}}{T_v} \tag{3.45}$$

$$J_{con} = \frac{2\gamma}{2-\gamma}h_{fg}\sqrt{\frac{M}{2\pi R}}\left[\frac{\rho_v(T_v - T_l)}{T_v^{3/2}}\right] \tag{3.46}$$

In this way the condensation mass transfer is linearly dependent on the temperature difference between the interface and the vapor phase. Again, the volumetric mass source term is given by:

$$S_v = -S_l = J|\nabla\alpha_v| \tag{3.47}$$

3.3.3. Lee model

The Lee model originates from the model for interface mass transfer based on the kinetic theory of gases proposed by Schrage [48]. The model is based on the assumption that both phases are in saturation states. However, the model allows for jump in pressure and temperature across the interface. This resulted in the modified version of the Hertz-Knudsen relation, the so-called Hertz-Knudsen-Schrage relation for evaporation and condensation:

$$J = J_{ev} = -J_{con} \tag{3.48}$$

$$J_{con} = \frac{2\gamma}{2-\gamma}\sqrt{\frac{M}{2\pi R}}\left[\frac{p_v}{\sqrt{T_v}} - \frac{p_{sat}(T_l)}{\sqrt{T_l}}\right] \tag{3.49}$$

Since condensation is of our most interest, we continue with the derivation of the condensation mass flux equation 3.49. The first term in 3.49 can be expressed in terms of an accommodation coefficient a_c.

$$a_c = \frac{2\gamma}{2-\gamma} \tag{3.50}$$

This coefficient represents the experimentally obtained condensation velocity to the theoretical maximum condensation velocity [57].

The Clausius-Clapeyron equation relates the pressure to the temperature at saturated conditions:

$$\frac{dP}{dT} = \frac{h_{fg}}{T\left(\frac{1}{\rho_v} - \frac{1}{\rho_l}\right)} \tag{3.51}$$

Integration gives:

$$p - p_{sat} = \frac{h_{fg}}{T\left(\frac{1}{\rho_v} - \frac{1}{\rho_l}\right)}(T - T_{sat}) \tag{3.52}$$

Substitution into the HKS-relation gives:

$$J_{con} = a_c \sqrt{\frac{M}{2\pi R T_{sat}}} \frac{\rho_v \rho_l h_{fg}}{\rho_l - \rho_v} \frac{T_{sat} - T}{T_{sat}} \tag{3.53}$$

Which is normally rewritten to:

$$J_{con} = a_c \sqrt{\frac{M}{2\pi R T_{sat}}} \frac{h_{fg}}{\frac{1}{\rho_v} - \frac{1}{\rho_l}} \frac{T_{sat} - T}{T_{sat}} \tag{3.54}$$

Since the mass source term in the VOF continuity equation should be in the units of $kg/m^3 s$, equation 3.57 has to be multiplied by the volumetric interfacial surface area a_i. In literature, two approaches for the determination of this parameter are discussed. However, both approaches are discarded due to implementation problems [57][38]. To counter this problem, another approach is proposed. In the approach by de Schepper et al [57], first the evaporation/condensation coefficient is assumed to be unity, which results in:

$$a_c = \frac{2\gamma}{2 - \gamma} = 2 \tag{3.55}$$

Next, assuming spherical bubbles, the volumetric interfacial surface area is related to the Sauter mean diameter according to:

$$a_i = \frac{6\alpha_v}{D_{sm}} \tag{3.56}$$

Now, multiplication with a_i and substitution of a_c leads to:

$$\dot{m}_{con} = a_i a_c \sqrt{\frac{M}{2\pi R T_{sat}}} \frac{h_{fg}}{\frac{1}{\rho_v} - \frac{1}{\rho_l}} \frac{T_{sat} - T_v}{T_{sat}} \tag{3.57}$$

$$\dot{m}_{con} = \frac{12\alpha_v}{D_{sm}} \sqrt{\frac{M}{2\pi R T_{sat}}} \frac{h_{fg}}{\frac{1}{\rho_v} - \frac{1}{\rho_l}} \frac{T_{sat} - T_v}{T_{sat}} \tag{3.58}$$

However, de Schepper et al [57] provides us with the following definition:

$$\dot{m}_{con} = \frac{6\alpha_v}{D_{sm}} \sqrt{\frac{M}{2\pi R T_{sat}}} \frac{h_{fg}}{\frac{1}{\rho_v} - \frac{1}{\rho_l}} \frac{T_{sat} - T_v}{T_{sat}} \tag{3.59}$$

Identification reveals that multiplication by the accommodation ($a_c = 2$) coefficient is missing. Liu et al[38] arrive at the same equation as de Schepper et al. However, they assume that the accommodation coefficient has a value of unity, which does result in Equation 3.59.

In any case, Equation 3.59 is rewritten in its final form according to:

$$\dot{m}_{con} = r_v \alpha_v \rho_v \frac{T_{sat} - T}{T_{sat}} \tag{3.60}$$

Analogously to the vapor to liquid mass transfer source term, the liquid to vapor source term can be deduced. Now the complete Lee model is written as:

$$\dot{m}_{ev} = -r_l \alpha_l \rho_l \frac{T_{sat} - T}{T_{sat}} \qquad T \geq T_{sat} \tag{3.61}$$

$$\dot{m}_{con} = r_v \alpha_v \rho_v \frac{T_{sat} - T}{T_{sat}} \qquad T < T_{sat} \tag{3.62}$$

which is the original model proposed by Lee [58]. Here r_l/r_v are referred to as the evaporation/condensation frequency or the mass transfer time relaxation parameter and have the units of s^{-1}. This finally results in the following definitions of r_l and r_v:

$$r_l = \frac{6}{D_{sm}} \sqrt{\frac{M}{2\pi R T_{sat}}} \frac{h_{fg} \rho_v}{\rho_l - \rho_v} \tag{3.63}$$

$$r_v = \frac{6}{D_{sm}} \sqrt{\frac{M}{2\pi R T_{sat}}} \frac{h_{fg} \rho_l}{\rho_l - \rho_v} \tag{3.64}$$

In the literature the above mentioned source terms are indicated with different letters, subscripts etc. For convenience this is pointed out below:

$$\dot{m}_{con} = \dot{m}_{gl} = \dot{m}_{vl} = S_{vl} = S_{gl} = S_l \tag{3.65}$$

$$\dot{m}_{ev} = \dot{m}_{lg} = \dot{m}_{lv} = S_{lv} = S_{lg} = S_v \tag{3.66}$$

Where S_l and S_v represent the source terms included in the VOF continuity equations of the liquid and vapor phase respectively according to:

$$\frac{\partial}{\partial t}(\alpha_v \rho_v) + \nabla \cdot (\alpha_v \rho_v \vec{u}_v) = S_v \tag{3.67}$$

$$\frac{\partial}{\partial t}(\alpha_l \rho_l) + \nabla \cdot (\alpha_l \rho_l \vec{u}_l) = S_l \tag{3.68}$$

Consider Figure 3.5, in the event the wall is heated, the liquid temperature will rise. When the cell temperature rises above the saturation temperature ($T_{cell} > T_{sat}$) Equation 3.61 will determine the mass transfer. By including the liquid volume fraction in the equation, it is ensured that the mass is 'taken' from the liquid phase. In addition, the cell temperature decreases since the enthalpy of phase change (latent heat) is extracted from the cell. This is done by including a source term in the energy equation which is defined as:

$$S_M = S_l = -S_v \tag{3.69}$$

$$S_E = h_{fg} S_M \tag{3.70}$$

Where S_M represents the source term included in the continuity equation and S_E the source term included in the energy equation. By defining the evaporation and condensation source term in this way, a boundary condition is set for both phases. This boundary condition ensures no vapor has a temperature below the saturation temperature and analogously ensures that no liquid temperature is above the saturation temperature. In addition mass, momentum and energy are conserved in every time step.

On the coefficient r

In literature a wide range of magnitudes for the evaporation/condensation frequency are employed as can be seen in Table 3.2. This table includes most of the literature published since 2000 concerning condensation phase change modeling using the Lee model. Since all presented papers make use of the commercial software FLUENT, the Lee model is probably introduced in FLUENT around 2008. One should note that the condensation frequency is varied from 0.1 to even as high as 1e7. This clearly indicates the case dependency of the condensation frequency. In the next column the interfacial temperature deviation is depicted. This value tells us something about the accuracy of the simulation.

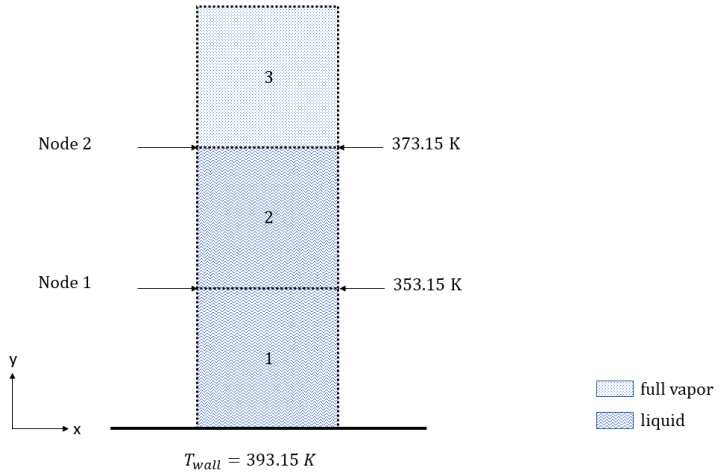

Figure 3.5: Schematic of evaporation process using the Lee model in conjunction with the VOF method in Fluent.

It is defined as the deviation of the interfacial temperature from the saturation temperature. One may note that not all authors publish this indicative figure. In addition no author states 'their' definition of the interfacial temperature. Since the interface is smeared across a few computational cells multiple approaches can be taken in determining the interfacial temperature. In general there exist three consensuses about the evaporation/condensation frequency r which are stated frequently throughout literature:

- r is very case dependent and should be tuned for every configuration [59][60].
- Higher values of r lead to more accurate solutions[57][61][60].
- Higher values of r may lead to stability issues [57][61][60].

Table 3.2: Condensation frequencies used throughout literature

Year	Author(s)	$r[s^{-1}]$ or $f_0[s^{-1}T^{-1}]$	Interfacial temperature deviation	Flow features	Geometry
2009	Da Riva & Del Col [59]	1,000,0000	0.3 K	Laminar film flow	Horizontal mini channel
2009	Alizadehdakhel [62]	0.1		Film flow, mist droplet flow	Thermophyson
2010	Da Riva & Del Col [63]	1,000,000 - 20,000,000	0.5 K	Laminar film flow	Horizontal mini-channel
2011	Da Riva & Del Col [64]	750,000 - 10,000,000	1.2K - 0.5K	Laminar film flow	Horizontal/vertical mini-channel
2012	Da Riva & Del Col [65]	750,000 - 5,000,000	1K	Laminar film flow	Horizontal mini channel
2012	Liu & Sunden [38]	5,000	1K	Laminar film flow/ wavy laminar film flow	Vertical parallel plates
2013	Bortolin, Da Riva & Del Col [66]	1,000,000 - 3,000,000	1K - 1.3K	Laminar film flow	horizontal mini-channel
2014	Qiu [61]	10,000		Stratified, annular & mist flow	Spiral tube
2014	Qiu [67]	10,000		Forced convective upflow condensation: bubbly flow, slug flow, churn flow, wispy annular flow	Vertical pipe (upflow)
2014	Chen [68]	100 (f_0)	0.1K	Annular flow, wavy annular flow, transition flow, slug flow and bubbly flow	Rectangular horizontal micro-channel
2015	Lee [60]	0.1/100/10,000	2K	Film flow with droplets in vapor core	Circular tube (downflow)
2015	Yin [69]	50,000	0.5K	Laminar film flow with/ wihtout non-condensable gas	Horizontal mini tube
2016	Zhang [70]	1,500,000		Film flow	Horizontal round and flattened mini-channels
2016	Zhang [71]	1,500,000	0.5K	Annular flow	Horizontal round circular tube
2016	Kharangate [72]	10,000		Film (annular) flow	Vertical tube (upflow)
2016	Quan Liu [10]	5,000 - 500,000		Laminar film flow, wavy laminar film flow	Vertical plate
2017	Ke [73]	100,000		Droplet condensation, droplet coalescence, droplet jump	Microstructured surface
2017	Shen [6]	10,000 - 10,000,000	1.1K	Film flow	Vertical plate
2017	Szijarto [74]	100 - 5,000		Direct contact condensation	Horizontal channel

As the condensation process is mainly driven by the temperature difference between the interface and the cool wall the evolution of the liquid film thickness is very important. The liquid film determines the local heat transfer coefficient, hence the rate of condensation. However, the introduction of the time relaxation parameter r makes the Lee model rather non-physical, since now the heat and mass transfer is not only driven by the temperature difference but also by an arbitrary coefficient.

From literature one can conclude that higher values of r lead to an interfacial temperature closer to the saturation temperature. However, no one really elaborates on why this happens. Now lets consider 1D condensation as depicted in Figure 3.6. The region is 1D, so we assume the temperature

only changes in the y-direction and the vapor is assumed to by quiescent. In addition the vapor temperature is assumed to be at saturation temperature and the wall temperature is assumed to be constant at 353.15 K. Now lets assume that the mass source term S_l has a magnitude leading to the complete condensation of one computational cell (situation 1), when this cell temperature drops below the saturation temperature. Subsequently, the enthalpy of phase change is transferred from the vapor phase to the liquid phase in one time step, but due to the efficient wall cooling, the temperature stays below saturation temperature. The next time step, there is no mass transferred in his computational cell since the vapor volume fraction is zero, hence the interface has moved one computational cell (from the wall to node 1) in the positive y-direction in one time step.

The above is very logical and seems to do what is done by the Lee model. However, due to the arbitrary coefficient r in the Lee model, the magnitude of transferred mass from the vapor phase to the liquid phase may be too low to ensure complete condensation. Now lets say that the magnitude of mass transfer in cell 1 ensures the condensation of half the computational cell. Then, due to the slightly higher temperature of cell 2, the magnitude of mass transfer in this cell only ensures condensation of one quarter of the computational cell. So the next time step cell 1 has a liquid volume fraction of 0.5 while cell two has liquid volume fraction of 0.25. This means that there exists a multiphase layer of two computational cells, hence an interface of two computational cells. In this way the solution gets "smeared out". Subsequently the interfacial temperature should be considered in two cells instead of one. The result is that due to the lower temperature of cell 1 compared to cell 2, the interfacial temperature decreases.

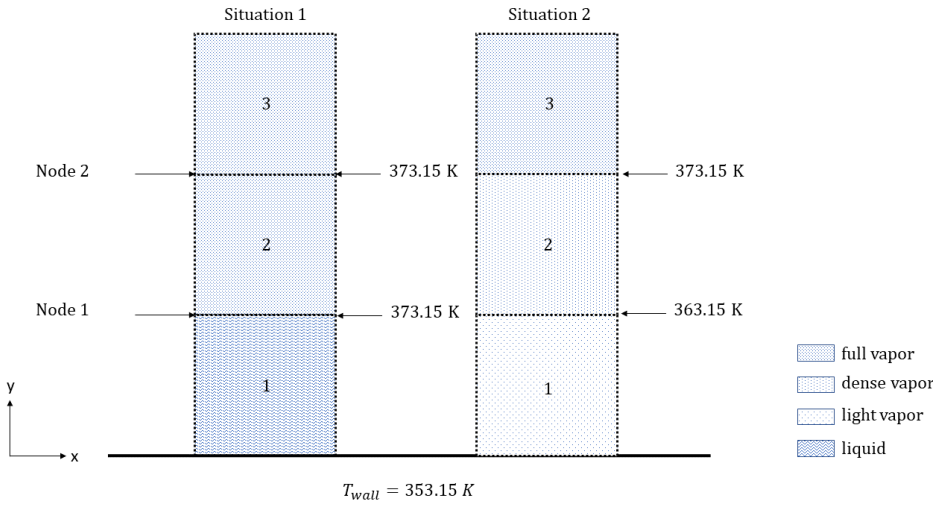

Figure 3.6: Schematic of condensation process using the Lee model in conjunction with the VOF method. Situation 1: full condensation. Situation 2: partial condensation.

Although many authors care to note that using higher values of r may lead to stability issues, no one really addresses the reason. One possible explanation is that the VOF CFL condition is not satisfied locally. According to this condition, the maximum volume that is sunk during one time step should not exceed the volume of the computational cell. Due to the relaxation coefficient r, which is arbitrarily chosen, the mass that will be sunk during one time step could result in not satisfying the VOF CFL condition. Especially condensation may lead to this problem since the specific volume of a vapor is much higher than the specific volume of a liquid.

Hardt and Wondra [75] do stress that a mass source term localized in a very narrow region leads to numerical instabilities. This is in accordance with the previous notion that higher values of r lead to a thinner interface, hence the mass source term is localized, hence stability issues may occur. In their paper Hardt and Wondra introduce a function that smears out the mass source term across multiple neighbouring cells. By introducing an additional scalar field ϕ, the mass transfer rate $\dot{m} = \phi_0$ is distributed over several cells. The mass source term is introduced in the neighbouring cells by solving

a diffusion equation(3.71) that satisfies a Neumann boundary(3.72) condition:

$$\nabla^2\phi = \frac{1}{D}(\phi - \phi_0) \tag{3.71}$$

$$\vec{n}\nabla\phi(\Omega) = 0 \tag{3.72}$$

Where D governs the length scale of the smearing region. The Neumann boundary condition is needed to satisfy conservation of the volumetric integral of the total condensation rate.

The smearing function as proposed by Hard and Wondra is employed several times throughout literature for the simulation of evaporating flows. Until now only one study is known where the smearing function is applied to condensation as well as to the Lee model [74]. By introducing the smearing function a case with a condensation frequency of $r = 2000s^{-1}$ was helped to converge.

Clearly the mass source term in the continuity equation causes stability issues. So lower values for the source term are needed to maintain stability. The question that arises is: is there an optimal trade-of between on one hand stability/convergence speed and on the other hand accuracy. In other words, will a certain magnitude of r cause the solution to be stable, converge quickly and obtain a reasonable accuracy? And will this curve be linear or non-linear (asymptotic)?

Modification by Chen

The classical Lee model was further simplified by Chen [68]. In his definition the saturation temperature T_{sat} from the denominator gets included in the condensation coefficient f_0, resulting in:

$$\dot{m}_{con} = S_l = f_0\alpha_v\rho_v(T_{sat} - T) \tag{3.73}$$

Where f_0 now has the units of $s^{-1}T^{-1}$. When compared to the classical Lee model of Equation 3.60 the modification by Chen brings nothing new, provided that the saturation temperature is constant. In the Lee model included in Fluent the saturation temperature can be assigned by the user, as a constant only. For this reason the modification by Chen is actually completely similar to the Lee model.

Modification by Liu

A different approach to the interfacial surface area is to assume that all vapor bubbles have the same diameter. Now the volumetric interfacial surface can be expressed as [3]:

$$a_i = \frac{6\alpha_v\alpha_l}{d_b} \tag{3.74}$$

Where d_b represents the bubble diameter. This different approach results in a different definition for the mass transfer relaxation parameter r_v:

$$r_v = \frac{6}{d_b}\sqrt{\frac{M}{2\pi RT_{sat}}}\frac{h_{fg}\alpha_l\rho_l}{\rho_l - \rho_v} \tag{3.75}$$

Although r_v is defined differently, this does not necessarily mean that the mass source term S_l will be different compared to the classical approach. The reason for this is that r_v is chosen arbitrarily as a constant and that Equation 3.60 remains the same.

Another approach where Equation 3.60 does change is proposed by Liu et al [10]. In this paper it is stressed that in the traditional approach (3.60), the interfacial surface area is not determined correctly. Namely, a_i depends on the Sauter mean diameter in the following way:

$$a_i = \frac{6\alpha_v}{D_{sm}} = \frac{6\alpha_v}{(6V_V/\pi)^{1/3}} \tag{3.76}$$

Where V_v represents the physical volume occupied by the vapor. In the paper it is said that the interfacial area density should not depend on the total vapor volume, but rather on the vapor volume in one computational cell.

$$a_i = \frac{6\alpha_v}{(6\alpha_v V_c/\pi)^{1/3}} = \left(\frac{36\pi}{V_c}\right)^{1/3}{\alpha_v}^{2/3} \tag{3.77}$$

Where V_c represents the volume of a computational cell. Substituting 3.77 into Equation 3.57, assuming $a_c = 1$ and rearranging results in:

$$\dot{m}_{vl} = r_v {\alpha_v}^{2/3} \rho_v \frac{T_{sat} - T_v}{T_{sat}} \tag{3.78}$$

According to Liu, the results yielded by this model should be closer to 'physical results'. However, no comparison with on the one hand experiments or on the other hand with the classical Lee model is made. In addition, no clear statement is made in what sense the results would be more physical. Nevertheless, this alteration was implemented. Favorable results, compared to analytical Nusselt condensation, in terms of film thickness for vertical downflow condensation were obtained.

Modification by Shen

One of the most recent developments on the Lee model was conducted in 2017 by Shen et al[6]. In this paper a correlation is found between the heat flux on one side and the interfacial temperature difference and the time relaxation parameter r on the other side.

$$q_i \approx (T_{sat} - T_i)\sqrt{A k_v} \tag{3.79}$$

$$A = \frac{h_{fg} r_v \rho_v}{T_{sat}} \tag{3.80}$$

This correlation was found by substituting the mass source term for condensation (S_l) in the energy equation of the vapor phase. In addition it was assumed that the time dependent term and the convective term are negligible compared to the latent heat term.

$$k_v \frac{d^2T}{dx^2} + \alpha_v \rho_v r_v \frac{T_{sat} - T}{T_{sat}} h_{fg} = 0 \tag{3.81}$$

Subsequently, it was assumed that the vapor phase is completely vapor up to the interface ($\alpha_v = 1$) and the equation was integrated. For the full derivation the reader is referred to [6].

By finding this correlation they concluded that for any given heat flux, the interfacial temperature difference depends in the same proportion on the vapor conductivity as on the condensation frequency r. This means that enhancing the vapor conductivity causes the interfacial temperature difference to decrease. As this is a measure for accuracy, one could say that the solution would get more accurate when the vapor conductivity in the two phase region is enhanced. For this reason the conductivity got altered in the following way.

$$k_{eff} = \alpha_l k_l + n \alpha_v k_v, \quad if\ T < T_{sat} \tag{3.82}$$

With k_{eff} the total effective conductivity and n the enhancement factor.

One might imagine that in the undefined two-phase region the effective conductivity should not be fraction averaged and is closer to the liquid conductivity. The two-phase region is more or less undefined since in reality the vapor liquid interface is very thin. However, when using a finite number of grid cells, the two phase region is at least one grid cell thick. In the case the Lee model is employed the interface is even smeared out across a couple of grid cells. For this reason a region appears that is non-physical. However, by enhancing the effective thermal conductivity it is claimed that more physical results are obtained.

In the paper the model is verified by simulating classical Nusselt condensation. In addition a simulation of forced convective downflow condensation in a miniature tube is checked with the results of Da Riva & Del Col [64]. In the Nusselt condensation problem the following five cases are assessed.

where β is changed independently since it governs the shape of the temperature curve while γ governs the model's performance in terms of liquid film thickness. As the ratio of the liquid conductivity to the vapor conductivity is around 30 ($\frac{k_l}{k_v} \approx 30$), an enhancement factor above 30 poses the question if the effective thermal conductivity will be physical. On the other hand, the two-phase region of multiple grid cells is already a questionable region and what if this modeling approach results in a physical solution? In any case, the liquid film thickness obtained by Shen's approach is shown in Figure 3.7.

From the first three cases it is concluded that a higher condensation frequency yields an interfacial temperature closer to the saturation temperature. Also it is concluded that the film thickness

Table 3.3: Cases assessed in Nusselt condensation, from [6]

	r	$k' = nk_v$	$\beta = A/k'$	$\gamma = Ak'$
Case I	$10,000$	k_v	β	γ
Case II	$100,000$	k_v	10β	10γ
Case III	$1,000,000$	k_v	100β	100γ
Case IV	$100,000$	$10k_v$	β	100γ
Case V	$1,000,000$	$100k_v$	β	$10,000\gamma$

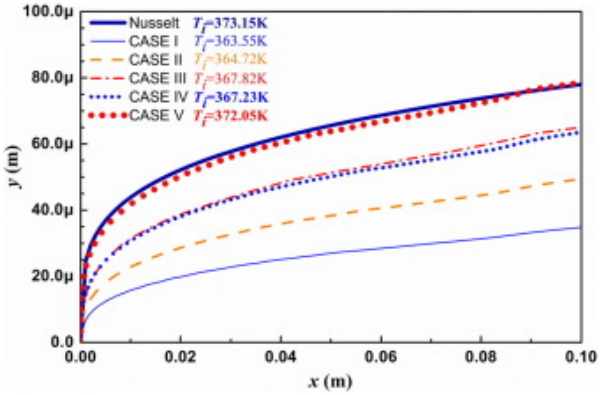

Figure 3.7: Nusselt film thickness and interface temperature yielded by Shen modified Lee model for case I-V, from Shen (2017) [6]

approaches the Nusselt film thickness as r increases. This result indicates that a higher condensation frequency does result in more accurate results, just as stated in section 3.3.3.

Case IV and case V achieve better results compared to the cases with the same condensation frequency but without enhancement of the conductivity. The improvement in interfacial temperature can be explained by the previously derived correlation (Equation 3.79. However, because the mass transfer intensity is not altered, the increase in film thickness is harder to explain. Clearly, the enhancement of the thermal conductivity enables the solution to take different thermal equilibrium compared to the classical Lee model. It will be interesting to find out in why this equilibrium is altered. Energy conservation at the vapor-liquid interface tells us:

$$k_l \frac{dT_l}{dy} = k_v \frac{dT_v}{dy} \tag{3.83}$$

From Equation 3.83 it can be deduced that enhancing the vapor conductivity results in more similar temperature gradients. For this reason the temperature jump across the interface will be more gentle which ultimately smooths the mass transfer rate curve [6]. In [6] better convergence is attributed to the smooth mass transfer curve.

The results by Shen prove that enhancing the conductivity produces more accurate results in terms of interfacial temperature deviation and film thickness, while maintaining stability. Still some questions remain. For instance, does there exist a physical explanation for better accuracy due to conductivity enhancement. Or is the explanation purely numerical? Following, what causes the liquid film thickness to increase while the mass transfer intensity does not change? Finally, it will be interesting to see if apart from producing a stable solution at better accuracy the convergence speed is altered.

3.4. Other approaches

3.4.1. Phase Field

The mass source term in the Phase Field model by Badillo [76] [74], is determined by a local thermodynamic equilibrium at the interface. The main difference with the numerical iteration technique (Lee model), is that the coefficient that governs the mass transfer is not arbitrarily chosen (as opposed to r from the Lee model). The coefficient is determined by an asymptotic analysis of the field equations,satisfying a thermodynamic equilibrium at the interface. For the full derivation the reader is

referred to Badillo [76]. The mass transfer rate is determined from:

$$\dot{m} = \frac{\epsilon_{pf}(T_{cell} - T_s)}{h_{fg}}|\nabla\alpha| \tag{3.84}$$

Where $|\nabla\alpha|$ represents the gradient of the void fraction, and h_{fg} is the latent heat of condensation. The coefficient ϵ_{pf} is governed by the diffusivity of the liquid:

$$D_l = \frac{k_l}{C_{pl}\rho_l} \tag{3.85}$$

and the characteristic length w of the interface, which corresponds to the height of a numerical cell. Now ϵ_{pf} can be written as:

$$\epsilon_{pf} = \frac{6\sqrt{2}}{5}\frac{D_l\rho_l C_{pl}}{w} \tag{3.86}$$

Or for convenience:

$$\dot{m} = \frac{6\sqrt{2}}{5}\frac{k_l}{w}\frac{T_{cell} - T_{sat}}{h_{fg}}|\nabla\alpha| \tag{3.87}$$

Looking at Equation 3.84 one sees that the driving force of condensation is determined by the temperature difference between the interfacial cell and the saturation temperature. So compared to the Lee model, the relaxation of the mass source term is governed by flow and domain properties instead of an arbitrarily chosen coefficient. For this reason it is claimed that the model is thermodynamically more consistent and much more efficient. It is interesting to note that due to the volume fraction gradient term the mass source term will only produce a non-zero value in the case of direct contact condensation. This means that when a particular flow is simulated it has to be known where the vapor will start condensing, since at this location a thin film needs to be patched.

Due to the big property difference between the two phases a correction term has to be included in the energy equation.

$$E_{corr} = (\rho_l C_{p,l} - \rho_v C_{p,v})\frac{w}{\sqrt{2}}\left(\frac{1}{\rho_v} - \frac{1}{\rho_l}\right)\vec{n}_l \cdot \nabla T \tag{3.88}$$

$$S_E = -\dot{m}(h_{fg} - E_{corr}) \tag{3.89}$$

Where S_E represents the source term in the energy equation.

Implementation of the phase field model through a User Defined Subroutine (UDF) in Fluent might pose some difficulties since variables as the numerical cell height and the unit vector of the liquid interface are not easily accessible. In any case this is exactly what was done by Szijártó et al. [74]. Three phase change models, including the phase field model, the classical Lee model and a heat flux balance method based on Equation 3.8, were tested by simulating direct contact condensation of the LAKOON experiment. In addition a smearing function proposed by Hardt and Wondra [75] was used to enhance stability. In their study the phase field approach yielded the most accurate results. However, the phase field method did perform only slightly better than the Lee model. However, it is stressed multiple times that due to the arbitrariness of the Lee model, the phase field model is preferred.

3.4.2. Rattner Model

In order to avoid the computationally expensive operation of interface reconstruction, Rattner [7] proposed a simplistic model for condensation that only acts on mesh connectivity, hence cell faces, and volumetric field data such as temperature, enthalpy etc. Every time step a so-called graph of the mesh is constructed which consists of nodes and edges. The nodes correspond to the cells while the edges correspond the faces. A computationally cheap 'graph' is created since only the volume fraction is saved. Subsequently the graph is screened for *cell pairs* with a volume fraction exceeding the threshold of $\alpha = 0.5$. Now these cell pairs get added to the interface cell set. A graphical representation is shown in Figure 3.8

For this representation of the interface a sufficiently small mesh is needed near the interface. In addition, cell pairs containing a wall boundary condition are added to the set. Therefore, condensation

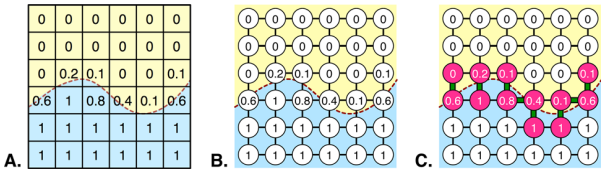

Figure 3.8: Interface cell identification process by Rattner [7]: The phase-fraction field on mesh cells (A) yields a graph (B) from which cell pairs straddling $\alpha = 0.5$ form the interface (C), from [7].

on a wall is also possible. Now using the data of the graph, an initially non-limited volumetric phase change heating rate is added to the energy equation of the interface cell set.

$$\dot{q}_{pc,0} = \rho C_p \frac{T - T_{sat}}{\Delta t} \tag{3.90}$$

By adding the physical time step (Δt) it is ensured that the interface takes the saturation temperature every time step. To meet the mass conservation criterion, the vapor mass taken from a cell in one time step should not exceed the vapor mass available in that computational cell.

$$\dot{q}_{lim,mass} = -\frac{1(\alpha - 1)\rho_v h_{fg}}{\Delta t} \tag{3.91}$$

Analogously, the VOF CFL condition needs to be met every time step. This means that the volume condensed during one time step should not exceed the volume of the computational cell.

$$\dot{q}_{lim,CFL} = -\frac{h_{fg}}{\Delta t}\left(\frac{1}{\rho_v} - \frac{1}{\rho_l}\right)^{-1} \tag{3.92}$$

Finally, the final source term for the energy equation can be derived from:

$$max(\dot{q}_{pc,0}, \dot{q}_{lim,mass}, \dot{q}_{lim,CFL}) \tag{3.93}$$

Since all before stated source terms will have a negative sign, Equation 3.93 will yield the smallest (most conservative) source term. For the complete implementation of the source terms of the continuity and momentum equation, the reader is referred to [7]. In addition the algorithm implementation in OPENFOAM is found in [7].

The proposed phase change model is assessed by means of three tests: horizontal film condensation, smooth falling-film condensation and wavy falling-film condensation. The results for horizontal film condensation were found to almost converge linearly to the analytical solution. Smooth falling-film condensation yielded heat flux values within 2% of the analytical solution, while wavy falling-film condensation yielded heat-transfer rates within 11% of the locus of values of established correlations.

3.4.3. Single Phase Approach

In an approach by Cao [77] the condensate liquid film is assumed to be very thin. By doing so only the heat and mass transfer of the vapor phase is simulated, while the condensate film flow is modeled. By doing so, computer resources and simulation time are said to be saved. The convective behavior between the vapor flow and the liquid film is replaced by multiple boundary conditions. In addition, source terms for mass and heat transfer are incorporated in the continuity and energy equation of the vapor phase respectively. The mass transfer between the phases is based on an energy balance over a control volume. Aside from the latent heat that is transferred from the vapor phase to the liquid phase it is stressed that also the sensible heat is transferred to the liquid phase. By doing this they account for the subcooling effect from the condensate.

The assumption of a very thin liquid film limits this approach to film condensation. In addition, the model is not capable of modeling full condensation, since full liquid flow is not supported in this method.

3.5. Geometries & flow features

In literature flow condensation is widely modeled with different success rates. When flow features get more complicated, much less literature is available. Only a couple of studies have mentioned

modeling more than two flow features successfully. The flow features included are: bubbly flow, slug flow, churn flow and wispy annular flow. Following, some studies focus on modeling single droplet condensation. An overview of the modeled flow features in available literature is shown in Table 3.4.

In two-phase vapor liquid flow, the flow phenomena highly depend on the quality of the mixture. An interesting study that employs various inlet qualities is that of Ganapathy [8]. Ganapathy manages to successfully model the following quality dependent flow phenomena: annular flow, transitional flow and intermittent flow. Figure 3.9 shows the modeled flow regimes compared to experiments. It should be noted that the comparison in Figure 3.9 is purely qualitative. The inlet conditions and geometry do not necessarily correspond to the experimental set-up. However, the study does prove that different condensation flow features can be modeled. In addition the numerical model is tested by comparing the

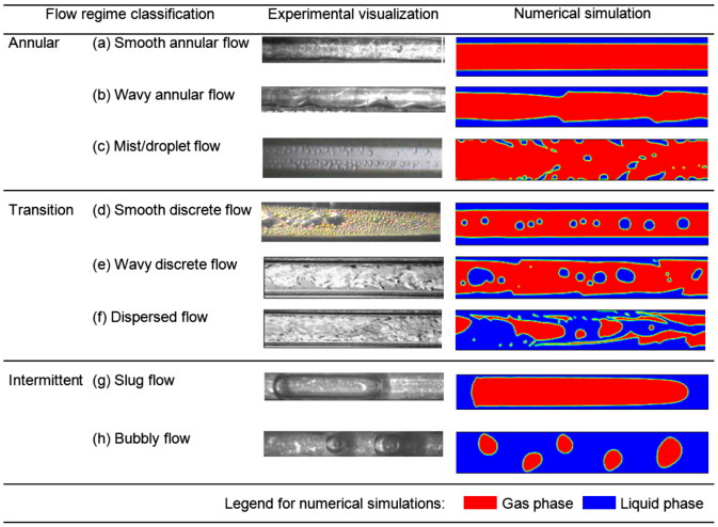

Figure 3.9: Comparison of CFD simulated two-phase condensation flow regimes with experimental visualization data in literature, from [8].

two-phase frictional pressure drop and the two-phase Nusselt number to data extracted from empirical correlations. The maximum absolute error (MAE) between the predicted and the empirical pressure drop was 8.1% while the Nusselt number was predicted within 16.6 % of the MAE.

Flow features relevant for plate heat exchangers are mainly dependent on the application, since the inlet and outlet vapor quality determine the flow regimes present. So depending on the desired application, certain flow regimes and model capabilities are interesting. In literature most authors start validating their model with a more straight-forward case such as Nusselt film flow. This case can be considered more straight-forward since no complicated inflow conditions are needed. In addition, it can be tested if the phase change model is able to produce liquid, without pre-existing liquid present. Looking at Table 3.4, a variety of studies have been conducted modeling laminar film condensation, wavy laminar film condensation up to fully turbulent film condensation. Also film condensation driven by gravity with a quiescent vapor phase has been modeled.

The last column of Table 3.4 shows the geometries considered in literature. Noticeably, only rather simple geometries such as rectangular of circular channels are modeled. Also in the case of a thermo-physon, only a small part, which corresponds to a circular channel, is modeled.

So from literature it is concluded that, in simple geometries, CFD is capable of predicting multiple two-phase phase change flow phenomena. However, in plate heat exchangers one can imagine that the present corrugations might lead to separation of the liquid film. In addition, the separated liquid might subsequently coalesce again or maybe it completely breaks up into multiple bubbles. From literature it is not clear if the available CFD models are capable of modeling such complicated flow features. For that reason it will be interesting to investigate the performance of available CFD models when complicated flow phenomena as separation are triggered.

Table 3.4: Flow features and geometries featured in condensation modeling

Year	Author(s)	Multiphase model	Phase change model	Flow features vapor	Flow features liquid	Geometry
2001	Zhang[78]	VOF	Heat flux balance	Laminar flow	Laminar film flow	Horizontal miniature tube/parallel plates
2006	Yuan[79]	Directly solved	Heat flux balance	Laminar flow	Laminar forced convective film condensation	Vertical parallel plates
2009	Da Riva & Del Col[59]	VOF	Lee model	Laminar / turbulent flow	Laminar convective film flow	Horizontal mini channel
2010	Alizadehdakhel[62]	VOF	Lee model	No information available on vapor velocity,vapor with non-condensable gasses	Film flow, mist droplet flow	Vertical thermosyphon
2010	Da Riva & Del Col[63]	VOF	Lee model	Turbulent flow	Laminar film flow	Horizontal circular mini channel
2010	Nebuloni[80]	VOF	Schrage (modified)	Laminar/turbulent flow	Laminar annular film flow	Horizontal micro/mini channels, various channel shapes
2011	Da Riva & Del Col [64]	VOF	Lee model	Turbulent flow	Laminar/turbulent film flow	horizontal/vertical mini channel
2012	Da Riva & Del Col[65]	VOF	Lee model	Turbulent flow	Laminar/turbulent film flow	Circular horizontal mini channel
2012	Liu & Sunden[38]	VOF	Lee model	Laminar flow	Laminar film flow, wavy laminar film flow	Vertical parallel plates
2013	Ganapahty[8]	VOF	Heat flux balance	Laminar flow	Smoothe annular, wavy annular, mist, smooth discrete, wavy discrete, dispersed, slug, bubbly	100mu horizontal micro channel
2013	Bortolin, Da Riva & Del Col[66]	VOF	Lee model	Turbulent flow	Laminar/turbulent film flow	Horizontal square mini channel
2014	Sun[81]	VOF	Heat flux balance	Quiescent	Single bubble direct contact condensation	-
2014	Qiu[67]	VOF	Lee model	Turbulent flow	Turbulent flow, stratified, annular & mist flow	Spiral tube
2014	Qiu[61]	VOF	Lee model	Turbulent flow	Turbulent upflow condensation: bubbly flow, slug flow, churn flow, wispy annular flow	Vertical pipe (upflow)
2014	Chen[68]	VOF	Lee model (modified)	Laminar flow	Convective, Annular flow, wavy annular flow, transition flow, slug flow and bubbly flow	Rectangular horizontal microchannel
2014	Rattner[7]	VOF	Rattner model	Quiescent	Horizontal film condensation, smooth and wavy laminar falling-film condensation	-
2015	Lee[60]	VOF	Lee model	Turbulent flow	Film flow with droplets in vapor core	Circular tube (downflow)
2015	Yin[69]	VOF	Lee model	Laminar flow with and without non-condensable gasses	Laminar film flow	Horizontal mini tube
2016	Zhang[70]	VOF	Lee model	Turbulent flow with vortex formation	Annular flow	Horizontal round and flattened minichannels
2016	Zhang[71]	VOF	Lee model	Turbulent flow	Annular flow	Horizontal round circular tube
2016	Kharangate[72]	VOF	Lee model	Turbulent upflow	Film (annular) flow, complex flow characteristics during flooding and climbing such as interfacial waviness, formation of liquid ligaments along the film's interface and break up of liquid masses from these ligaments that are either redeposited onto the film or entrained in the vapor core before moving towards the centerline.	Vertical circular tube (upflow)
2016	Quan Liu[10]	VOF	Lee model (modified)	Laminar flow	Laminar film flow, wavy laminar film flow	Vertical plate
2016	Samkhaniani [82]	CF-VOF	Tanasawa	Quiscent	Bubble condensation in subcooled water	-
2017	Datta[83]	VOF	Heat flux balance	Quiscent	Single vapor bubble condensation in subcooled water	-
2017	Ke[73]	VOF	Lee model	Quiscent	Droplet condensation, droplet coalescence, droplet jump	Microstructured surface
2017	Shen[6]	VOF	Lee model (modified)	Laminar flow	Film flow, wavy film flow	Vertical plate
2017	Szijarto[74]	VOF	Lee/Heat flux balance/Phase field	Laminar flow	Film flow, DCC condensation	Horizontal channel
2017	Cao[77]	Single phase, with BC's for liquid phase	Heat flux balance	Turbulent flow	Film flow	Vertical cylindrical channel
2018	Fertahi[84]	VOF	Lee model	-	Film flow, bubbly flow	Thermosyphon

3.6. Summary & remaining questions

In this section a small summary of the phase change models used for condensation will be presented by answering relevant sub-questions. In addition implementation and validation of the models will briefly be addressed. Finally two remaining questions will be discussed.

3.6.1. Summary

What phase change models are employed?

Phase change models are mainly based on two approaches. In the first one, the mass source term is derived by conducting an heat flux balance at the interface. This approach is widely used in literature. The second approach is to derive the mass source term from the kinetic theory of gasses. The first one to modify the classic Hertz-Knudsen equation in order to account for kinetic effects was Schrage. This resulted in the Schrage model. Tanasawa simplified the Schrage model by making the mass source term linearly dependent on the temperature jump across the interface. Both models need to be multiplied by the gradient of the volume fraction in order to obtain the source term in $kg/(m^3s)$. A further simplified version of the Schrage model is the Lee model, also referred to as the numerical iteration technique. Using the Clausius-Clayperon equation and the introduction of a parameter r (condensation or evaporation coefficient) resulted in a model that operates at a quasi- thermo- equilibrium and constant pressure. Mass transfer is driven by a small temperature deviation from the saturation temperature. So when the vapor temperature drops below the saturation temperature, condensation mass transfer occurs. A further simplified version of this model is the Chen model. Both models are very dependent on the condensation coefficient r. This coefficient must be correctly chosen for each case. The solution is very dependent on this coefficient in terms of accuracy and stability. Low values of r may lead to convergence but poor accuracy while high values of r lead to high accuracy but may pose convergence problems. Since this coefficient is arbitrarily chosen, the physical base of the Lee model is questionable. However, the Lee model is the most popular model in literature (20/29 studies employ this or a modification of this model). Some efforts have been made to overcome the arbitrariness of the condensation coefficient (including the Chen model). However no real comparison between these modifications have been conducted. Three other approaches emerged from literature. In one approach, the mass source term was derived from a phase field approach. In this paper also a comparison between the Energy jump method, Lee model and the phase field method was provided. The phase field method was found to predict the experiments of the Lakoon experiment best. However, the experiment consisted of direct contact condensation (condensation of vapor on water) in a horizontal channel. Also the predictions of the Lee model were close to predictions by the phase field method. The second model (Rattner model) relates the mass flux linearly with the cell temperature deviation from the saturation temperature divided by the numerical time step. Therefore the model is time step dependent, but it also overcomes the arbitrariness of the Lee model. The model was assessed by modeling the 1D Stefan problem. Results predicted by the model were compared with results produced by the Lee model and an energy jump model proposed by Sun. The single phase approach by Cao addresses the problem of computational effort by only simulating the heat and mass transfer of the vapor phase. The condensate film flow is modeled, and the convective behavior between the liquid phase and vapor phase are linked through multiple boundary conditions.

What flow features have been modeled?

In literature flow condensation is widely modeled with different success rates. When flow features get more complicated, much less literature is available. Only a couple of studies have mentioned modeling more than two flow features successfully. The flow features included are: bubbly flow, slug flow, churn flow and wispy annular flow. Following, some studies focus on modeling single droplet condensation.

What geometries have been modeled?

A wide variety of geometries have been modeled. Most frequent are simulations of horizontal/vertical rectangular/round mini/micro channels. More complicated geometries are very rare. In two cases a thermosyphon is modeled and in one case a wick structure. Also a microstructured surface is modeled. Interesting to note is that the CFD calculations concerning the thermosyphon were used for optimization purposes. In general no geometries have been modeled that represent a full PHE, however, the thermosyphon models materialize a careful optimism about phase change modeling in full PHE's.

What software is employed for implementation?

Most models are implemented through the user defined subroutines provided by Ansys Fluent. Occasionally, OPENFOAM is employed or the model is completely self-developed.

How are the models validated?

Validation can be achieved in multiple ways. Two popular analytical approaches are to compare the modelled solution with the analytical solutions of the Nusselt or the Stefan problem. In these cases the interface position gets checked. Authors also use the empirical correlations provided by literature to validate their models. Heat transfer coefficients/ wall temperatures are checked in this way. Finally, experiments are used to check HTC's and flow visualization. Interesting to note is that many authors use their model to conduct parametric studies. So the model is validated with a simplified case-study (Nusselt, Stefan) and subsequently the model is used to predict flow phenomena in a different configuration.

3.6.2. Remaining questions

Model performance in terms of accuracy and CPU time

From literature no distinct difference in accuracy per phase change model can be derived. Often, models are said to be in good agreement with experiments/analytical solution. However, no statements concerning computational effort are made. This leads to the suggestion that all models provide good accuracy if CPU effort is not taken into account. From own experiences, obtaining a converged solution may prove difficult, not to mention obtaining an accurate solution. Since in literature this problem is (almost) not addressed it will be interesting to compare accuracy vs CPU effort for various (or modifications of) phase change models. The above can be summarized into two questions:

- How will the practicality of the phase change models be affected by accuracy requirements?
- What phase change model will perform best in terms of practicality vs accuracy?

Modeling of complicated flow features

As mentioned before, the flow features that are modeled are limited to flow features caused by flow quality. However, in plate heat exchangers complicated flow phenomena as separation or circulation are important for the heat transfer. For this reason it is evident that, in order for CFD to be a predictive tool, CFD has to be capable of modeling these complicated flow features. Therefore, it will be interesting to assess the performance of the available phase change models in simulating a flow with separation or circulation.

4

Practical assessment of phase change models applied to condensation in Fluent

4.1. Introduction

The main aim of this chapter is to investigate the available phase change models in terms of implementation and performance and ultimately answer the questions stated in section 3.6.2. The test environment is restricted to the commercial software package Ansys Fluent 18.1. In this package, only the classical Lee model is available by default. Other models or modifications will be implemented through the User Defined Function environment of Fluent. For extra information on the user-defined functions used throughout this work the reader is referred to Appendix C.

Objectives

- Provide a comprehensive view on the difficulties to modeling condensation by examining the implementation difficulties in terms of stability and convergence speed.
- Present a thorough comparison of the performance in terms of accuracy vs CPU effort of the available phase change models.

Restrictions

- The phase change models must be implementable in Fluent 18.1.
- The phase change models can be employed in a finite volume VOF interface tracking environment.

Comparison

- The phase change models will be verified and compared by modeling the vertical Nusselt condensation problem.
- The set-up by Liu [10] will be taken as a reference case for comparison and validation purposes.

4.2. Set-up

4.2.1. Nusselt Film Condensation

Laminar film condensation on a vertical wall

In order to check and compare the available phase change models, a benchmark condensation problem is needed. Moreover, the condensation control problem should preferably be an analytical exact solution. In this way, no experiments have to be conducted, saving time and avoiding measurement errors. For this reason the phase change models are checked with the Nusselt condensation problem. Nusselt [85] was the first one to develop an analytical model on vertical film condensation along a flat plate. This theory was further developed and is nowadays widely accepted. The theory of the vertical

Nusselt condensation is taken from "Fundamentals of heat and mass transfer" by F. Incropera [9]. In order to arrive at the solution for the analytical film thickness four assumptions are made:

- The liquid film flow is laminar and the material properties of the liquid are constant throughout the film.
- The gas phase is assumed to be purely vapor. Moreover the temperature of the vapor is constant throughout the domain. So no temperature gradient is present. Energy transfer at the liquid-vapor interface is governed by condensation.
- The shear stress at the liquid-vapor interface is negligible. Together with the assumption of constant temperature in the vapor phase, the temperature and vapor boundary layer shown in Figure 4.1**a** do not have to be considered.
- Due to the low film velocity, momentum and energy transfer by advection in the liquid film is negligible. Heat transfer only takes place through conduction in the liquid film. Therefore the temperature distribution is linear, as shown in Figure 4.1**b**.

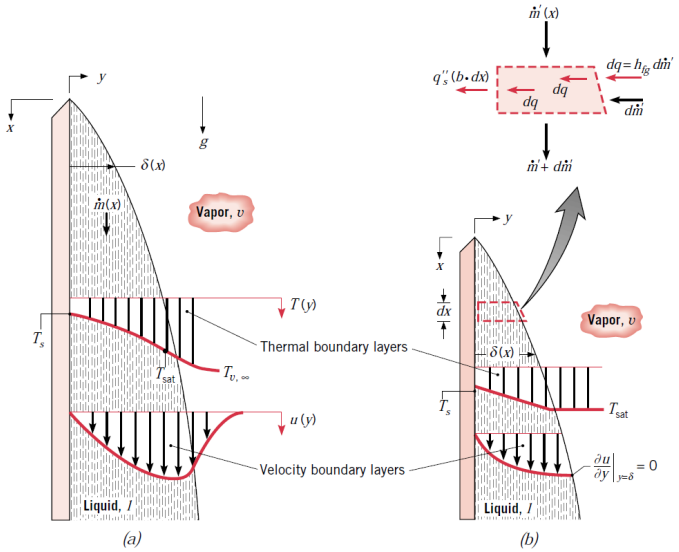

Figure 4.1: Boundary layer effects in vertical film condensation without (**a**) assumptions, with (textbfb) assumptions, from [9].

The laminar liquid film flow can be treated as a boundary layer flow. A boundary layer flow is assumed to be a steady two-dimensional flow of incompressible fluid with constant properties. In addition the following assumptions are made:

- The boundary layer pressure gradient in the streamwise direction $(+x)$ can be approximated as the free stream $(+x)$ pressure gradient : $\frac{\partial p}{\partial x} = \frac{dp_\infty}{dx}$
- The boundary layer (liquid film) is assumed very thin compared to the object (plate). Therefore the gradients along the plate are very small compared to the gradients normal to the plate: $\frac{\partial^2 u}{\partial x^2} << \frac{\partial^2 u}{\partial y^2}$

Using the above assumption the Nusselt film thickness in Equation 4.1 is derived. For the full derivation the reader is referred to Appendix B.

$$\delta(x) = \left[\frac{4k_l\mu_l(T_{sat} - T_w)x}{g\rho_l(\rho_l - \rho_v)h_{fg}}\right]^{1/4} \tag{4.1}$$

In order to account for thermal advection in the liquid film the definition of the latent heat was modified by Nusselt and Rohsenow according to

$$h'_{fg} = h_{fg} + 0.68C_{p,l}(T_{sat} - T_w) = h_{fg}(1 + 0.68Ja) \tag{4.2}$$

where Ja represents the Jacob number and is defined as the ratio of the sensible heat to the latent heat absorbed or released during the phase change process:

$$Ja = \frac{Cp(T_w - T_{sat}}{h_{fg}} \tag{4.3}$$

The local heat transfer coefficient can be expressed as

$$q"_w = h(T_{sat} - T_w) \tag{4.4}$$

Using Fourier's law and Equation 4.1 the local heat transfer coefficient can be deduced. Hence

$$h = \frac{k_l}{\delta} \tag{4.5}$$

$$h = \left[\frac{g\rho_l(\rho_l - \rho_v)k_l^3 h'_{fg}}{4\mu_l(T_{sat} - T_w)x}\right] \tag{4.6}$$

Correction for the vapor velocity

In the event of a vapor flow, the flow will act on the liquid-vapor interface and subsequently a shear stress will be present. In order to account for the shear stress, the third assumption must be altered to:

$$\mu_l \frac{\partial u}{\partial y}|_{y=\delta} = \tau_i \tag{4.7}$$

$$\tau_i = C_f \frac{1}{2}\rho_v U_e \tag{4.8}$$

Where τ_i represents the shear stress at the interface. C_f is referred to as the skin friction coefficient while U_e represents the free stream velocity of the vapor. In the determination of C_f it should be taken into account that the liquid-vapor interface is permeable. Whereas normally a skin friction coefficient is determined under the assumption of zero velocity normal to the surface. The normal component of the velocity is also referred to as *suction* at the surface. At high interface suction the shear stress exerted on the liquid interface can be interpreted as the momentum loss due to deceleration of the impinging vapor particles from their free stream velocity U_e to the liquid film velocity u_δ. The shear stress due to suction can be much higher than the shear stress without suction. The shear stress at the liquid-vapor interface is determined according to:

$$\tau_i = \mu_v \frac{dU}{dy}|_{y=\delta} = \dot{m}"(U_e - u_\delta) \tag{4.9}$$

Where $\dot{m}"$ represents the mass flow rate per unit area. For the full derivation the reader is referred to "Basic Heat and Mass Transfer" by A.F. Mills[31]. Now, for $\rho_v << \rho_l$ and $u_\delta << U_e$ the local heat tranfer coefficient can be determined according to:

$$h' = \left[\frac{k_l^2 U_e}{8\nu_l x}\left\{1 + \left(1 + \frac{16Pr_l}{Ja_l}\frac{gx}{U_e^2}\right)^{1/2}\right\}\right] \tag{4.10}$$

Under the assumption of linear temperature distribution in the liquid film and using Equation 4.5 the corrected liquid film thickness can be determined by:

$$\delta'(x) = \frac{k_l}{h'} \tag{4.11}$$

4.2.2. Material properties

Correction for Variable fluid properties

In the process of film condensation, the film temperature changes with the liquid film thickness. At the subcooled wall, the film takes the wall temperature, while at the liquid vapor interface, the film is near saturation temperature. Material properties as density, specific heat, thermal conductivity and viscosity depend on the temperature. Therefore, when specifying the material properties, the non uniformity in terms of temperature of the liquid film should be taken into account.

Denny and Mills [86] developed a reference temperature scheme to account for the subcooled liquid variable fluid properties. The scheme is restricted to condensation of saturated vapor on a vertical surface at normal gravity. In addition, the scheme only applies to high Prandtl number fluids. In this scheme the latent heat is defined as:

$$h'_{fg} = h_{fg} + 0.35C_{p,l}(T_{sat} - T_w) \tag{4.12}$$

Where h_{fg} represents the latent heat evaluated at the saturation temperature and T_{sat} and T_w represent the saturation and the wall temperature respectively. All variable fluid properties, like the specific heat $C_{p,l}$, should be evaluated at the reference temperature T_r:

$$T_r = T_w + \zeta(T_{sat} - T_w) \tag{4.13}$$

In Equation 4.13, ζ is a dimensionless parameter which defines the degree of the subcooling effect. According to [86], ζ proved to be weakly dependent on all parameters except fluid species. Subsequently, ζ values corresponding to particular fluids could be selected. Other parameters that are already neglected in the Nusselt solution and that might introduce errors are the convective and inertial effects. Due to the weak dependency of ζ on all parameters except fluid specie, the use of ζ only introduces a maximum error of two percent in the local heat transfer coefficient. Values for ζ can be found in "Basic Heat and Mass transfer" by Mills [31]. For fluids not listed by Mills, Equation 4.14 should be used for determining the alternative latent heat:

$$h'_{fg} = h_{fg} + +\left(0.683 - \frac{0.228}{Pr_l}\right)C_{p,l}(T_{sat} - T_w);\ Pr_l > 0.6 \tag{4.14}$$

with Pr_l the liquid Prandtl number and h_{fg} evaluated at T_{sat}. All other fluid properties are evaluated at the mean film temperature.

Properties

The water-liquid and water-vapor properties used for all tests presented in this chapter are shown in table 4.1. It should be noted that the driving force of condensation is a wall with a constant temperature at $T = 353.15K$. Subsequently, the reference temperature for water ($\zeta = 0.33$) resulting from Equation 4.13 is as follows: $T_r = 360K$.

Table 4.1: Material properties

	Evaluated @ $T[K]$	$\rho[kg/m^3]$	$C_p[J/kgK]$	$k[W/mK]$	$\mu[kg/sm]$	H $[J/kgmol]$
Water-liquid	360	967.1	4203	0.674	0.000324	7549089
Water-vapor	373.15	0.5956	2029	0.0248	0.000012	4.821e7

Fluent deduces the enthalpy of phase change from the difference between standard state enthalpies at saturation temperature. Since the enthalpies have to be entered in $[J/kgmol]$, the enthalpies have to be multiplied by the molecular weight of water. All properties presented in this section can be found in [9].

4.2.3. Domain & Grid

The domain considered in this chapter is inspired by the domain of Liu et al[10] and is shown in Figure 4.2. The modeled 2D domain is shown on the left while the domain that defines the 3D structure is shown on the right. By taking a $40mm$ width in two directions it is ensured that surface tension effects in the corners of the physical domain do not have to be taken into account. Therefore, the flow can be modeled as 2D. In addition, the gradients of temperature, velocity and volume fraction

can be assumed zero at the symmetry boundary. Saturated vapor flows into the domain with a velocity of $0.5\ m/s$.

As stated in [10] the length of the adiabatic wall in the upstream region is chosen so that influence of the inlet boundary condition is avoided. In the paper by Liu also an adiabatic wall in the downstream region was included to avoid outflow boundary effects. However, no significant differences were witnessed between cases with and without adiabatic wall. This sounds logical since no backflow was observed. For this reason the adiabatic wall in the outflow region was discarded.

The wall that ensures subcooling of the vapor has a temperature of $353.15\ K$, yielding a temperature difference of $20\ K$ between the wall and the saturated vapor temperature. One might note that the inflow velocity profile is constant, while in reality a fully developed flow would be present. Moreover, a fully developed inflow boundary condition is known to enhance convergence speed. But, in order to be able to compare the results to the results of Liu et al, a constant velocity profile is chosen. Besides, the comparison of CPU effort is not jeopardized when all other boundary conditions are kept the same. Finally, a pressure outlet boundary condition is specified at the outlet.

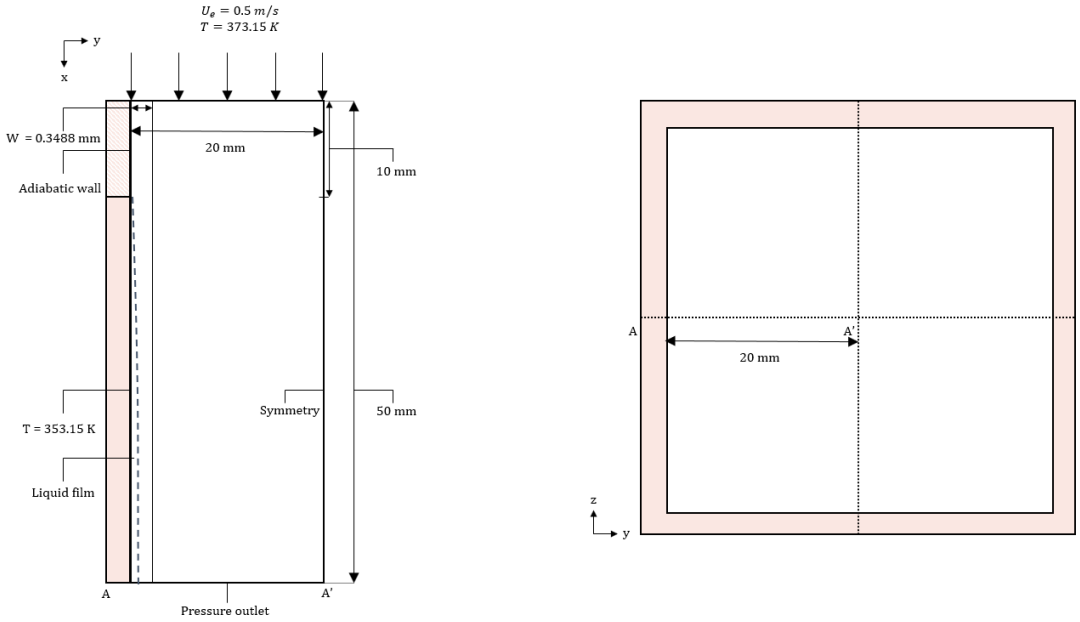

Figure 4.2: Domain and boundary conditions considered in modeling Nusselt condensation problem.

In the paper by Liu a first cell width (direction normal to the wall) of $0.005mm$ is used next to the wall. Subsequently it is stated that the dense mesh layer grows with a grow factor of 1.05 for 30 consecutive cells. This means that the dense layer that is used to capture the liquid film has a width of:

$$width = \sum_{n=1}^{30} 0.005 \cdot 1.05^n = 0.3488\ mm \tag{4.15}$$

Gambit 2.4.6 was used to create the dense mesh layer. In order to have a slightly denser mesh close to the wall, the first cell width was reduced to $0.0019\ mm$. Using a growth factor of 1.1 yields the same layer width W as used by Liu. The specification for the cell count in the stream wise direction was directly taken from Liu yielding the mesh in Figure 4.3.

Before incorporating the layer width of Liu an approximation of the liquid film thickness was made using Equations 4.1 , 4.10 and 4.11:

$$\delta'(x = 40\ mm) = 0.071\ mm \tag{4.16}$$

Equation 4.16 tells us that the liquid film will fall well within the dense mesh layer shown in 4.3. Moreover, by specifying that the mesh close to the wall is somewhat more dense, it is expected that

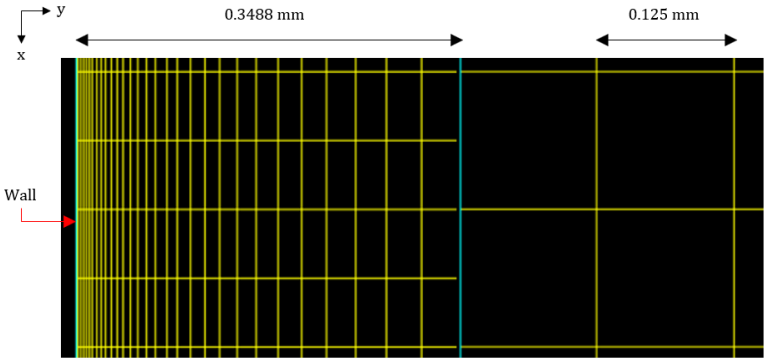

Figure 4.3: Mesh used in simulations, left: dense near-wall region, right: coarse vapor-only region.

the phase interaction will be captured accurately. In addition, the mesh near the wall is able to capture the liquid accumulation in an earlier stage than when the mesh was uniformly sized. This is important when no pre-existing liquid is present.

In the outer region, where only vapor is present, the mesh consists of quadrilateral elements with sides of $0.125\ mm$. This specification yields an element count of 400 in the streamwise direction and 157 in the wall normal direction. Since no phase interaction will be present in this region a much coarser grid is appropriate to capture the flow phenomena. Moreover, a coarser grid is less demanding to the CPU effort. Now the total cell count yields 86800 which is slightly higher (74500) than the highest cell count employed by Liu.

4.2.4. Model set-up

The employed models, methods and solution controls are shown in Table D.2. The multiphase Volume Of Fluid method is used to account for the two phases. Since both phases are assumed laminar, the viscous laminar model is used. In addition the Energy equation is turned on to account for heat transfer.

In the multiphase model panel it is important to include the implicit body force simulation. According to the Fluent manual [30] the implicit formulation enhances solution convergence by accounting for the partial equilibrium of the pressure gradient and body forces in the momentum equations.

As in the paper by Liu, pressure-velocity coupling is accounted for by the PISO scheme, while the spatial discretization of momentum and energy is accounted for by the QUICK scheme. According to the Fluent user's guide the PRESTO! scheme is recommended for flows in strongly curved domains. The domain considered is flat. However, in the next stage of the research a curved domain will be considered. Therefore the PRESTO! scheme will be employed to enhance comparability. In addition, using the VOF method without PRESTO! proved to be prone to stability issues.

In the paper by Liu et al, the Geo-Reconstruct scheme is used for the interface reconstruction. This scheme is said to be more accurate than the other schemes available for interface reconstruction [3]. However, it was found that the Modified HRIC scheme yielded the same accuracy, in terms of mean film thickness, as the Geo-Reconstruct scheme. Moreover, the calculation time needed to reach convergence decreased when using the Modified HRIC scheme. Since the accuracy of the models will be tested by comparing the mean film thickness with the Nusselt film thickness, the modified HRIC scheme is chosen. Finally, time integration is handled by the explicit formulation of the VOF-method.

4.2.5. Convergence & Real Computation Time

Convergence was checked by analyzing the mean heat transfer coefficient of the subcooling wall. The solution was found to be converged when the mean heat transfer coefficient became constant for at least 0.025 seconds. MATLAB was used to read and process the generated HTC data. For the sake of comparability a certain threshold for convergence was defined by analyzing the most unstable heat transfer signal. When the mean heat transfer coefficient was constant for at least 0.025 seconds, and the amplitude did not exceed the amplitude of the most unstable converged heat transfer signal, the

Table 4.2: Model Set-Up

General	
Pressure based, transient, 2D	
Multiphase VOF, Viscous Laminar, Energy On	
Multiphase model	
VOF	
Volume Fraction Parameters Formulation	Explicit
Volume Fraction Cuttof	1e-6
Courant Number	0.25
Body Force Formulation	Implicit Body Force
Interface Modeling	Sharp
Solution Methods	
Pressure velocity coupling	
Scheme	PISO
Skewness Correction	1
Neighbor Correction	1
Skewness-Neighbor Coupling	On
Spatial Discretization	
Gradient	Least Square Cell Based
Pressure	PRESTO!
Momentum	QUICK
Volume Fraction	Modified HRIC
Energy	QUICK
Transient Formulation	First Order Implicit
Under Relaxation	
Pressure	0.3
Density	1
Body Forces	1
Momentum	0.7
Vaporization Mass	1
Energy	1

solution was found to be converged. When the solution did not reach this threshold, the solution was aborted and considered 'not converged'. A fixed time step in the range of $5 \cdot 10^{-5} - 5 \cdot 10^{-7}$ s was employed in all cases. The time step was chosen so that the solution remained stable. The condensation coefficient r proved to be leading in the stability of the solution. Meaning that one should decrease the time step size parallel to an increase in the condensation coefficient. Due to the small time steps needed to ensure stability, the yielded mean global Courant number is smaller than 0.1. During one time step, a maximum of 200 iterations was allowed, while continuity and momentum were found to be converged when the scaled residual dropped below $1 \cdot 10^{-4}$. The scaled residual threshold of energy was set to $1 \cdot 10^{-6}$.

4.2.6. Grid independence

In the grind independence tests, the condensation coefficient was $r = 5000\ s^{-1}$ for all cases. In conjunction with the condensation coefficient a time step of $5 \cdot 10^{-5}$ s was needed to ensure stability.

Streamwise

Grid independence is checked in the streamwise direction by testing three different grids. The three meshes are shown in Table 4.3, where the first mesh corresponds to the mesh presented in section 4.2.3. The number of cells of the 'vapor only' and the 'dense layer' region in both the streamwise and the wall normal direction are depicted. Also the total number of cells is shown. By altering the mesh resolution of the two regions independently and simultaneously, grid independence is thoroughly checked.

Table 4.4 shows the results from the streamwise grid Independence tests. In the second column

Table 4.3: Meshes tested in streamwise grid independence study

Grid	Streamwise Vapor Region	Streamwise Dense layer Region	Wall Normal Vapor Region	Wall Normal Dense Layer	Size Vapor Region [mm]	Total
800	400	800	157	30	0.125x0.125	86800
400	400	400	157	30	0.125x0.125	74800
200	200	200	79	30	0.250x0.250	21800

Table 4.4: Heat transfer coefficient and convergence time for three streamwise different grids

Grid	HTC $[W/m^2K]$	Total Real Time Until Convergence [hr]
800	690.7959	8.01
400	690.5047	7.55
200	690.4552	5.15

the area averaged heat transfer coefficient of the subcooling wall is shown. Also the total real time until convergence is listed in column three. As can be seen all HTC's lie within 0.1% of each other. This means that for all grids a grid independent solution in the streamwise direction is obtained. As expected, the total convergence time decreases for coarser grids. It should be noted that the depicted test comprises of flow phenomena that change slowly in the streamwise direction. Therefore a coarse grid is able to capture all important flow features. However, when the flow changes more rapidly in the streamwise direction, as for instance is the case when the formation of surface waves is of particular interest, a coarse grid might not be able to capture all flow features.

Wall normal

A grid independence study was conducted for five different grid configurations. Since phase interaction acts mainly in the wall normal direction the focus was to find a wall normal independent solution. Moreover, refinement was only performed in the dense layer region. As the flow is only expected to change rapidly in the dense layer region, only this region subjected to a grid independence test. In other words, the dense layer region is expected to be large enough to not to be influenced by the vapor flow in the coarse region.

The cell size distribution in the wall normal direction is shown in Figure 4.4. The numbers in the legend correspond to the number of layers in the wall normal direction. The base case mesh comprises of 30 layers, like the mesh reported by Liu [10]. However, as pointed out previously (section 4.2.3), the distribution closer to the subcooling wall is more dense compared to the original distribution by Liu. The original distribution is also shown in Figure 4.4 under the label 'Liu'. Also, the stars in the plot show where the sum of the layers exceeds the expected film thickness. For example, for the 60 layers grid, the film will be captured by 45 grid cells.

In addition to the five different grids, a case is tested with a fully developed velocity profile inlet condition. This test case has the label 'VP' (velocity profile).

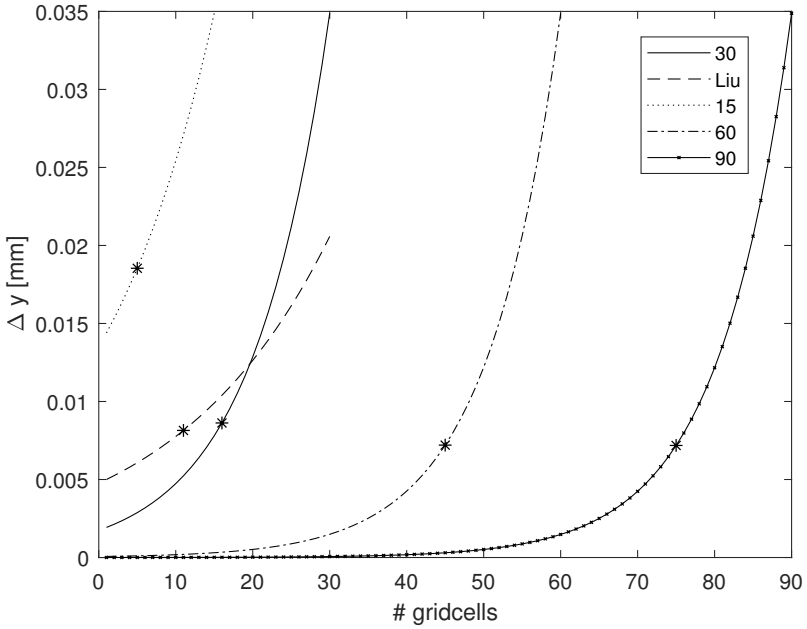

Figure 4.4: Increase of cell size in wall normal direction in dense mesh layer for different grids. Star indicates the position of the maximum expected Nusselt thickness.

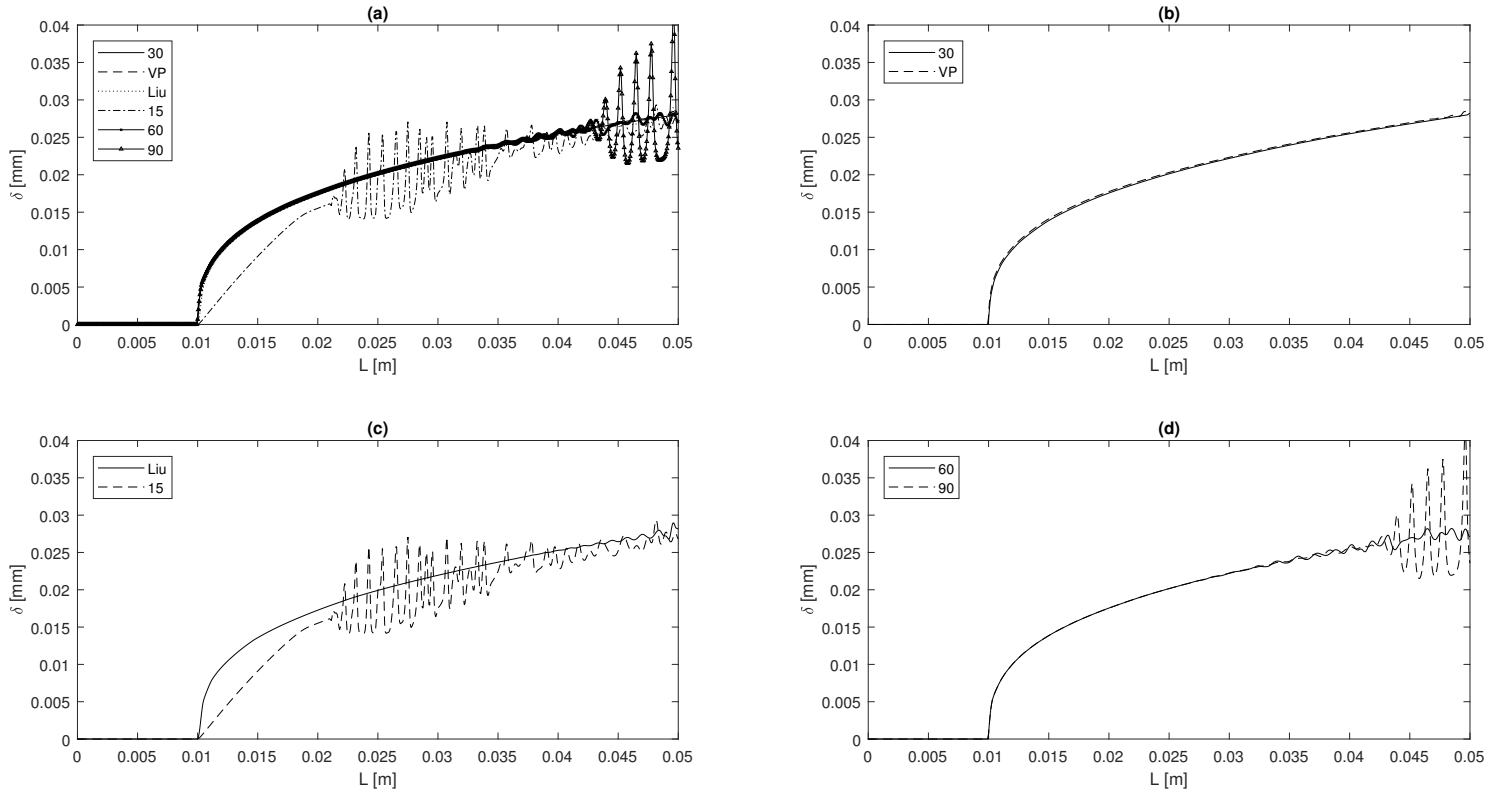

Figure 4.5: Grid independence tests showing liquid film thickness vs plate length for grid 15, 30, 60, 90 and grid 'Liu'. VP indicates fully developed inlet vapor velocity profile in conjunction with grid 30. **a**: All grids. **b**: Grid 30 and grid 30 in conjunction with 'VP'. **c**: Grid adopted from Liu and grid 15. **d**: Grid 60 and grid 90.

Table 4.5: Area averaged heat transfer coefficient and total computation time for different grids

Grid	HTC $[W/m^2K]$	Total Real Time Until Convergence [hr]
30	690.7959	8.01
VP	691.2725	10.11
Liu	688.1077	7.94
15	697.2385	Not converged in 24 hr
60	693.7577	6.54
90	693.6331	7.54

All wall normal grind independence cases are depicted in the top left (a) plot of Figure 4.5. The liquid film thickness of all cases except the case for 15 grid layers show a great similarity. To get a better picture of the difference between the separate cases, plots b, c and d depict the cases in pairs. In terms of mean film thickness the grid was found independent for 30 grid layers and more. Also, the different grid configuration of Liu or the fully developed inlet velocity profile did not influence the mean film thickness. However, some wiggles that are not observed at the 30 layer grid can be observed in the case of Liu, 60 and 90 layers. The film Reynolds number for each case was found to be far below the transition Reynolds number. Therefore there has to be some other explanation for the wiggles. One possible explanation is the effect of *numerical diffusion* (see 2.4.1) .

Random numerical noise might disturb the liquid film, causing wave formation. Beside, the velocity difference between the film surface velocity and the vapor velocity results in a shear stress on the liquid film. Shear stress on the liquid film surface is known to induce surface wave formation. Numerical diffusion acts as an extra viscosity and therefore dampens the waves. Numerical diffusion can be mitigated by means of grid refinement. For this reason mesh 60 and 90 do show surface waves when compared to mesh 30. In addition to this argument, mesh 90 shows even more wiggles than mesh 60. However, mesh 30 is more dense in the film region compared to the original mesh by Liu, so why does the mesh by Liu show wiggles and the more dense mesh not? The Modified HRIC scheme employed in the presented simulations is a scheme which, depending on the flow variables, switches between downwind differencing and multiple orders of the upwind schemes (see A.2). The upwind schemes are known to produce better solutions when employed on a uniform grid. The curve of grid cell size versus cell number (Figure 4.4) shows the highest gradient for mesh '30'. Thus a higher numerical viscosity can be expected in the '30' mesh, which ultimately results in the highest damping of the surface waves.

The geometric reconstruction scheme avoids problems of numerical diffusion by determining the volume face fluxes a geometric approach (see section A.1). Figure 4.6 shows the liquid film thickness on mesh '30' for HRIC and Geo-Reconstruct. As can be seen from Figure 4.6, the amplitude of the

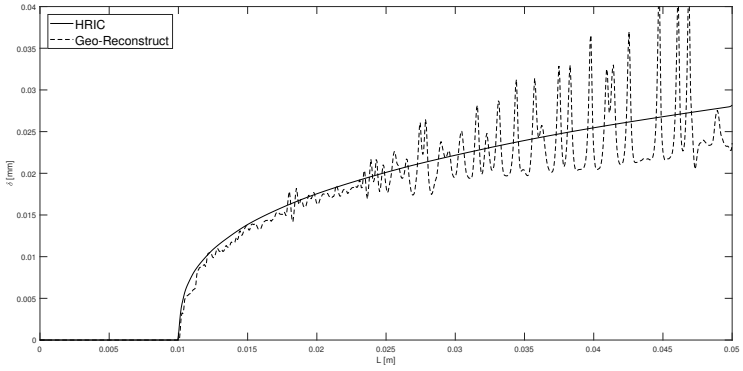

Figure 4.6: Liquid film yielded by HRIC and Geo-Reconstruct scheme on mesh 30.

surface waves yielded by the Geo-Reconstruct scheme are less damped, meaning that the assumption of the presence of numerical diffusion in the HRIC scheme is valid.

4.2.7. Validation

The model is checked by comparing three cases to results obtained from Liu et al[10]. Figure 4.7

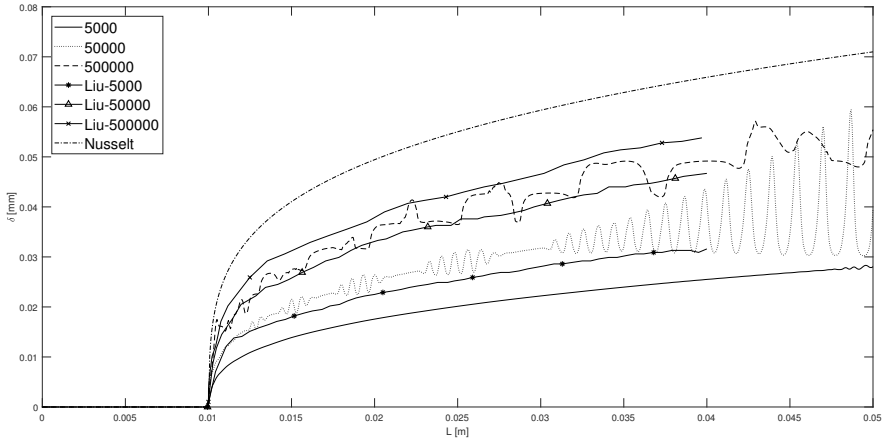

Figure 4.7: Comparison of liquid film thickness results by Liu[10] to simulation results for $r = 5000s^{-1}, \Delta t = 5 \cdot 10^{-5}$, $r = 50000s^{-1}, \Delta t = 5 \cdot 10^{-6}$, $r = 500000s^{-1}, \Delta t = 5 \cdot 10^{-7}$.

shows the liquid film thickness yielded by increasing values of the condensation coefficient r. As can be seen, there exists quite a deviation between the simulation results and the results by Liu. Moreover, the simulation results show sinusoidal waves for $r = 50000s^{-1}$ and even roll waves for $r = 500000s^{-1}$. It is hard to think of reasons explaining the discrepancies, since the exact simulation conditions were used as well as the same geometry and models. In addition, the mesh was found to yield grid independent results.

The only difference to the model of Liu, is the use of the modified HRIC scheme instead of the Geo-Reconstruct scheme. But, as pointed out earlier (4.2.6), both schemes yield the same mean liquid film thickness in the domain size employed.

Although both simulations make use of water as working fluid, a different approach to temperature dependency of the water may explain the deviating liquid film thickness. As we will see later, the thermal conductivity plays a major part in the development of the liquid film. A higher liquid conductivity may result in more mass transfer and ultimately a thicker liquid film. Another possible explanation is a different approach to the definition of the latent heat. As the latent heat was not mentioned by the authors, a smaller latent heat could result in a thicker liquid film. In order to tackle these problems, the authors were contacted to supply the properties they used, but without success.

Nevertheless, the simulations are still usable to test CPU performance per model. However, mimicking a relatively simple case of 2D laminar condensation flow already proves to be a challenge, indicating that modeling condensation is extremely prone to errors.

4.3. CPU test results

4.3.1. Test cases

The only phase-change model that is provided by Fluent in the one-fluid approach of the VOF method is the famous Lee model. As mentioned before, the condensation coefficient r determines not only the accuracy of the solution but also the stability and subsequently the real time until convergence. In order for any model to be workable, the real simulation time versus the accuracy of the model must be reasonable. Since ”reasonable” is rather subjective, the aim of this section is to show the extra real time needed for a certain increase in accuracy. In addition to the classical Lee model, two modifications of the Lee model, the modification by Liu[10] and the modification by Shen [6], will be tested. It will be interesting to see if the claimed improvement in accuracy will be at the expense of simulation time, or if it might even reduce the computation time.

In the end a total of five different models were tested. Using three different values of the condensation coefficient yields the fifteen test cases shown in table 4.6. To keep the solutions stable, the time step size was reduced in parallel with an increase in condensation coefficient. The necessity of time

step size reduction agrees with the findings of section 3.3.3. All cases were tested on a cluster of 16 nodes while using 1.5 GB RAM.

Table 4.6: Assessed cases in CPU performance test

Case	Model	Condensation Coefficient	Enhancement Factor	Δt
1.1	Lee	$5000s^{-1}$	-	$5 \cdot 10^{-5}s$
1.2	Lee	$50000s^{-1}$	-	$5 \cdot 10^{-6}s$
1.3	Lee	$500000s^{-1}$	-	$5 \cdot 10^{-7}s$
2.1	Liu	$5000s^{-1}$	-	$5 \cdot 10^{-5}s$
2.2	Liu	$50000s^{-1}$	-	$5 \cdot 10^{-6}s$
2.3	Liu	$500000s^{-1}$	-	$5 \cdot 10^{-7}s$
3.1	Shen	$5000s^{-1}$	10	$5 \cdot 10^{-5}s$
3.2	Shen	$50000s^{-1}$	10	$5 \cdot 10^{-6}s$
3.3	Shen	$500000s^{-1}$	10	$5 \cdot 10^{-7}s$
4.1	Shen	$5000s^{-1}$	28.25	$5 \cdot 10^{-5}s$
4.2	Shen	$50000s^{-1}$	28.25	$5 \cdot 10^{-6}s$
4.3	Shen	$500000s^{-1}$	28.25	$5 \cdot 10^{-7}s$
5.1	Shen	$5000s^{-1}$	100	$5 \cdot 10^{-5}s$
5.2	Shen	$50000s^{-1}$	100	$5 \cdot 10^{-6}s$
5.3	Shen	$500000s^{-1}$	100	$5 \cdot 10^{-7}s$

4.3.2. Results

Figure 4.8 shows the accuracy versus the total simulation time in hours of the fifteen tested cases. Cases 1.3, case 2.2 and case 2.3 were found to be converged visually. However, these cases did not satisfy the convergence condition stated in section 4.2.5.

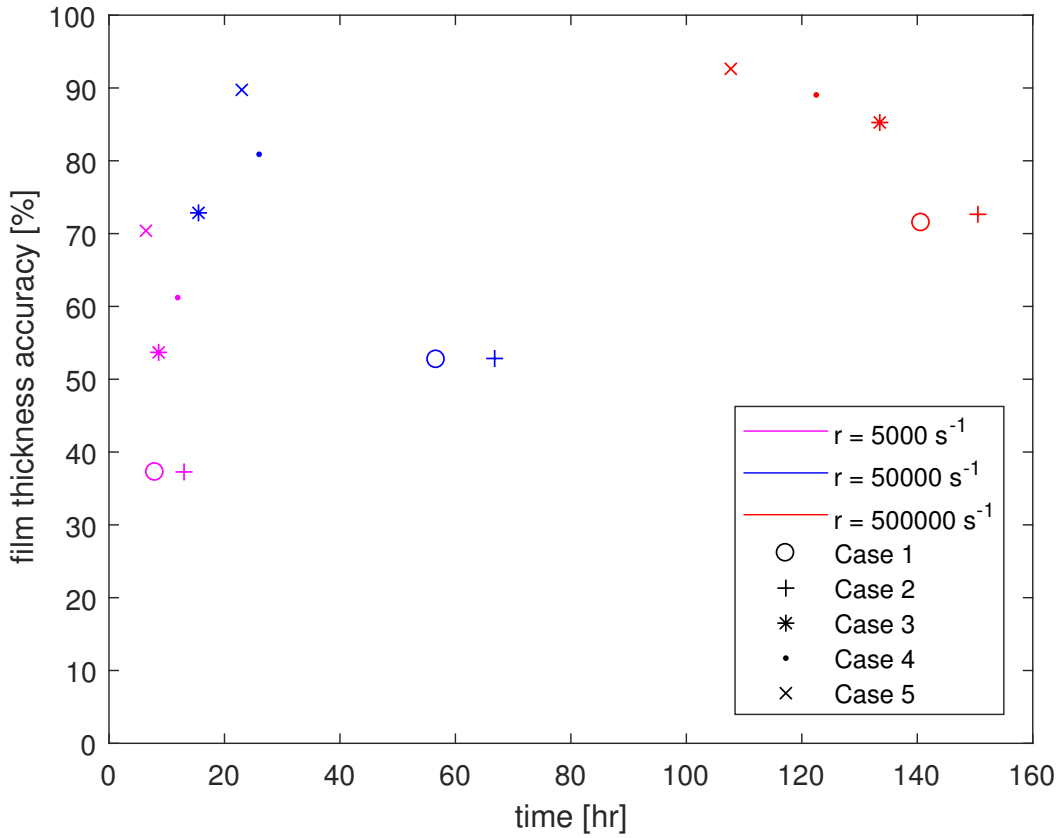

Figure 4.8: Performance of different condensation models checked in terms of liquid film thickness accuracy vs real computation time. Case 1: Lee model, Case 2: Liu model, Case 3: Shen model, $n = 10$, Case 4: Shen model, $n = 28.25$, Case 5: Shen model, $n = 100$.

Regarding the condensation coefficient r, several conclusions can be drawn from Figure 4.8:

1. The film thickness accuracy is improved by increasing r.
2. The real computation time increases significantly when increasing r from $50000s^{-1}$ to $500000s^{-1}$, while only a small increase in accuracy is obtained (5-10 % compared to 20 – 25 % in previous step).
3. For the Lee model and the Liu model, the increase in film thickness accuracy compared to the increase in computation time is linear.
4. For the Shen model, the increase in film thickness accuracy compared to the increase in computation time seems exponential.

Conclusion 1 is already widely discussed in literature and in section 3.3.3. However, conclusion 2, 3 and 4 are new and very interesting. Namely, these results imply that there *is* some threshold where increasing the condensation coefficient leads to a negligible increase in film thickness accuracy compared to computational effort. In terms of model practicality this is an extremely important conclusion. Although the threshold might deviate for different cases, this result indicates that for every particular case a careful consideration of the accuracy versus the computational effort should be taken into account. Especially when using the Lee model or a modification of the Lee model for design purposes, an analysis of the accuracy versus computation time might prove to be very fruitful.

Regarding the model performance in terms of accuracy the following statements in relation to the original Lee model (Case 1) can be made using Figure 4.8.

1. The modification by Liu (Case 2) yields a negligible increase in accuracy while the real computation time is increased.

2. Enhancement of the thermal conductivity in the two-phase region results in a higher liquid film accuracy.

3. Enhancement of the thermal conductivity reduces the real computation time for $r = 50000s^{-1}, r = 500000s^{-1}$.

Liu model

Looking at conclusion 1 gives rise to the question why the Liu modification yields more or less the same results as the classical Lee model. When the solution reaches steady state, a mass balance is set between the mass transfer between the phases, and the liquid mass leaving the domain. Taking a closer look to the mass flow per unit volume of both cases, the mass balance has set itself equally. The mean vapor volume fraction, considering the entire two-phase region, is in case of the Liu model slightly higher than that of the Lee model. But the integral of the mass transfer intensity, $\dot{m}_{vl}$, is equal. This means that the mass transfer between the phases is equal for both models, while the vapor volume fractions in the numerical interface (the two-phase region) deviate slightly. Now, remembering that the only difference between the models lies in the incorporation of the volume fraction in the mass transfer equation, and taking into account that mean temperature in the two-phase region is equal for both models, it is no surprise that the mean vapor fractions deviate. Since only by doing so, the same balance can be reached. The higher vapor fraction in case of the Liu model is a direct consequence of the incorporation of the $\alpha^{2/3}$ term compared to the α term in case of the Lee model. Because only when the vapor volume fraction in the interface is higher for the Liu model compare to the Lee model, the yield of both models is equal. This is pictured in Figure 4.9, where the mass transfer intensity of a fictional process is plotted versus the vapor fraction.

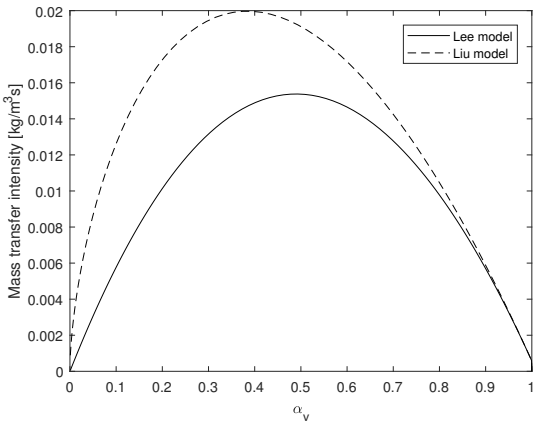

Figure 4.9: Comparison of mass transfer intensity versus the vapor fraction for the Lee model and Liu model.

Although we know that the models set their selves into the same mass balance, we do not know exactly why. It seems that the extra mass transfer due to the way the vapor fraction is incorporated is negligible. Only by increasing the mass transfer intensity constant r, the mass balance between the interface mass flow and the outlet mass flow can be changed significantly.

The increase in computational effort is difficult to explain. One explanation can be that the way the UDF-subroutine is incorporated into the software slows the program. Another perspective is that the deviation of the mass transfer intensity curve depicted in Figure 4.9, destabilizes the solution, causing an increase in iterations per time step. In any case, the increase in accuracy is negligible while the increase in computation time is significant. Therefore, the modification by Liu is deemed purposeless. In the paper by Liu, no comparison between his model and the classical Lee model is presented. The sole motivation behind the model is that it produces 'more physical results'. However, no further elaboration on this statement is given.

Shen model

Taking a look at the temperature profiles in the liquid film, depicted in Figure 4.10, reveals that enhancing the thermal conductivity in the two-phase region results in a steeper temperature curve in

the liquid region. This is also shown in the original work by Shen[6]. For this reason, the temperature difference between the wall and the interface increases. In parallel, the heat transfer increases. The more energy that is extracted from the vapor, the more vapor will eventually convert to liquid, meaning that enhancing the heat transfer enables phase change. Therefore, enhancing the heat transfer between the phases indirectly enhances the mass transfer between the phases. In the end, since the energy equilibrium is set at a higher rate, the mass transfer equilibrium is also set at a higher rate. The result is a thicker liquid film.

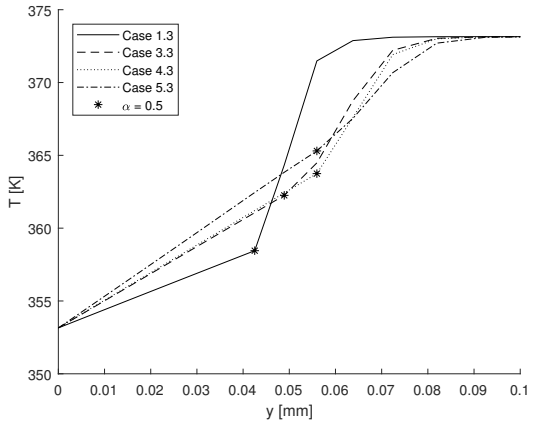

Figure 4.10: Temperature profiles for the Lee model (case 1.3) and the Shen model with ascending increasing enhancement of the thermal conductivity (case 3.3, 4.3, 5.3) for $r = 500000\ s^{-1}$ at $x = 0.04m$. The star indicates the interface position.

The temperature profile in the Nusselt solution goes linearly from the wall temperature to the saturation temperature [9] (see Figure 4.1**b**). Taking this linearity into account, enhancing the thermal conductivity brings the temperature profile closer to the Nusselt solution. Even enhancing the thermal conductivity beyond the highest physical conductivity present (in this case the water-liquid conductivity) yields a more physical solution. Additionally, taking note that a two-phase region representing an interface is actually a non-physical approximation, the enhancement of the conductivity in this region proves to be a better model, then volume averaging the thermal conductivity.

4.4. Conclusion & Recommendations

In this chapter the real computational cost versus the obtained accuracy was revealed. By doing so the practicality of the computational models was exposed. As practicality is rather subjective, this study is only indicative. Nevertheless, since no explicit statements about computational effort were made in literature, this study gives new insights.

In addition, this study showed that the increase in computational effort versus the increase in accuracy is not necessarily linear. Meaning that depending on the model, one should always consider if the increase in accuracy is worth the wait. Especially when one wants to use the models for design purposes, and many different configurations are tested, taking the computational effort into account is advisable.

Next, the Shen models (case 3, case 4, case 5) outperformed the Lee and Liu model in terms of accuracy and computational effort. The Liu model was even found to be completely irrelevant. Because the Shen model's accuracy seems to increase exponentially, while the Lee model's accuracy increases linearly, the Shen model seems to be an improvement. Moreover, the temperature profile of the Shen model comes closer to the Nusselt solution.

The exponential increase of the Shen model is very interesting, but this conclusion is only founded on nine test cases. Therefore, in future work this implication needs to be validated by conducting more tests at more different condensation frequency (r) levels.

Next, only three condensation models were tested. Thereby, all condensation models were related to the original Lee model. The performance of heat flux balance models and other condensation models that were discussed in chapter 3 is still unknown. In this work, an attempt was made to investigate the performance of the Tanasawa model and the heat flux balance model by Sun. However, due

to implementation problems of the smearing function by Hardt & Wondra [75], the attempts were suspended. Nevertheless, the accuracy versus CPU-effort performance of these models has to be known before one could say what condensation model is deemed most practical. Therefore, in future work the implementation difficulties have to be sorted out, after which the same sort of study needs to be conducted on these models.

Finally, the performance of the models was only tested on CPUs. Recent literature have showed promising results for CFD simulation acceleration for turbomachinery design on GPUs [87] (Graphics Programming Unit). Therefore, quantifying the GPU-effort for condensation simulations will be very interesting.

5

Condensation model performance in 'complicated' flows

5.1. Introduction

Flow features such as circulation and separation are of high importance in heat transfer applications. Due to these flow phenomena, heat transfer is enhanced. Therefore, most plate heat exchangers consist of a geometry that is designed to induce separation and circulation. This chapter aims to assess available phase change model's performance when more 'complicated' flow regimes as circulation, surface wave formation and separation are induced.

Objectives

- Provide an insight in the applicability of the phase change model(s) to more complex flow phenomena.
- Expose difficulties in applying phase change models in more complex flows.

Geometry

- Flat geometry to assess surface wave formation and evolution
- Flat plate geometry to assess surface wave formation and evolution on films while being exposed to artificial perturbations
- Corrugated channel to assess the effect of the corrugations on wave formation and heat transfer of condensate flow

Restrictions

- The phase change models must be implementable in Fluent 18.1.
- The phase change models can be employed in a finite volume VOF interface tracking environment.

Comparison

First the wave formation and evolution of a condensate flow on a flat plate will be modeled and checked with literature. Also the effect of the waves on heat transfer will be checked and compared with literature. Subsequently, the film flow without condensation will be compared to the condensate flow. By doing so, differences between the two flows will be exposed. In addition, an artificially disturbed film flow will be compared to an artificially disturbed condensate flow. The same discrepancies as in the previous set-up are expected to be found. In this way, the influence of the phase change model on the flow field is thoroughly assessed.

The next stage is to assess the heat transfer predictions of the phase change models in case of a corrugated channel. First a film flow over a corrugated surface is validated with literature. Following, the phase change models are turned on. This will be done in both the laminar and the wavy laminar regime. The aim is to find out if the phase change model's heat transfer predictions will adhere to theory presented in section 5.2.1.

5.2. Film flow and condensation flow in literature

5.2.1. The wavy laminar flow regime

In general, there exist three flow regimes for film flow. The laminar flow regime, the wavy laminar regime and the turbulent regime. Each flow regime can be identified by its film Reynolds number. The film Reynolds number is governed by the bulk velocity U_b and the hydraulic diameter D_h of the film, hence:

$$U_b = \frac{\Gamma}{\rho_l \cdot \delta} \tag{5.1}$$

$$D_h = \frac{4A_c}{\mathcal{P}} = \frac{4 \cdot 1 \cdot \delta}{1} \tag{5.2}$$

$$Re_\delta = \frac{\rho_l U_b D_h}{\mu_l} = \frac{4\Gamma}{\mu_l} \tag{5.3}$$

The typical onset for the wavy laminar regime is around thirty ($Re_\delta \approx 30$). Transition to turbulent flow takes place at $Re_\delta \approx 1000$ in the outer region of the film. The liquid film will be fully turbulent when the Reynolds number of the inner region reaches $Re_\delta \approx 1800$. When condensation occurs, the film temperature is typically closer to the saturation temperature. According to Mills [31], the temperature dependent transition (to turbulent) Reynolds number can be found using the following relation:

$$Re_{tr} = 5800 Pr_l^{-1.06} \tag{5.4}$$

Between the laminar regime and the fully turbulent regime, some extra wave phenomena can be distinguished. Increasing the Reynolds number in the range of $20 < Re_\delta < 200$ causes the formation of the first small surface waves and is referred to as the capillary wavy laminar regime [88]. Surface tension forces play an important role in this regime. The surface tension forces are caused by the local temperature and concentration differences and start being of significance when they equal the viscous and inertial forces. As surface tension acts to minimize the film surface the waves occur as high frequency, low amplitude waves, so-called ripples.

With increasing Reynolds number, the wave amplitude (crests and troughs) increases and the frequency decreases. The shape of the waves is almost periodic sinusoidal. Therefore, the waves are often referred to as sinusoidal waves.

As the Reynolds number increases further, the inertial forces start to dominate the surface tension forces and the wave lengths increase while the wave frequencies decrease. Subsequently, the previous sinusoidal waves turn into so-called roll waves. The corresponding flow regime is referred to as the inertial wavy laminar regime ($200 < Re_\delta < 1000$). From experiments it was found that roll waves travel with an almost constant celerity. The celerity of a wave represents the magnitude of the wave velocity, also called the phase speed. Typically, in front of a roll wave, there exists a local minimum in film thickness. In the local minimum in front of the large wave, the surface tension forces dominate the inertial forces, causing the formation of ripples. The multiple wave shapes that exist in wavy laminar condensate flow are depicted in Figure 5.1.

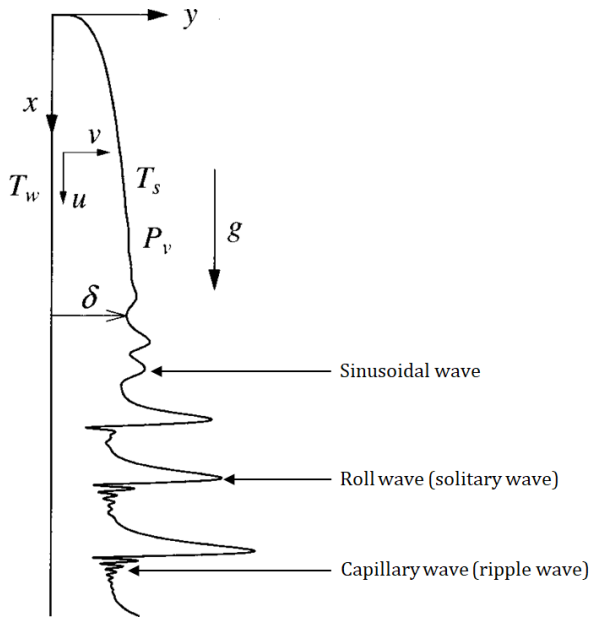

Figure 5.1: Schematic representation of wave formation during condensation in wavy laminar flow regime. Figure taken and modified from [11]

In the fully laminar flow regime the heat transfer is entirely governed by the liquid film resistance according to:

$$h = \frac{k_l}{\delta} \tag{5.5}$$

However, the analysis of the heat transfer in the wavy laminar regime is less straightforward. Due to the complexity of the wave formation caused by surface tension and gravity, no theoretical approach is available. Predictions in heat transfer are made by developing correlations using experimental data. But by using correlations, no insight in the heat transfer driving forces is given. Where in fully laminar flow, heat transfer is entirely governed by conduction, in wavy laminar flow also convection will play a part. For instance, Stühltrager [89] [90] found that the temperature profile in the liquid film is affected by convection. But, the enhancement of heat transfer in the wavy laminar regime is mainly attributed to local thinning of the liquid film, meaning that conduction is still the dominant heat transfer mechanism. Jayanti & Hewitt [91] have also investigated the influence of sinusoidal waves and solitary waves on the heat transfer performance. They point out that although the sinusoidal waves enhance heat transfer, the heat transfer is still governed by the liquid film thickness. Also, the effect of circulation on heat transfer in large solitary waves is investigated. It is concluded that due to the higher cross-sectional area under solitary wave compared to the cross-sectional area under the substrate film, the mean velocity and circulation velocity are relatively small in the wave. Subsequently, the contribution to heat transfer by convection is concluded to be small. Continuing the work of Stühltrager, Miyara (1999) [92] investigated the heat transfer in roll waves with a Reynolds number of one hundred. He finds that for low Prandtl numbers (0.1 & 1) heat transfer is determined by conduction, while for high Prandtl numbers (10 & 100) both conduction and convection govern heat transfer.

5.2.2. Wavy laminar condensate flow

One can imagine that the heat and mass transfer caused by condensation may result in a different wave behavior compared to falling film behavior. In order to find these differences, Stühltrager[89] compared numerical condensate flow results with experimental falling film results. In his paper, the evolution of a condensate film was modeled using a finite difference approach. After the liquid film was converged, every $1/16s$ a snapshot was taken. From this analysis several conclusions were drawn:

1. The celerity of the modeled ripples is smaller than the celerity obtained from experiments. Therefore, the conclusion is drawn that condensation slows the waves down.

2. While ripples grow into larger sinusoidal waves between $70 < Re_\delta < 140$, the film thickness is decreasing. In addition, the wave celerity is strongly increasing.

3. The condensation flow is in good agreement with the experiments for falling film flow for $110 < Re_\delta < 220$.

4. For $Re_\delta > 220$ the wave amplitude is almost not increasing anymore, the film thickness starts to increase again. In addition waves start to merge. Since the Nusselt solution does not take surface waves into account, the Nusselt film thickness is much higher in this region than the simulated one.

The main difference between the numerical method employed by Stühltrager compared to the use of Fluent, is the use of a prescribed solution for the liquid film thickness by Stülhtrager. In other words, in the approach of Stühltrager, the liquid film thickness is determined from the Nusselt solution, whereas in Fluent the liquid film thickness is estimated using a mechanistic model with a physical base (the Lee model). Therefore, Fluent's method is applicable to other problems, whereas Stühltrager's method is only applicable to the Nusselt condensation problem. Now, considering the differences in the numerical approach, it would be interesting to see if the Lee model and descendants of the Lee model are able to reproduce the aforementioned conclusions from Stühltrager.

5.3. Condensation flow on a vertical flat plate - wave analysis

5.3.1. Set-up

The classical Lee model in Fluent will be tested by simulating the condensate flow reported by Stühltrager [89]. In addition, the modification of the Lee model by Shen [6] will be tested in the same way. The condensation coefficient is set at $r = 50000 s^{-1}$ in both cases. In this way a trade-of between the real computation time, and the film thickness accuracy is made (see 4.3.2). The enhancement factor in the modification by Shen is chosen so that the thermal conductivity in the two-phase region takes the liquid phase conductivity. By doing so, the conductivity is maximized without obtaining a non-physical total conductivity. The working fluid used by Stühltrager is the refrigerant trichloromonofluoromethane or better known as R11. Table 5.1 shows a summary of the test cases. A vapor flow inlet condition is applied at the inflow boundary in order to supply vapor mass for the

Table 5.1: Condensation flow waviness test cases

Working Fluid	Kinematic Viscosity $[m^2/s]$	Condensation Model	Condensation Coefficient $[s^{-1}]$	$T_{sat} - T_w [K]$
R11	$3.17 \cdot 10^{-7}$	Lee	50000	12.27
R11	$3.17 \cdot 10^{-7}$	Lee modified by Shen	50000	12.27

condensation process. In Stühltrager [89] the vapor was modelled as quiescent. However, Phan & Narain [93] showed that the influence of the vapor flow on the wave behaviour of the condensate film is negligible. They also showed that the effect of surface tension on roll waves is negligible. Namely, the waves are gravity driven and the surface tension only slightly assists in steepening the front of the waves. This is in agreement with Miyara (2000) [94], where it is concluded only the wave peak height of the roll waves is influenced by surface tension while the celerity of the roll waves is independent of surface tension. Moreover, Stühltrager ignored surface tension altogether, therefore surface tension is not taken into account.

The grid employed by Stühltrager is not mesh independent, but it captures at least 1/4 of the smallest measured amplitude of the most unstable wave. In addition, the most unstable wave length resolution is chosen at 8 points. (So at least 4 grid cells are used to capture the smallest amplitude while at least 8 grid cells are used to capture the smallest wave length.) The mesh resolution from Stühltrager is adopted in this work in order to assess if Ansys Fluent, and the phase change models, are able to reproduce the reported results. The solution was considered converged when the liquid volume, the area averaged heat transfer coefficient and the area averaged velocity became constant. The time step was chosen as $5 \cdot 10^{-6}\ s$, so that the solution remained stable. The resulting global Courant number was 0.04.

All presented parameters are non-dimensionalized using the theoretical Nusselt film thickness δ_{max} at the *outflow* boundary according to Equation 5.6.

$$x^* = \frac{x}{\delta_{max}} \quad \delta^* = \frac{\delta}{\delta_{max}} \quad u^* = \frac{u}{u_{max}} \quad t^* = \frac{t}{\delta_{max}/u_{max}} \tag{5.6}$$

The temperature is non-dimensionalized using the saturation temperature T_{sat} and the wall temperature T_w according to:

$$T^* = \frac{T - T_w}{T_{sat} - T_w} \tag{5.7}$$

5.3.2. Validation

Wave speed at line of inception

The first definition that needs to be considered is the so-called *line of inception*. This line represents the onset of waviness and normally coincides with $Re_\delta \approx 30$. But what is waviness? Stainthorp & Allen [95] define the line of inception as the point where the wave amplitude exceeds 10^{-3} mm. However, it should be noted that this condition is only defined by the instruments used to detect the waviness. Waves may occur somewhat earlier, but are difficult to discern. In any case, since Stühltrager compares his work to the work of Stainthorp & Allen, their definition is adopted in this work and is also referred to as the line of inception.

In Stainthorp & Allen a correlation between the wave speed at the line of inception and the local film Reynolds number is presented, see Equation 5.8:

$$K = 2.95 \cdot Re^{0.5} \tag{5.8}$$

One should note that the wave speed K is determined in centimeter per second. In order to check the first conclusion by Stühltrager, "the celerity of the modeled ripples is smaller than the celerity of experiments", the wave speed of the first wave at the line of inception will be taken at six different times, with a time interval of $1/16\ s$. Subsequently, the average of the six wave speeds is taken. To be complete, the numerical model will be checked by the simulation of three film flows without condensation. By doing so, the difference in wave speed at inception point between condensation and no condensation will be assessed.

Wave disturbance analysis

Due to the relative old age of the literature presented by Stühltrager and Stainthorp & Allen, also a simple wave disturbance analysis is conducted. Nosoko [96] developed correlations to describe the wave speed of falling liquid films which are excited by a disturbance frequency. By testing a wide range of flow ranges and temperatures of water the correlation was validated in the range:

$$15 < Re_0 < 90 \tag{5.9}$$

One should care to note that the Reynolds number used by Nosoko is defined in a different way than used throughout this work:

$$Re_0 = \frac{u_0 \delta_0}{\nu} \tag{5.10}$$

where u_0 represents the velocity at the surface of the film at δ_0. In addition, the following dimensionless numbers are defined:

$$We_0 = \rho \delta_0 u_0^2 / \sigma \tag{5.11}$$

$$u_w' = u_w / u_0 \tag{5.12}$$

$$f' = f \delta_0 / u_0 \tag{5.13}$$

where We_0 is the Weber number, u_w' the dimensionless wave speed and f' the dimensionless disturbance frequency. Now, the dimensionless wave speed can be determined using correlation 5.14.

$$u_w' = 1.49 f'^{-0.449} We_0^{0.087} Re_0^{-0.425} \tag{5.14}$$

The disturbance of the wave is introduced using an alternating velocity according to the relation by Kungi[97].

$$U = [1 + \epsilon sin(2\pi f t)]U_b \tag{5.15}$$

where ϵ is a parameter set to 0.03 by Miyara (2000) [94]. U_b represents the bulk velocity of the film without waves and t represents the flow time. Also the time t' is non-dimensionalized using the bulk velocity according to:

$$t' = t/(\delta_0/U_b) \tag{5.16}$$

5.3.3. Results

Qualitative comparison with Stühltrager

The liquid film thickness yielded by the classical Lee model and the modification of the Lee model by Shen are shown in Figure 5.2 and Figure 5.3, respectively. Also the wave speed at time t^* is shown for the waves starting at the line of inception. In addition, the theoretical Reynolds numbers are shown at the right hand side of each figure.

Both films exhibit the same behavior in the sense that small ripples start to grow from the line of inception. The ripples become larger and sinusoidal waves are formed. Eventually, the sinusoidal waves grow into large solitary waves. This observation agrees to the observation of Stühltrager [89]. However, Stühltrager also notes that the solitary waves are merging downstream into harmonic waves. As can be seen from the dotted line in both Figure 5.2 and Figure 5.3, the wave speed is increasing from the line of inception and is still increasing when the end of the domain is reached. Also the wave amplitude is increasing slightly, like reported by Stühltrager. However, due to the underpredicted film thickness, the film Reynolds number does not exceed $Re_\delta = 70$ for both cases. Stühltrager reports that the wave amplitude stops increasing at $Re_\delta > 220$. At the same moment the wave celerity does not increase anymore, and subsequently, the film thickness increases again and waves start to merge. Hence, the wave merging flow regime is not reached in both cases.

By analyzing the position of the line of inception at six different times for each case, it is validated that, like in the results of Stühltrager, the line of inception is not fixed but moves up an down the domain. Also, the same observation as reported by Stühltrager is made that the surface instability starts with ripple waves. Next, as the ripples swiftly grow into sinusoidal waves, the film thickness decreases and the wave celerity strongly increases, like reported by Stühltrager.

In summary, the overall wave evolution of both cases agrees to the findings by Stühltrager. This means that in both cases the numerical model is able to predict the flow phenomena in a correct manner. However, one should note that evolution of waves depends on both the condensation model and the multiphase model. In order to be able to say something about the condensation models, conclusion 1 (see section 5.2.2) will be comprehensively assessed.

In addition, the paper by Stühltrager is rather old, and therefore, the results should be compared with more up to date literature.

Qualitative comparison with other literature

In Miyara (2001) [11], a wavy condensate film without an artificial perturbation and a wavy condensate film with an applied artificial perturbation are modeled. In the first case, the surface waves develop from the spatial perturbations caused by the variations between the initial condition and the numerical solution [11]. The perturbations grow into irregular large amplitude waves. As the solution proceeds, the line of inception moves downstream, until almost all waves are advected out of the domain.

When an artificial perturbation is applied, the line of inception fluctuates between $x^* = 250 - 300$. The fluctuation of the position of the inception line agrees with Stühltrager as well as with this work. However, the x-location is different. This might be attributed to the underprediction of the film thickness in this work. When the film thickness would adhere to the Nusselt film thickness, the film would grow more rapidly and subsequently the Reynolds number would be higher, causing the inception condition to be met. Miyara explicitly concludes that the location of wave inception depends on the Prandtl number. In this work and the work by Stühltrager, the fluid Prandtl number is 4.3, in the work by Miyara the Prandtl number is 5. Therefore, the difference in inception line position may also be attributed to this deviation in Prandtl number. It should be noted, however, that the line of inception is not explicitly

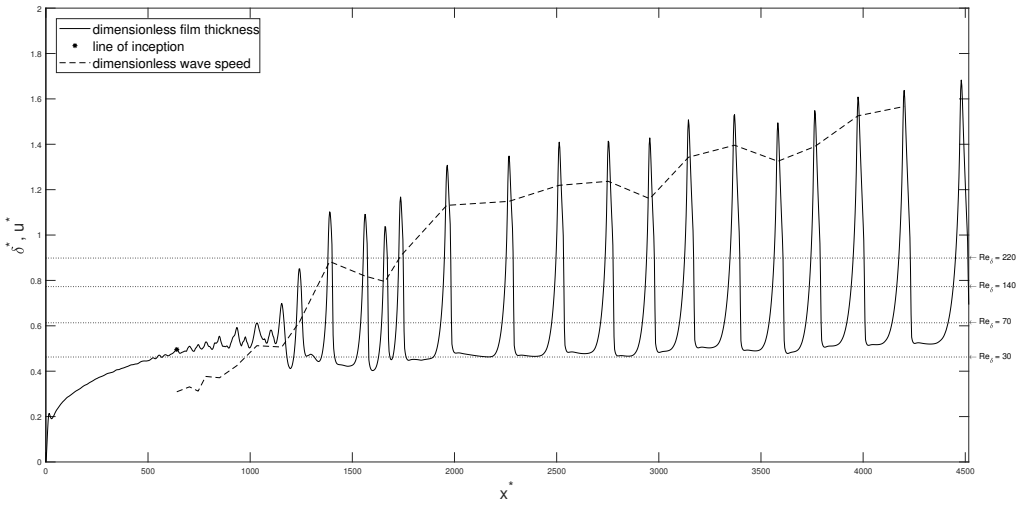

Figure 5.2: Dimensionless film thickness predicted by the classical Lee model at time $t^* = 9203$. Dimensionless wave speed from line of inception at same time index. From the line of inception at $x = 640$ (indicated by a star) small ripples grow into larger sinusoidal waves. At $x = 1200$ large solitary waves start to form and move down the domain.

defined in the work by Miyara, which also may lead to different results compared to Stühltrager and this work.

In any case, the surface waves of the present simulations seem to be caused by a continuing random numerical perturbation. Namely, the waves are continuously formed even when the solution has reached steady state (in terms of mean film thickness).

Miyara notes that the waves that develop on a perturbed condensate film are initially sinusoidal. Afterwards, they develop rapidly into pulse-like solitary waves, consisting of a large amplitude wave and small amplitude capillary waves. The results by Stühltrager show a similar behavior. However, no small capillary waves are observed. In this work, the capillary waves are only observed sporadically in the results produced by the Shen modified Lee model (see Figure 5.3). Miyara also notes that after the initial growth of the waves, the waves move downstream without interaction and maintaining their shape. This was also seen in this work. The absence of wave merger in this work and the work by Miyara can be attributed to the small Reynolds number. In this work, the domain is large enough for the film to reach the Reynolds number mentioned in conclusion 4 (see section 5.2.2). However, due to the underprediction of the film thickness, the Reynolds number is not reached. In the work by Miyara, the domain (with $x_{max} = 1250$) is too small to reach the Reynolds number from conclusion 4. Finally, Miyara notes that the sinusoidal wave region is very small compared to the solitary wave region. This agrees to both this work, and the work by Stühltrager.

Other authors that have investigated the wave behavior of falling condensate films are Aktershev and Alekseenko [98]. In this work the solitary waves are described as:"non-linear waves of high amplitude, which have a typical peak with steep front slope and low local maximum in front of it (the capillary ripples)." The ripples mentioned by Miyara and by Aktersev & Alekseenko are seen more often throughout literature. For instance, in Miyara[94], Gao[99] and Kungi[97]. In all papers surface tension is included. Also capillary waves are known to be due to the effect of surface tension forces dominating inertial forces (low Weber number). Since the local Weber number depends linearly on the film thickness, the surface tension forces start to dominate the inertial forces at the local minimum of the solitary wave. In both this work and the work by Stühltrager, surface tension is neglected. Therefore, the capillary waves are not present. However, this does not explain why in Figure 5.3 some capillary waves are observed.

The instantaneous dimensionless velocity field is depicted for the Lee model and Shen model in Figure 5.4**a** and Figure 5.5**a**, respectively. In addition, the local dimensionless temperature contours are shown. In **b**, **c** & **d**, the local temperature profiles at the wave rear, crest and in the substrate film are presented for both figures. The results for both the Lee model and Shen model are very similar. Therefore, first the Lee model (Figure 5.4) will be compared with literature. After, the differences

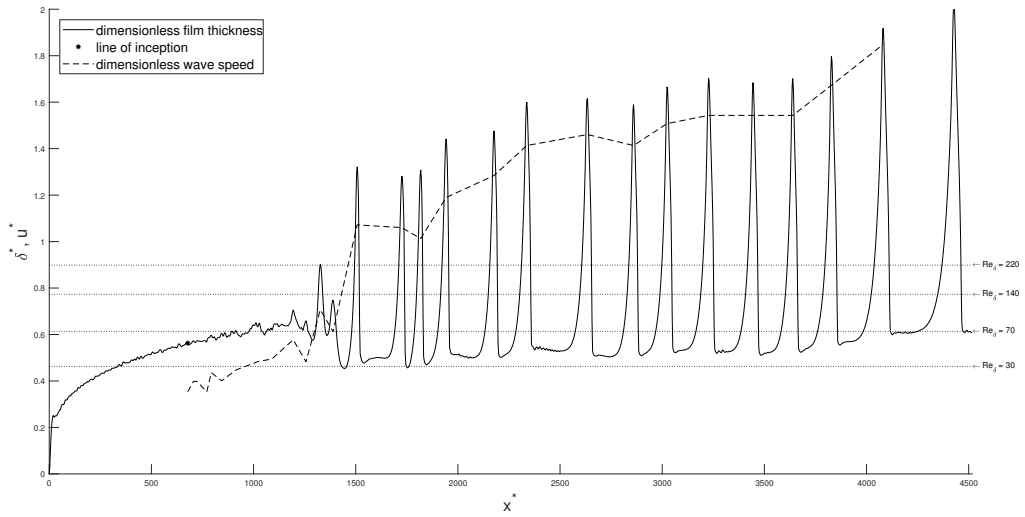

Figure 5.3: Dimensionless film thickness predicted by the by Shen modified Lee model at time $t^* = 5496$. Dimensionless wave speed from line of inception at same time index. From the line of inception at $x = 680$ (indicated by a star) small ripples grow into larger sinusoidal waves. At $x = 1200$ large solitary waves start to form and move down the domain.

between the Lee model and Shen model are assessed.

In the substrate region in Figure 5.4**a**, the velocity is zero at the wall and increases according to the Nusselt solution to it's local maximum at the interface. The wave slides with a considerable higher wave speed over the substrate layer, causing the substrate velocity to increase locally. For instance, the velocity under the crest already exceeds the maximum substrate velocity at $\delta^* \approx 0.2$. This is in accordance with findings by Stühltrager [90]. The main difference between the present velocity fields and the velocity field by Stühltrager is that the y-component of the velocity vector is almost invisible. But, taking a closer look at the velocity vector in the wave rear region ($3120 < x^* < 3140$) reveals that the vector is slightly pointing into the film, whereas in the wave front region ($3180 < x^* < 3200$) the vector is slightly pointing upwards. This is also seen in the vector plots by Stühltrager[90].

The temperature contours are deformed in a way that the peaks of the contour lines near the wall surface are upstream, compared to the peaks of the contour lines close to the film surface. This was also witnessed by Stühltrager. The local temperature profile at the wave rear (**b**) has a convex shape, the temperature profile in the crest (**c**) a concave shape, and the temperature profile at substrate (**d**) is linear. This is in accordance with the temperature profiles found by Stühltrager [90]. Both the convex shape and the concave shape indicate that heat transfer is not only determined by conduction, but also by convection. In the wave rear, convection decreases the heat transfer, whereas in the crest region heat transfer is enhanced. Compared to the results by Stühltrager, the liquid film surface does not reach the saturation temperature. This can be attributed to the underprediction of mass transfer by the condensation model. As was already seen in Figure 5.2 and Figure 5.3, the film thickness in case of the Shen model is slightly larger than the film thickness of the Lee model. In addition, the temperature profiles in Figure 5.5**b**, **c** & **d** are somewhat less steeper than the profiles produced by the Lee model (Figure 5.4). This means that the heat flux, with $q^* \sim \frac{\partial T^*}{\partial \delta^*}$, in case of the Shen model is higher compared to the heat flux of the Lee model. Since the energy transfer due to condensation is linearly dependent on the mass transfer, the higher heat flux is deemed logical.

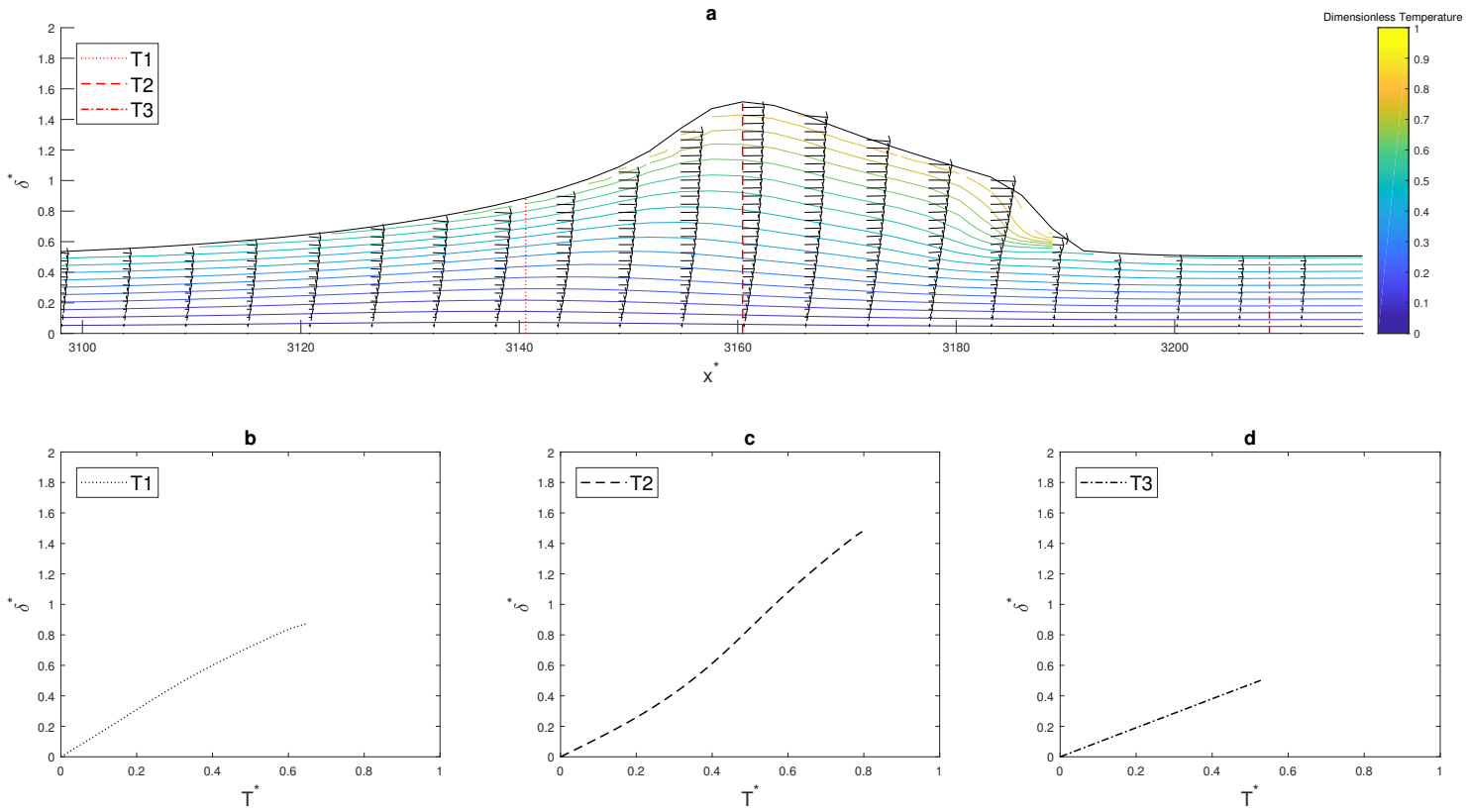

Figure 5.4: Instantaneous solitary wave yielded by Lee model from Figure 5.2 at $t^* = 9203$. **a**: Dimensionless velocity vector plot of solitary wave, instantaneous dimensionless temperature contours, T1, T2 & T3 refer to temperature profiles in b,c & d, respectively. **b**: Temperature profile at wave rear. **c**: Temperature profile at wave crest. **c**: Temperature profile in substrate film.

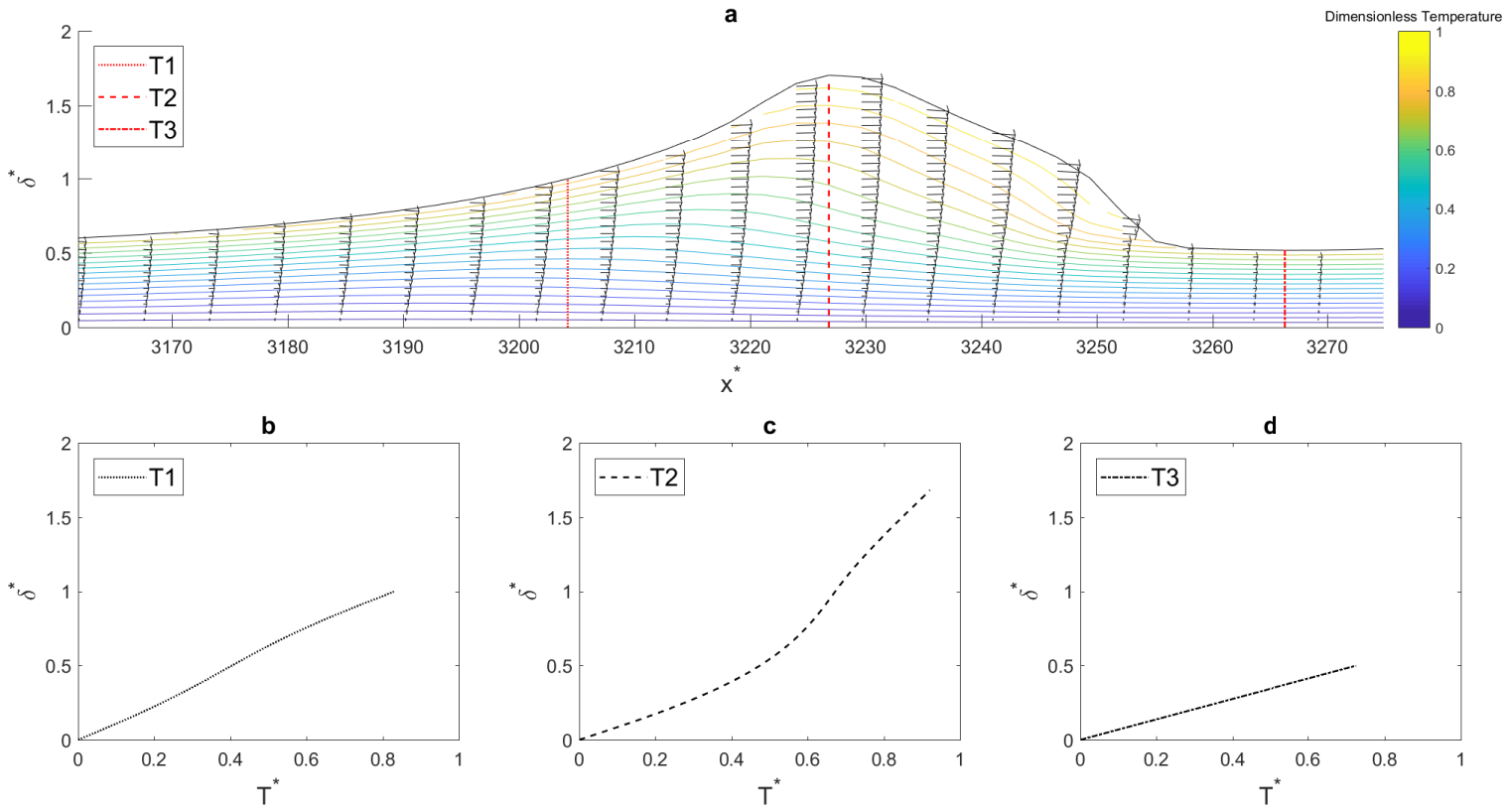

Figure 5.5: Instantaneous solitary wave yielded by Shen model from Figure 5.3 at $t^* = 5496$. **a**: Dimensionless velocity vector plot of solitary wave, instantaneous dimensionless temperature contours, T1, T2 & T3 refer to temperature profiles in b,c & d, respectively. **b**: Temperature profile at wave rear. **c**: Temperature profile at wave crest. **c**: Temperature profile in substrate film.

By subtracting the unsteady wave speed of the solitary wave from the velocity field, one can get an insight in the local unsteady flow mechanism. Gao [99] used this method to show that there exists a circulation zone in large solitary waves. In Figure 5.6 and Figure 5.7 the local velocity field subtracted with the instantaneous phase speed is depicted for the Lee model and Shen model respectively. Gao stated that perhaps the reason for the name ”roll wave” for large amplitude waves stems from the roll shape of a recirculation. In any case, both Figure 5.6 and Figure 5.7 show a developing circulation zone in the top-right region of the crest. The effect of the circulation is seen in the temperature contours of Figure 5.4 and Figure 5.5, where the contours become more dense under the circulation zone. This is also seen in the work of Miyara (2001) [11]. However, the circulation zone in Miyara is much more distinct than in this work. Subsequently also the temperature contours are much more deformed. In an earlier work by Miyara (2000)[94], it is pointed out that for increasing Reynolds number, the circulation zone also increases. This is also seen when Figure 5.4 and Figure 5.5 are compared. Namely, in case of the Shen model (Figure 5.5) the circulation zone is slightly bigger than in case of the Lee model. Figure 5.2 and Figure 5.3 shows that also the Reynolds number is larger in case of the Shen model, agreeing to the statement of Miyara. The extra heat transfer due to circulation is expressed in the somewhat more, compared to Figure 5.4, deformed and dense temperature contours shown Figure 5.5 .

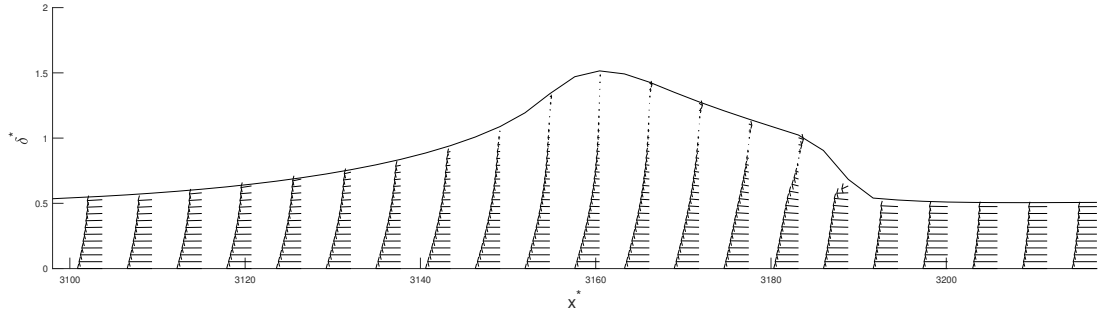

Figure 5.6: Instantaneous solitary wave yielded by Lee model from Figure 5.2 at $t^* = 9203$. Velocity vector plot at the wave-speed moving coordinates, with $K^* = \frac{K}{u_{max}} = 1.35$

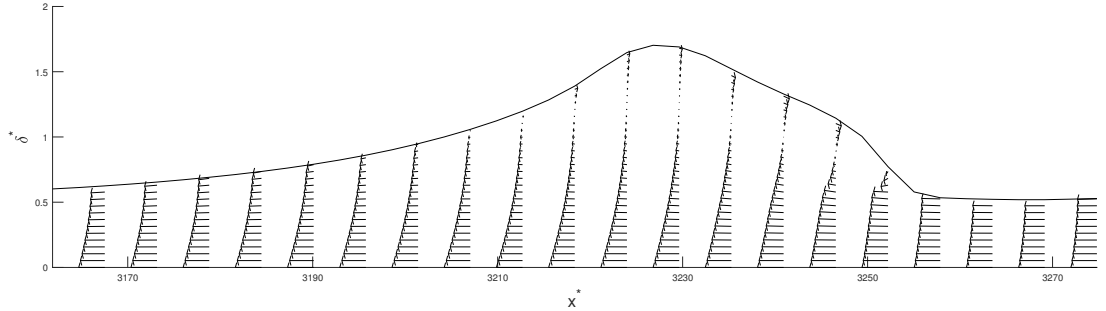

Figure 5.7: Instantaneous solitary wave yielded by Shen model from Figure 5.3 at $t^* = 5496$. Velocity vector plot at the wave-speed moving coordinates, with $K^* = \frac{K}{u_{max}} = 1.54$.

5.3.4. Line of inception

As mentioned before, the line of inception is the point where the wave amplitude exceeds a thousandth of a millimeter, and also represents the transition from the laminar flow regime to the wavy laminar flow regime. The transition Reynolds number normally lies around thirty [31] and will be taken as a reference point.

The transition Reynolds number lies in the region reported by Phan & Narain [93] for the classical Lee model. However, the transition Reynolds number for the Shen modified Lee model far exceeds the theoretical value of thirty, meaning that the model imposes some sort of dampening on the wave formation. Due to the enhanced conduction in the two-phase region, the temperature profile in the film will be different from the Shen model compared to the classical Lee model, as can be seen in Figure 5.8. Possibly, the smooth temperature profile of the Shen model causes the random instability to be expressed at higher Reynolds numbers. Yet, it is very hard to say something useful about an instability caused by the numerics. Therefore, this notion should only be seen as a possibility, not a fact. According to Phan & Narain [93], there exists a small influence of $\Delta T = T_{int} - T_w$ on the transition Reynolds number, where the subscript int indicates the interface. However, the question remains if this influence is large enough to cause the transition Reynolds number to differ with a magnitude of around twenty.

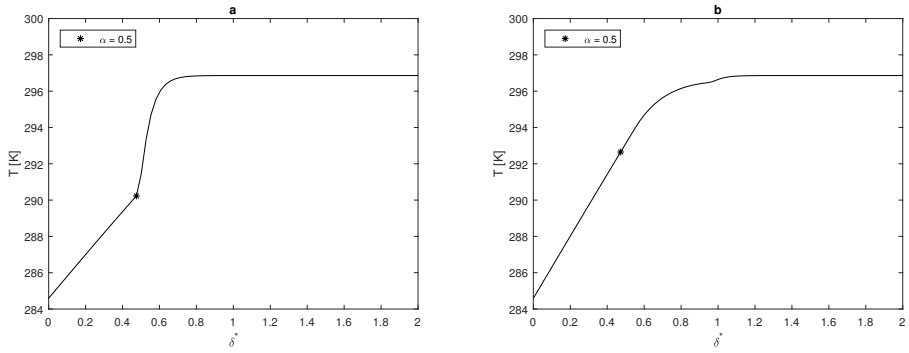

Figure 5.8: Temperature profile at $x^* = 641$ (wave inception location Lee model). The star indicates the interface position. **a**: Lee model, **b**: Shen model

5.3.5. Wave speed analysis

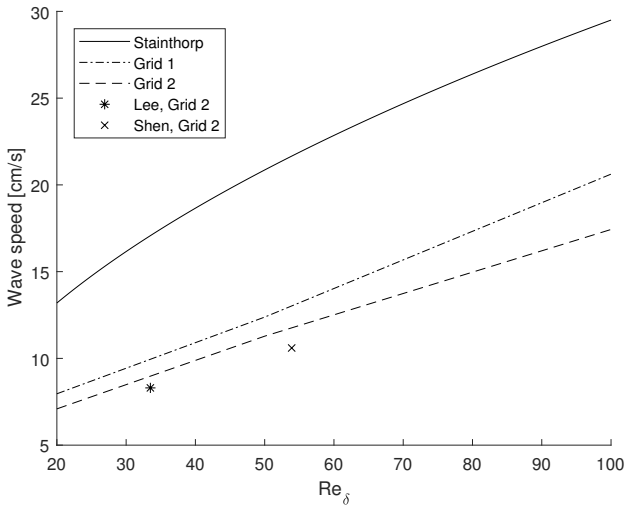

Figure 5.9: Wave speeds predicted by Stainthorp, wave speeds predicted by Fluent without condensation for two grid sizes and wave speeds predicted by Fluent with the Lee model and Shen model respectively.

The wave speeds predicted by the VOF model of Fluent are shown in Figure 5.9. In addition the wave speeds predicted by Fluent with condensation are shown for the classical Lee model and the Lee model modified by Shen. For comparison also the wave speed predicted by Stainthorp & Allen is shown in the figure. Two main *implications* are drawn from Figure 5.9:

- The wave speed at the line of inception is lower for $Re_\delta = 20, 50, 100$ on both grid sizes compared to the wave speed predicted by Stainthorp & Allen.
- The wave speed at the line of inception during condensate flow is lower than the wave speed predicted by both Stainthorp & Allen and the simulations. This is in agreement with findings from Stühltrager (see conclusion 1 in section 5.2.2).

As it is not clear how Stainthorp & Allen have defined the film Reynolds number, an alternate version of the film Reynolds number might be used. This Reynolds number is defined using the *surface* film velocity, just like in the work of Nosoko (Equation 5.10). The yielded alternative Reynolds number for condensation with the Lee model on Grid 2, and alternative wave speed using correlation 5.8 are shown below:

$$Re_0 = 13.8 \tag{5.17}$$

$$K = 2.95 \cdot Re_0^{0.5} = 11\ cm/s \tag{5.18}$$

By using the new Reynolds number of Equation 5.17 the wave speed predicted by the correlation (see Equation 5.18) is now considerably closer to the wave speeds predicted by Fluent. Yet, the wave speed is still considerably lower than wave speed in the event of condensation, agreeing to conclusion 1. Therefore it is concluded that condensation has indeed a mitigating effect on velocity of the waves at the line of inception. However, the wave speeds without condensation are a result of six simulations. So for each line, only three points are used to construct the line. To be precise, each line is constructed using data of film flow at the Reynolds (Re_δ) numbers 20, 50 and 100. In addition, the film flow (no condensation) predicted by grid 2 showed separating flow in the downstream region. All data extracted from these simulations is extracted before the film separates, and is therefore considered relevant. Finally, grid 2 refers to the grid size used by Stühltrager while grid 1 is a coarse version of grid 2. Although the same grid size is used as by Stühltrager, the different numerical approach from Stühltrager compared to this work might influence the results. Therefore, we can say that Figure 5.9 only implies that condensation slows down the wave celerity.

In order to verify the previous implication the following has to be conducted:

- Obtain a grid independent solution.
- Extract sufficient data in data from at least ten Reynolds numbers in the range from 20 to 100, to ensure that the wave speed curves are correct.

Separation during film flow

Before being able to find a grid independent solution, one has to find out why the flow is separating. During simulations extensive research was directed to this subject. However, no decisive answer was found. The separation of the flow was the main reason why the amount of data is minimal. During the conduction of the grid independency study several important observations were made:

- Shear stress on the liquid vapor interface caused by non-equal surface film velocity and vapor velocity generated the development of surface waves.
- The development of surface waves can be suppressed by mitigating the shear stress on the film surface. In this way, a completely smooth (no waves, no separation) film was obtained, even in the wavy laminar regime. However, this did not solve the problem of wave separation when wave formation is of interest.
- When the mesh count in the x-direction was increased, separation of the flow was enhanced.
- Separation of the flow occurred due to the development of surface waves. The surface wave became larger going downstream into the domain and finally the surface wave started to break up.

- The separation of the surface waves is governed by on one hand the grid size in the flow direction and on the other hand by the amplitude and speed of the surface waves.
- The grid size in the y-direction was kept constant. Therefore one might think that the aspect ratio of the grid cells would have a significant effect on the separation. However, a fully square mesh was tested and still flow separation was present.

5.3.6. Wave disturbance analysis

One of the main conclusions reported by Stühltrager stated that in the event of condensation, the phase velocity of the surface waves is mitigated (see conclusion 1). In order to assess this notion, a smooth film flow is subjected to an artificial vibration. As a result, waves will form and will travel with a well defined velocity. By excluding and including condensation in an identical case, the effect of condensation will become clear.

The yielded wave speeds will be compared to the correlation by Nosoko (Equation 5.14). All cases are ran until steady state. After, the wave velocity is extracted for the same grid and time step. The test cases are set-up in a way that they adhere to the correlation's boundaries set by Nosoko and that flow separation is avoided as much as possible.

The grid size used to by Stühltrager will again be used as base case. Yet, since previous findings implicated that the solution is not grid independent, five extra meshes will be tested.

Table 5.2: Wave speed predicted by correlation (u_w) compared to wave speed predicted by Fluent (K). (* means with condensation)

Case	Mesh ($\Delta x/\delta_0$)	$\Delta t'$	Re_δ	Re_0	We_0	$f[Hz]$	f'	u'_w	$u_w[cm/s]$	$K[cm/s]$
1	4.1	9.4	100	38	0.1217	50	0.035	1.19	15.46	15.0
2	4.1	9.4	100	38	0.1217	60	0.042	1.10	14.24	15.0
2*	4.1	9.4	100	38	0.1217	60	0.042	1.10	14.24	15.0
3	4.1	9.4	50	19	0.0381	40	0.036	1.44	11.76	11.9

In table 5.2 the wave speeds predicted by the correlation from Nosoko and the wave speeds from Fluent are depicted in the two last columns respectively. Also, relevant information about the case set-ups is shown in the table.

At first sight the wave speeds predicted by Fluent come fairly close to the wave speeds predicted by the correlation. However, it should be noted that, while extracting the data, it was found that the speeds are extremely dependent on the grid size. For instance, in case 2, the yielded ratio $\lambda/\Delta x$ is only six. As a result, the wave speed could easily be overpredicted or underpredicted to $17.5\ cm/s$ or $12.5\ cm/s$ respectively. By increasing the wavelength to gridsize ratio this effect is expected to decrease.

Apart from a very grid dependent solution, the flow of case 3 also showed signs of separation. Although case 1 did not show any sign of separation, its amplitude was almost twice that of case 2. Since experience showed that wavy flows with high velocity and wave amplitude are prone to flow separation, it was expected that the flow of case 2 would be more separation resistant than case 1. Therefore, case 2 was taken as a reference case from this point onward.

Table 5.3 shows the wave speeds predicted by Fluent for case 2 on five refined meshes. This table clearly indicates that the solution obtained in table 5.2 is not grid independent. As the wave speed yielded by Fluent closely matches with the speed predicted by Nosoko in table 5.2, table 5.3 shows that the wave speed tends to increase when the grid is refined in the x-direction. After case 2.3, the wave speed only deviates with a maximum of 3.5 percent, therefore the solution is considered mesh independent for case 2.3.

It should be noted that on grid refinement flow separation occurred. Therefore, only the waves that did show not any sign of separation were used to extract data from. Separation flow was observed for all meshes except case 2.1 and 2.2. To be consistent, the data was extracted from the first two waves for all meshes. However, using the wave speeds of all waves in the case of case 2.1 and 2.2 did not influence the result in any way. Or in other words, the wave speeds observed without flow separation turned out to be constant. Therefore, it is found reasonable to use only the first two waves for each case.

Table 5.3: Grid independency study for Case 2. (* means with condensation)

Case	Mesh ($\Delta x/\delta_0$)	$\lambda/\Delta x$	$\lambda[cm]$	$\Delta t'$	$u_w[cm/s]$	$K[cm/s]$
2.1	4.1	6	0.225	9.4	14.2	15.0
2.2	3.3	8.3	0.250	9.4	14.2	15.0
2.3	1.1	27	0.270	9.4	14.2	16.5
2.4	0.5	56	0.280	9.4	14.2	17.0
2.4*	0.5	53	0.263	9.4	14.2	16.8
2.5	0.27	114	0.285	9.4	14.2	16.6
2.6	0.11	280	0.280	9.4	14.2	17.1

Table 5.4: Assessment of wave speeds with and without(*) condensation.

Case	Mesh ($\Delta x/\delta_0$)	Δt^*	$u_w[cm/s]$	$\lambda[cm]$	$K[cm/s]$	$\lambda f[cm/s]$
2.4	0.5	9.4	14.2	0.280 ± 0.01	16.3 ± 1	16.8 ± 0.6
2.4*	0.5	9.4	14.2	0.282 ± 0.01	16.6 ± 1	16.9 ± 0.6

A thorough assessment of the wave speeds with condensation and without condensation is presented in Table 5.4. In this investigation, the speeds of the first two waves were extracted at five different times. Therefore, for each case, ten data points were used in the calculation. Also, the maximum mesh dependent error is shown. In the last column, the theoretical wave speed according to

$$u_w = \lambda \cdot f \tag{5.19}$$

is shown. Where $f = 60Hz$ is the forcing frequency applied in case 2.

From table 5.2, table 5.3 and table 5.4 the following conclusions are drawn:

- The wave speed tends to increase when the grid is refined in the x-direction.
- The grid independent solution (table 5.4) yields a wave speed with an error minimum of 8% and a maximum of 22%.
- No difference outside the error region can be found in wave speed and wave length for case 2 with and without condensation.

The effect of increasing wave speed with increasing mesh accuracy in the x-direction can be explained by looking at length of the waves. By increasing the mesh-resolution in the x-direction, the waves are captured by more grid cells. Hence, the wave lengths are more accurately predicted. As the wave frequency is set, the wave speed linearly increases with increasing wave length.

Now looking at the second conclusion, the question arises if the overprediction of the wave speed is the result of the physics or if it has a numerical explanation. As it is expected that surface tension mitigates the wave speed, the over-prediction of the wave speed in the case of a dense grid might be attributed to the exclusion of surface tension in the simulations. The effect of surface tension on the wave speed is included in the correlation (Equation 5.14) by Nosoko [96]. According to the correlation, an increase in surface tension (decrease of We_0) results in a decrease in wave speed. Therefore, it sounds reasonable that the wave speed is overpredicted when surface tension is excluded from modeling.

Theoretically, as surface tension acts to minimize the surface area of a liquid, the wave amplitude is mitigated by the surface tension. This is also seen in the simulations by Miyara [94]. But why does this result in a decrease of the wave speed? Or is it the other way around? Do high wave speeds result in high wave amplitudes? In any case, including the surface tension in the simulations proved difficult. Again flow separation started to dominate the flow. But where first the two first waves could be used, now the complete flow field was ruined by the separation.

In conclusion, the overprediction of the wave speed, caused by the exclusion of surface tension is deemed most logical. By including surface tension in the models this conclusion can be validated. However, until the problem of flow separation is solved, no explicit conclusion can be made. In summary, the event of flow separation proved to be a major limiting factor.

The fourth conclusion contradicts the observation of Stühltrager. Namely, according to the results, condensation does *not* slow down the surface waves. However, higher wave speeds in this case study compared to wave speeds in section 5.3.5 might cause the difference in wave speed between with and without condensation to be less distinct, causing it to fall within the error range. Therefore, the tests should be conducted on a finer mesh in order to reduce the error range.

In future work, when the separation problem is solved, a set-up including surface tension, generating ripple waves, can be used to explicitly verify or falsify conclusion 1 (see section 5.2.2).

5.4. Condensate flow on a baffled surface

It should be noted that the modeling approach in this section is similar to the modeling approaches in section 5.3.1. Only the working fluid is altered from R11 to methanol, while also surface tension will be included. Furthermore, the same phase change models are employed, as well as the same volume fraction discretization scheme. For the complete domain and set-up, the reader is referred to Appendix D.1.

In literature it is said that the heat transfer between the wall and the condensate flow is mainly governed by the film thickness. This means that baffles are mainly included to impose a disturbance on the film flow and cause wave formation. Due to the, waves the film thickness will decrease locally, and hence heat transfer is enhanced. This particular phenomenon is widely used to enhance heat transfer in plate heat exchangers and therefore it will be interesting to see if Fluent and the condensation models are able to reproduce it. Also it will be interesting to see if local circulation might play a role in heat transfer. In relation to section 5.3.6, a baffled surface serves the same purpose as the artificial vibration. Namely, it imposes a disturbance on the flow, causing an instability which will grow or fade out. It will be interesting to see if a disturbance imposed by a geometry will initiate the wavy laminar regime at the designated transition Reynolds number (so $Re_\delta \approx 30$).

The model is first validated using the work of Ishikawa et al [13] (see Appendix D). Next, since surface tension will play an important role in laminar film condensation, the effect of the Weber inlet number (We_{δ_0}) and the effect of the baffle height to film height (B/δ_0) is assessed. In this case study, the use of methanol as working fluid, as was used by Ishikawa, solved the problem of flow separation, implicating that fluid properties as density and viscosity are important to consider when modeling film flows.

Seven test cases are assessed. In each case either the flow rate or inlet film thickness is altered compared to the previous cases. Each of the seven cases is compared to an identical film flow case without baffles. All cases and corresponding parameters are shown in table 5.5. In the last two columns the area averaged heat transfer coefficient of a baffled surface and the corresponding flat surface are depicted, respectively.

Table 5.5: Test cases with corresponding area averaged heat transfer coefficient for the baffled surface and the flat surface for the classical Lee model.

Case	$U_b[m/s]$	δ_0/B	Re_{δ_0}	We_{δ_0}	$\overline{h}_{baffle}[W/m^2K]$	$\overline{h}_{flat}[W/m^2K]$
1	0.025	2	29	0.0045	539	655
2	0.05	2	57	0.0178	613	577
3	0.025	4	57	0.0089	612	581
4	0.05	4	114	0.0357	694	791
5	0.025	8	114	0.0178	693	784
6	0.05	8	228	0.0714	740	819
7	0.1	8	457	0.2855	781	845

At low flow rates the surface tension will dominate the flow, and will try to minimize the surface are of the liquid film. As the flow rate increases the flow will become more dominated by inertial forces than by surface tension forces. As a result, the effect of the surface tension on the film thickness will

be less visible and therefore the film is expected to adhere more to its inlet film thickness δ_0.

The ratio of inertial forces compared to surface tension forces is expressed in the Weber number. In order to increase this number, and decrease the effect of surface tension on the flow, either the flow velocity or the inlet film thickness can be increased. It is expected that when inertial forces start to dominate, since the waves cause local thinning of the film, the heat transfer in of a baffled surface will transcend the heat transfer in case of a flat surface. Now the question arises, what parameter, the velocity or the inlet film thickness, will contribute most to the increase in heat transfer?

Besides the role of surface tension, the ratio of the inertial forces to the viscous forces also plays an important role in the creation of the film. Namely, according to the Nusselt solution, the bulk velocity (see Equation 5.1) and film height are directly related. Therefore, it is expected that an identical inlet Reynolds number with differing inlet velocity/or inlet heights, will result in the creation of a more or less identical film shape.

5.4.1. Theory behind the numerics

Before we can say something about the heat transfer, we first have to define how the heat transfer is determined in Fluent. Fluent determines the wall heatflux by using the temperature gradient at the cooling wall according to:

$$q_w = k_l \frac{\partial T}{\partial n} \tag{5.20}$$

Where n represents the normal vector to the wall. Subsequently, fluent calculates the heat transfer coefficient using the wall heat flux and a reference temperature. In this case the saturation temperature.

$$h = \frac{q_w}{T_w - T_{sat}} \tag{5.21}$$

5.4.2. Heat flux validation

To be able to say something about the heat flux across a liquid film in the presence of condensation, a fully laminar liquid film is investigated. From the Nusselt theory it is known that the heat flux across the film in the fully laminar regime is only determined by the film thickness. Therefore, when steady state is reached the heat flux across the film should adhere to Equation 5.22.

$$q_{int} = \frac{k_l}{\delta}(T_w - T_{int}) \tag{5.22}$$

$$q_{theo} = \frac{k_l}{\delta}(T_w - T_{sat}) \tag{5.23}$$

where T_{int} is the temperature at the interface, and in physical conditions is equal to the saturation temperature. Figure 5.10**a** and Figure 5.11**a** show the interface temperature predicted by the classical Lee model and the Shen modified Lee model respectively. In addition, in **b**, the heat flux predicted by Equation 5.22, the heat flux predicted by Fluent and the theoretical heat (Equation 5.23) flux across the liquid film are depicted.

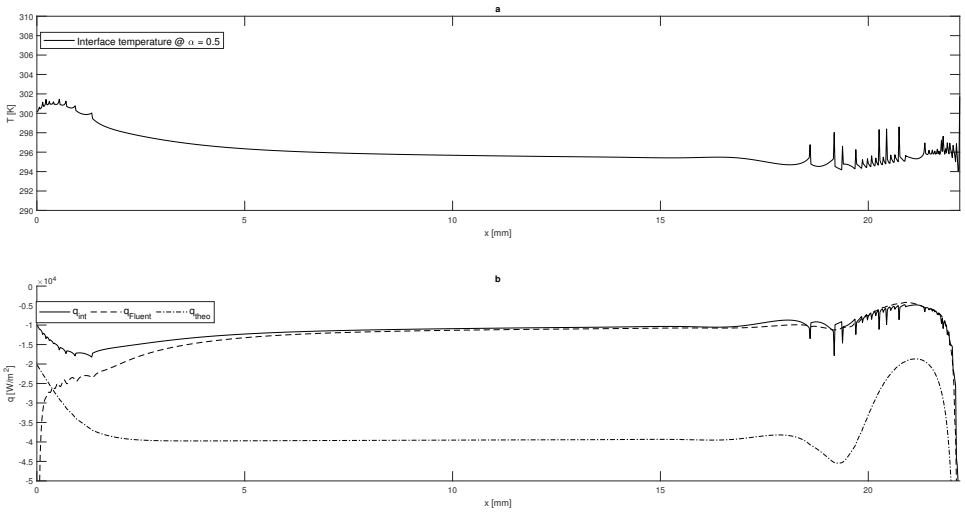

Figure 5.10: **a**: Interface temperature using the Lee model. **b**: q_{int}: Theoretical heat flux using interface temperature. q_{Fluent}: Heat flux from Fluent. q_{theo}: Theoretical heat flux using saturation temperature.

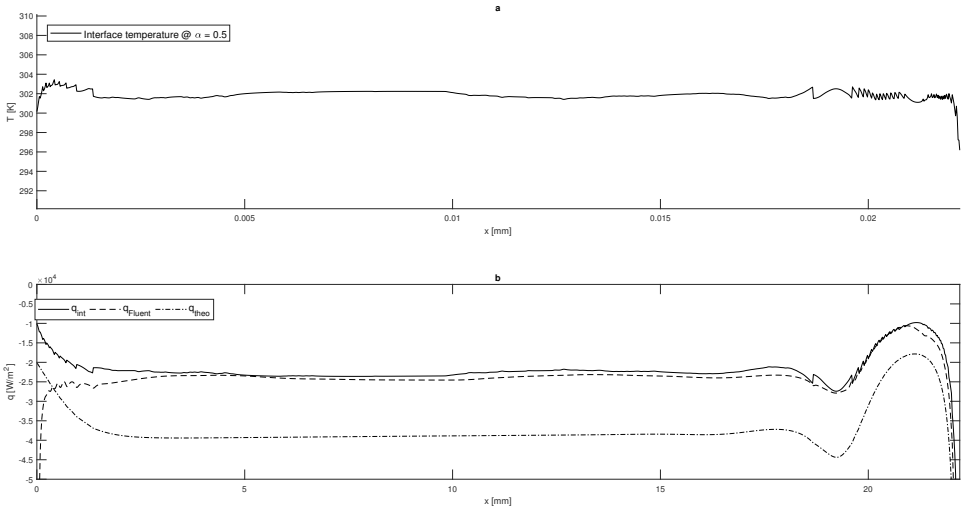

Figure 5.11: **a**: Interface temperature using the Shen modified Lee model. **b**: q_{int}: Theoretical heat flux using interface temperature. q_{Fluent}: Heat flux from Fluent. q_{theo}: Theoretical heat flux using saturation temperature.

Both figures show that the heat flux predicted by Fluent and the heat flux using Equation 5.22 are in accordance. This means that the flow is actually fully laminar, and that the heat flux is fully governed by conduction. A linear temperature profile between the phases is according to the so-called Nusselt solution, see section 4.2.1. However, the absolute theoretical heat flux is much higher than the heat fluxes from Fluent. This can mainly be attributed to the underprediction of the energy transfer between the phases, and partly be attributed to the low thermal conductivity in the two-phase region.

Due to underprediction of the mass source at the interface, the liquid side temperature is underpredicted. Subsequently, the heatflux through the liquid film is underpredicted. The Shen model addresses this problem by amplifying the thermal conductivity in the two phase region. However, the Shen model only addresses part of the problem. Namely, by amplification of the conductivity, the heat in the two phase region is transferred more easily. But since the mass transfer is still underpredicted, the latent heat that is transferred from the vapor to the liquid phase remains underpredicted. Therefore,

not enough energy is transferred to the liquid phase in order to obtain an interface temperature that approaches the saturation temperature.

In summary, the heat flux across the liquid film is fully governed by thermal conduction, agreeing to theory. However, the heat flux is underpredicted due to the underprediction of the mass transfer by the condensation model. This is partly solved by the modification by Shen. Although the Shen model performs considerably better than the classical Lee model, the Lee model will be used from now on, since this model is widely accepted in literature and therefore is more relevant.

5.4.3. Heat transfer grid independency

In order to check the dependency of the heat transfer to the grid size, three different meshes with increasing y-direction resolution were tested. Only the heat transfer performances were magnified, since Ishikawa [13] already proved that the flow field without phase change is mesh independent for mesh 1. Details of the different grid sizes are depicted in Table 5.6, where δ_* represents the local film thickness in millimeters, and is taken from Figure 5.12.

Table 5.6: Mesh sizes and mesh counts tested in grid independency study.

Mesh	$\Delta x[mm]$	$\Delta y[mm]$	$\delta_*/\Delta x$	$\delta_*/\Delta y$	Total mesh count
1	0.1	0.02	1	5.2	22200
2	0.02	0.01	5.2	10.4	222000
3	0.02	0.005	5.2	20.5	444000

Figure 5.12 shows the steady state liquid film thickness and the local temperature profile. From Figure 5.12**a** one can conclude that the is grid independent, apart from the outflow region. However, when looking at the temperature profile in the grid independent region, the temperature profiles are far from grid independent. With increasing grid resolution the temperature ramp in the liquid region (liquid region is for $y < 1\ mm$) decreases. At the same time, the two-phase region temperature ramp becomes steeper with increasing mesh resolution. First of all, the Nusselt solution shows there exists a linear temperature profile between the phases in a laminar film flow. The temperature profiles of the condensation model agree to this solution. In addition, from section 3.3.3, we know that the interface temperature will increase when the mass flow intensity coefficient r is increased. From this point of view, we expect the temperature profile to completely agree with the Nusselt solution when r is increased sufficiently. However, when r is not sufficiently high, the heat transfer between the phases is not fully governed by the liquid phase thermal resistance. Namely, it is also governed by the two-phase region, seen in Figure 5.12 at the point where the temperature ramp steepens. In conclusion, when the condensation coefficient r is not sufficiently large, the heat flux is not only governed by the liquid film resistance, but also by the two-phase resistance.

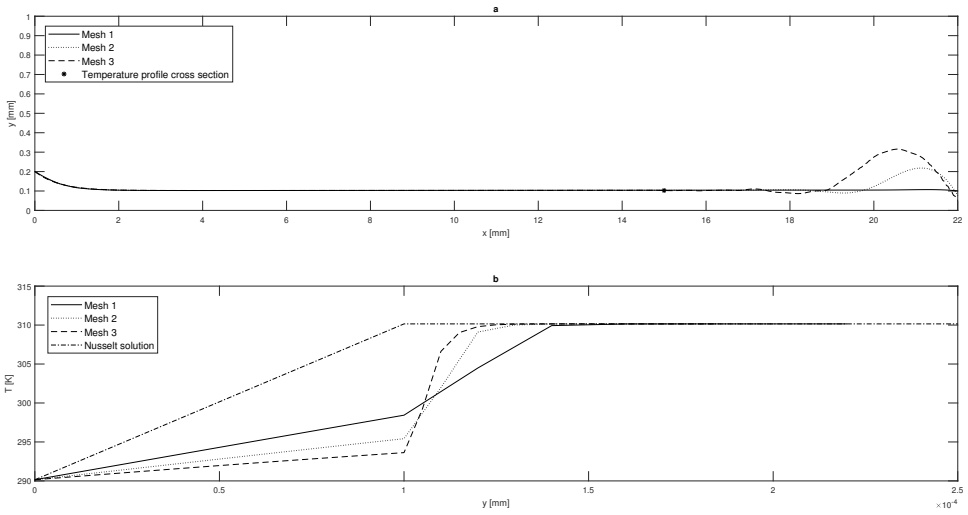

Figure 5.12: **a**: Liquid film thickness for Mesh 1: $\delta_*/\Delta y = 5.2$, Mesh 2: $\delta_*/\Delta y = 10.4$, Mesh 3: $\delta_*/\Delta y = 20.5$, **b**: Temperature profile for Mesh 1,2,3 at $x = 15mm$.

Next, one might notice that the temperature ramp in the liquid region decreases for increasing mesh count. Since Fluent directly deduces the heat flux from this ramp, the heat flux will decrease with increasing mesh count. The ramp decreases due to a decreasing interface temperature. This seems counter-intuitive, since increasing the mesh count would bring the interface relatively closer to the vapor, and subsequently closer to higher temperatures.

By increasing the mesh count in the y-direction, the interface becomes thinner in terms of absolute thickness. Yet, the computational interface (i.e. the two-phase region) is always covered over its thickness by 2 to 3 mesh cells.

Now, lets take a look at a simple example of one coarse mesh (mesh 1) and one fine mesh (mesh 2), as depicted in Figure 5.13. Steady state is assumed as well as equal film thickness. Therefore, according to the mass balance, the condensation rate for both meshes has to be equal. Subsequently, the same amount of vapor mass goes to the liquid phase in both cases. Therefore also the same amount of energy is transferred between the phases.

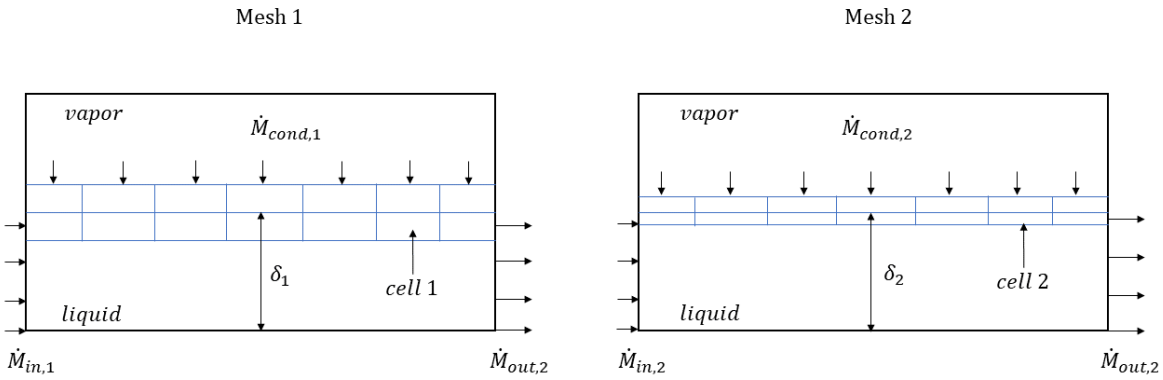

$$\dot{M}_{out} = \dot{M}_{in} + \dot{M}_{cond}$$
$$\delta_1 = \delta_2$$
$$\dot{M}_{in,1} = \dot{M}_{in,2} \quad \dot{M}_{out,1} = \dot{M}_{out,2} \quad \dot{M}_{cond,1} = \dot{M}_{cond,2},$$

Figure 5.13: Schematic representation of coarse mesh 1 (left) and fine mesh 2 (right).

$$\dot{M}_{cond,mesh_1} = \dot{M}_{cond,mesh_2} \tag{5.24}$$
$$\dot{q}_{mesh_1} = \dot{q}_{mesh_2} \tag{5.25}$$
$$T_{mesh1} = T_{mesh2} \tag{5.26}$$

With cell 1 being one computational cell of mesh 1 and cell 2 being one computational cell of mesh 2. While the condensation process takes place, the residual void gets filled with new vapor from surrounding cells. Due to the fact that the cell volume of the cells of mesh 1 are bigger than of cell volumes of mesh 2, the vapor volume fraction of cell 1 will be slightly bigger than of cell 2. Since the vapor density is very small compared to the liquid density this difference is negligible.

$$\alpha_{v,mesh_1} \approx \alpha_{v,mesh_2} \tag{5.27}$$

In the first step the mass transfer was assumed. Now we let the condensation model 5.28 determine the mass transfer.

$$\dot{m}_{vl} = r\alpha_v\rho_v\frac{T_{sat} - T_{cell}}{T_{sat}} \tag{5.28}$$

Since the vapor fractions in case 1 and case 2 are almost identical, $\dot{m}_{vl,mesh_1} \approx \dot{m}_{vl,mesh_2}$. However, $\dot{m_{vl}}$ is the amount of mass transferred per unit time, per unit volume. The real mass transfer, i.e. $\dot{M}$, between the phases, is the mass transfer per unit time calculated according to:

$$V_{cell,mesh_1} = 2V_{cell,mesh_2} \tag{5.29}$$
$$\dot{M}_{mesh_1} = V_{cell,mesh_1} \cdot \dot{m}_{lv,mesh_1} \tag{5.30}$$
$$\dot{M}_{mesh_2} = V_{cell,mesh_2} \cdot \dot{m}_{lv,mesh_2} \tag{5.31}$$

This means that when cell volume 1 is twice the volume of cell 2, the mass transfer between the phases is also twice as large. Because the energy transfer between the phases is linearly dependent on the mass transfer, there is also twice as much energy transferred in case 1. Therefore, the resulting steady state temperature at the interface is higher for coarser meshes.

In the simulations, the same trends as mentioned above were witnessed. In summary, the poorly defined dependency of the condensation model on the local cell volume causes the underprediction

of the heat transfer when the mesh count in the condensation direction is increased. Although this error is expected to vanish when the condensation coefficient is increased, this error strongly affects the practicality of the condensation model. Namely, having to increase the condensation coefficient brings lots of extra CPU effort, as was shown in section 4.3.2. In addition, the dependency of the mass transfer and energy transfer on the cell size, forces one to adjust not only r for each configuration, but also the cell size.

5.4.4. Overall results

Film shape

The steady state film shapes for the flat cases and baffled cases (from Table 5.5) are depicted in Figure 5.14 and Figure 5.15, respectively. In both the flat cases and baffled cases, case 1 to 6 show a steady film profile from $x = 7.5\ mm$ to $x = 20\ mm$, whereby steady means that the mean film thickness remains constant. Before $x = 7.5\ mm$ inflow conditions influence the film shape. After $x = 20\ mm$ the outflow condition affects the film shape. For this reason, results presented will be taken from this inner steady region. The outflow region is affected by the outflow boundary condition. Namely, the outflow boundary was specified with a vapor backflow. Therefore, the no liquid is present on the wall in the outflow region and subsequently wall adhesion forces the film to take this curvy shape. This was substantiated by the observation that increasing the domain length, forced the sinusoidal outflow region to move with the increasing domain length. Moreover, case 7 is disposed of entirely, since no steady profile is obtained in this domain.

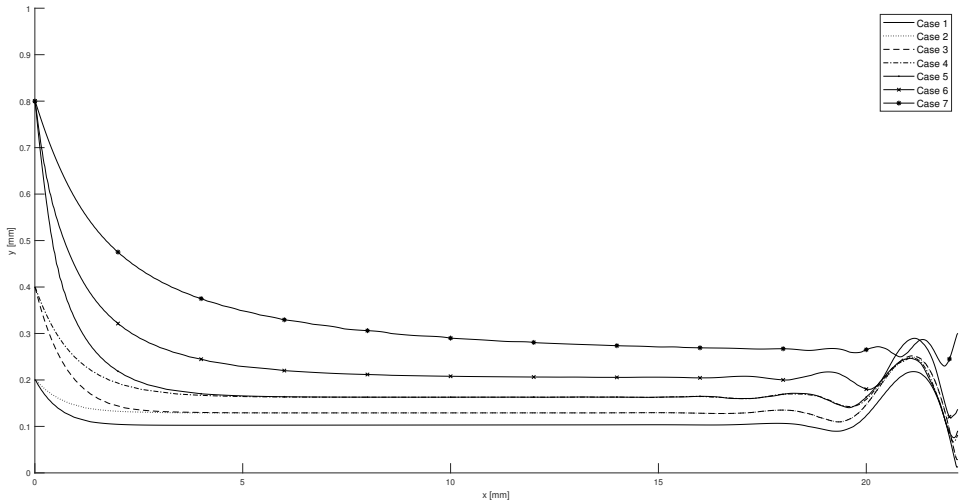

Figure 5.14: Film thickness for case 1 to 7 corresponding to a flat surface.

It is interesting to see that in both the flat cases and the baffled cases, the film thickness seems to be entirely governed by the ratio of the inertial forces and viscous forces. Although, for instance from case 2 to 3 the inlet Weber number decreases, both films show an almost identical shape. This can mainly be attributed to the laminar film flow regime. Namely, for laminar film flow the film velocity and film thickness are related. This is also called the Nusselt solution. Aleensko et al [100] have shown this for smooth laminar flow, while Lel et al [101] have also shown this in terms of mean film thickness for wavy laminar flow. As a result, noting that the film thickness decreases and the linear relation between the bulk velocity and the film thickness, keeping the Reynolds number constant, the film bulk velocity will increase (see Equation 5.1). Investigation of local bulk velocities agree with this finding, meaning that the bulk velocity has indeed increased. From this, the conclusion is drawn that the flow adheres to the Nusselt solution.

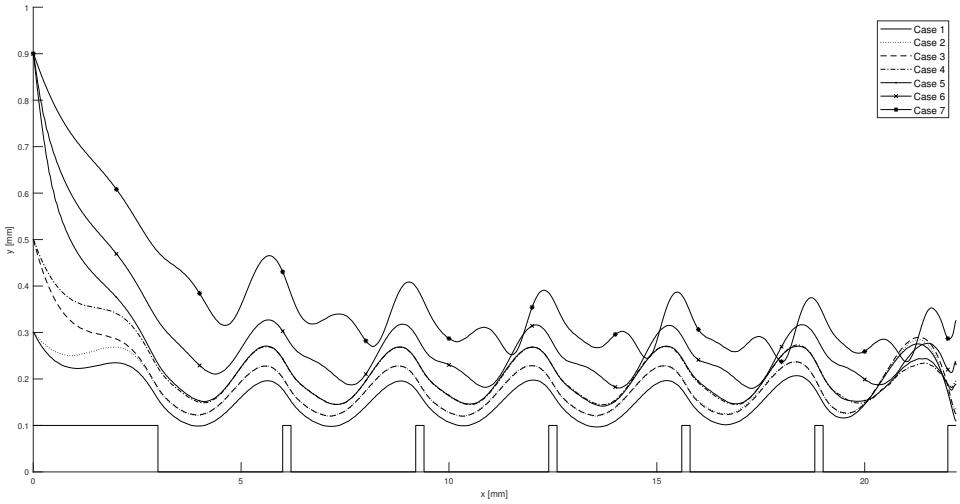

Figure 5.15: Film thickness for case 1 to 7 corresponding to a baffled surface.

Now taking a closer look at Figure 5.15 and Figure 5.16, one can see that the crest to trough height linearly increases for increasing Reynolds number. This is in accordance with Argyriadi [102]. However, Argyriadi only showed this for an inclined baffled plate with angles $\theta = 1.3°$ to $\theta = 5.4°$. In this study the corresponding angle for vertical downflow is $\theta = 90°$. The baffle height to baffle period tested in Argyriadi are $1/60$, $1/30$ and $1/15$. In this study the baffle height to baffle period is $1/30$. So the baffle geometry corresponds to Argyriadi's geometry, while the contact angle does not agree. For complete validation of the linear increase in crest to trough height, experiments should be conducted with a ninety degrees inclination angle. Until then, the linear increase in the results of Figure 5.16 seems to be in line with the findings of Argyriadi, but is not completely validated.

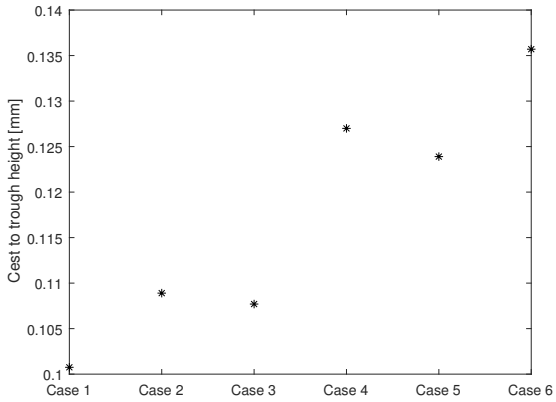

Figure 5.16: Crest to trough height for first wave in Figure 5.15 after $x = 10\ mm$. Crest to through height pictured for Case 1 (Re =29), Case 2 (Re = 57), Case 3 (Re =57), Case 4 (Re = 114) , Case 5 (Re = 114), Case 6 (Re = 228)

Global heat transfer

Figure 5.17 shows the mean film thickness for the flat and baffled cases. In addition the corresponding area averaged mean heat transfer coefficients (from Table 5.5) are depicted. From Incropera [9] we know that the heat transfer in laminar flow is governed by the liquid film thickness according to Equation 5.32.

$$h = \frac{k_l}{\delta} \tag{5.32}$$

The comparison between the mean heat transfer coefficient and the mean film thickness raises the question why the heat transfer is increasing with increasing film thickness.

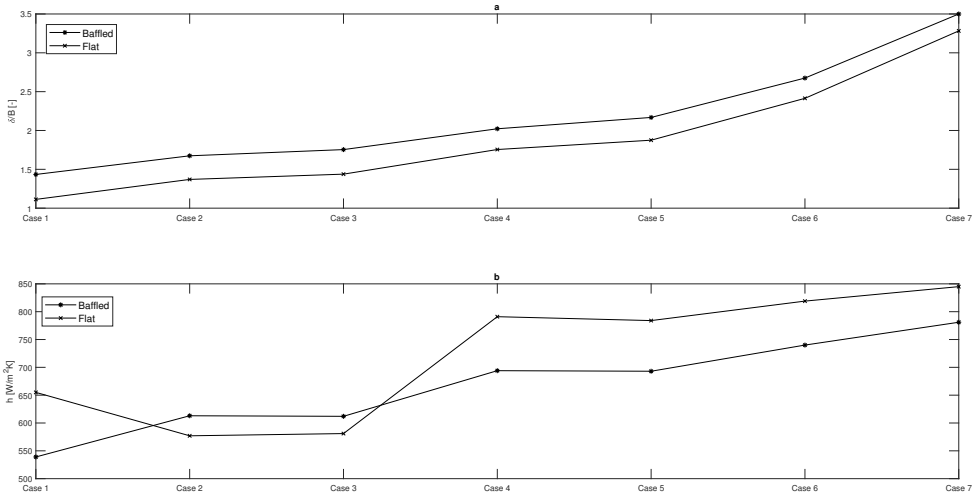

Figure 5.17: **a**: Mean film thickness normalized with baffle height B for case 1 to 7. **b**: Mean heat transfer coefficient from Fluent for baffled & flat case 1 to 7.

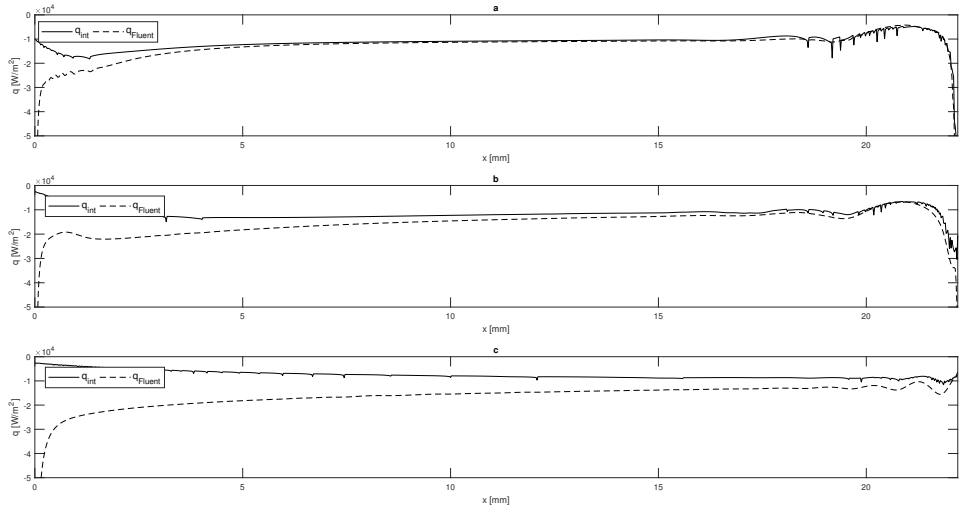

Figure 5.18: Heat flux across interface and heat flux given by fluent for a flat surface. **a**: Case 1 (Re = 29) **b**: Case 5 (Re = 114) **c**: Case 7 (Re = 457)

Figure 5.18 shows that the heat flux constructed using Equation 5.22 (q_{int}) and the heat flux given by Fluent. As can be seen, the heat flux predicted by Fluent diverges from the interface heat flux with increasing Reynolds number. This raises the question whether this is caused by enhanced heat transfer or if boundary conditions might influence the flow field. The inflow boundary is specified with a constant temperature profile of $T_{in} = 310.15\ K$ (see Appendix D.1). The temperature profile at the beginning of the domain might be affected by this inlet condition. In order to check up to what distance the temperature profile is affected by the inlet condition, one can use an approximation for the thermal penetration depth δ_p.

$$\delta_p \approx \sqrt{4\alpha_{thermal} t} \tag{5.33}$$

where $\alpha_{thermal} = \frac{k}{Cp_l k_l}$ and represents the thermal diffusivity. This approximation tells us what distance the thermal energy diffuses in a certain time t. The time t is deduced using the steady state film thickness and therefore differs in each case. By multiplying the time t with the bulk Nusselt velocity, the development distance is obtained.

$$x_{development} = \frac{\delta_{p,ss}^2}{4\alpha_{thermal}} U_{b,ss} \tag{5.34}$$

where $\delta_{p,ss}$ represents the steady sate film thickness and $U_{b,ss}$ the bulk velocity at the steady state film thickness. The steady state film thickness for each flat case is shown in Figure 5.14. From this figure it already can be seen that the film of case 7 is still developing. For the other cases, taking the steady state thickness seems reasonable, since from $x = 7.5mm$ the mean film thickness remains constant. In addition to the steady state film thickness (Nusselt thickness), the steady state bulk velocity (Nusselt velocity) is used.

By making use of the thermal penetration depth, it was discovered that in case 1, the domain is long enough for a fully developed temperature profile. This was also seen in the solution, by plotting the temperature profile along x. For all other cases the temperature field was not fully developed. Due to the influence of the inflow and outflow boundaries, no sensible statements can be made about the heat transfer coefficients for case 2 to case 7. The thermal penetration depth showed that even for a relatively low Reynolds number of $Re_\delta = 57$, already a domain of around thirty millimeter is needed. Taking note of the practicality that condensation models need very fine meshes in order to show fundamental flow phenomena, such a domain would require a huge amount of computational cells.

5.4.5. Local heat transfer behavior

One should note that the geometry shown in the figures only corresponds to the baffled case. The film thickness for the flat surface is measured from $y = 0\ mm$.

Case 1

The film thickness for case 1 for a baffled surface and a flat surface are depicted in Figure 5.19**a**. Also the corresponding heat transfer coefficient along the wall is plotted in Figure 5.19**b**.

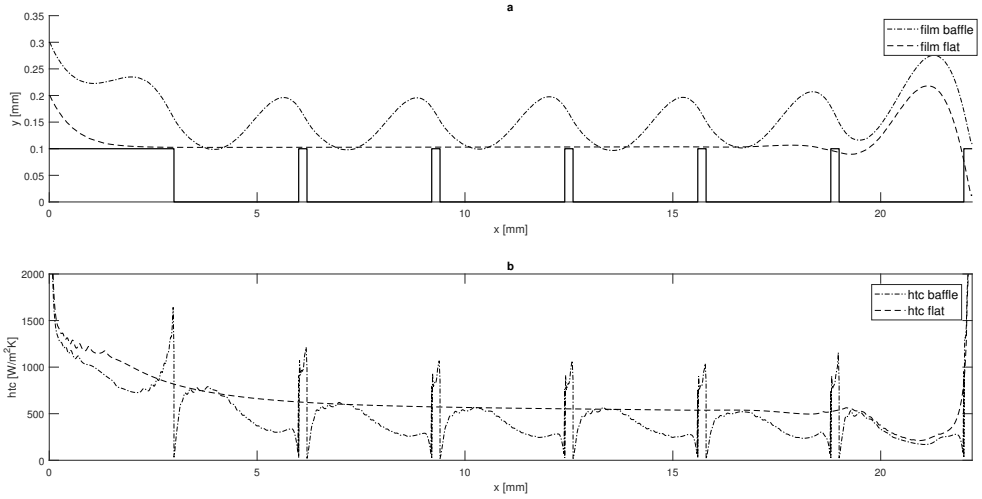

Figure 5.19: Case 1: $Re_0 = 29$ **a**: Steady state film shape for baffled surface and flat surface, **b**: Local heat transfer coefficient for baffled surface and flat surface

The first thing that jumps out from Figure 5.19 is that the heat transfer in the case of a flat surface is higher compared to the baffled surface. This can be attributed to the extra resistance from a thicker liquid film. In the figure, the locations where the film thickness of the baffled case and flat case are

equal, the heat transfer coefficient is also equal. This fact substantiates that the heat transfer is only governed by the liquid film resistance. The heat transfer peaks shown in Figure 5.19**b** are a result of a local minimum in film thickness. The local minimum in film thickness can be attributed to the baffles.

Figure 5.20**a** shows the absolute liquid film thickness for the baffled case. Using the absolute thickness, the theoretical heat transfer coefficient can be determined using Equation 5.32. For comparison purposes the theoretical heat transfer is normalized using the mean heat transfer coefficient predicted by Fluent. By doing so, the exact local difference between the local theoretical heat transfer and the heat transfer predicted by Fluent is depicted in Figure 5.20**b**. Looking at the figure, the influence of the inflow boundary is clearly visible. After the thermal development length is reached (at around 15 millimeter), the heat transfer coefficients agree very well. Therefore, we can conclude that the heat transfer is indeed entirely governed by the liquid film thickness, as is expected in the laminar flow regime.

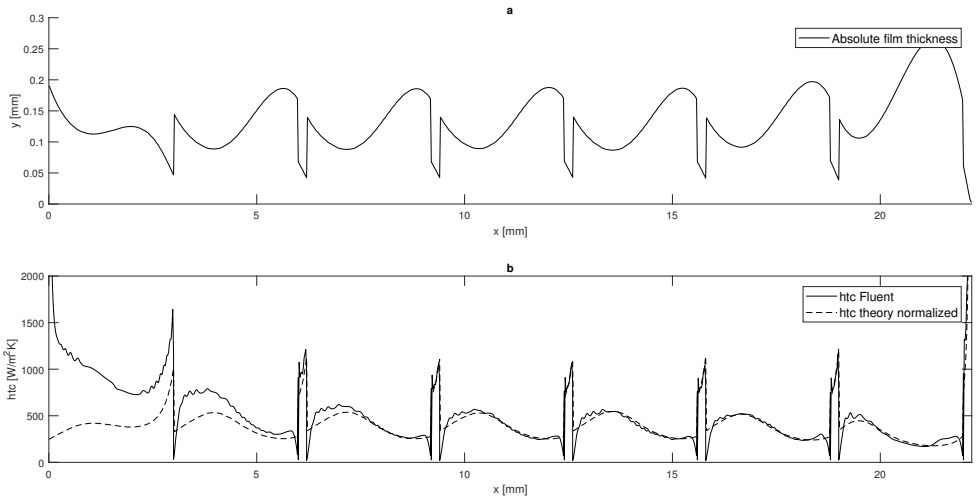

Figure 5.20: **a**: Absolute film thickness, **b**: Heat transfer coefficient from fluent vs theoretical normalized heat transfer coefficient.

Next, due to the baffles, the film is not able to converge to the Nusselt solution. Therefore, the mean film thickness is higher compared to the flat case. Although, heat transfer is enhanced locally, it does not outweigh the effect of the higher mean film thickness. In conclusion, when using baffles in a laminar film flow, one should be careful in choosing baffle height. Or to be more explicit, the Nusselt thickness to baffle height δ_{Nu}/B is the leading factor in the enhancement of heat transfer. Clearly the ratio shown in Figure 5.19 is chosen poorly. Maybe heat transfer will be enhanced when this ratio is increased from 1 to 2. However, since the mean film thickness will not decrease, the effective enhancement of heat transfer per square meter will still be considerably small.

What is more, the extra surface due to the baffles does not seem to enhance the total heat transfer. Looking at the lower baffle corner regions, no considerable heat transfer is witnessed. This might be attributed to the local zero velocity in the corner region. Due to the low flow velocities, the lower part of the liquid is almost not moving. Therefore, no mixing occurs and subsequently the temperature is almost constant in the x-direction. Consequently, the extra baffle surface used does not contribute to the heat transfer.

Case 2

Case 2 of Table 5.5 was re-simulated on a larger domain, to account for the thermal development length (see Equation 5.34). Figure 5.21 shows the film shape for a baffled surface and a flat surface. Also the local heat transfer coefficient for both surfaces is depicted. At first sight Figure 5.21 looks a lot like the film evolution and local heat transfer coefficient of case 1 (Figure 5.19). However, taking a closer look at the film shape at the end of the domain reveals two important difference. First, the film shape shows unsteady behavior (sinusoidal waves are disturbed). Secondly, the local heat transfer coefficient of the baffled surface is higher than the heat transfer coefficient of the flat surface.

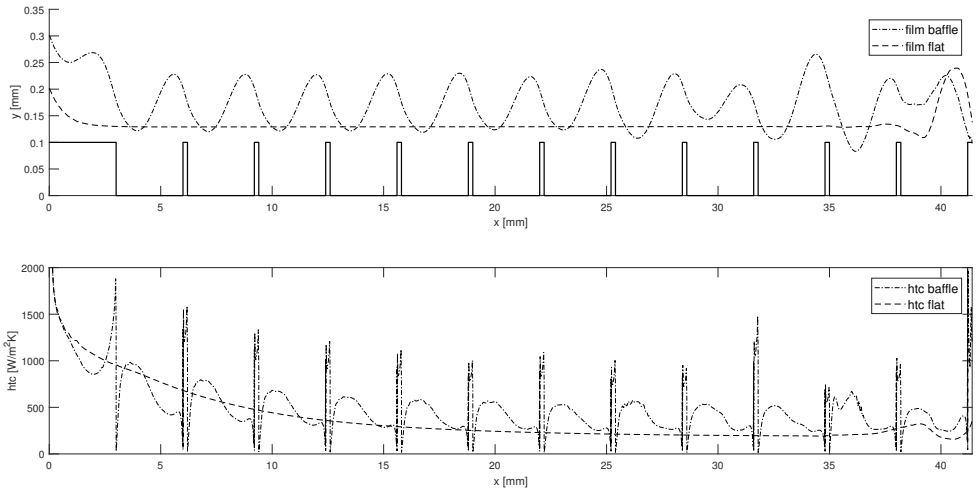

Figure 5.21: Case 2: $Re_0 = 57$ **a**: Unsteady film shape for baffled surface and steady state film shape for flat surface, **b**: Heat transfer coefficient for baffled surface and flat surface

The first difference can be explained with Figure 5.23. Figure 5.23 shows the local Reynolds number evolution of the flow over the baffled surface and flat surface respectively. In case of the baffled surface, the local Reynolds number first remains more or less constant, but from $x \approx 23\ mm$ the local Reynolds number starts to show sinusoidal behavior. This behavior is an indicator for entering the unsteady wavy laminar regime. Although the Reynolds number already exceeds the transition Reynolds number for the wavy laminar regime, the flow over the flat surface remains in the fully laminar regime. This can be deduced from the fact that the local Reynolds number for the flow over the flat surface remains constant. Therefore, we can conclude that the baffles induce a disturbance on the flow, causing an instability to continuously grow, which initiates the wavy laminar regime. Figure 5.22 shows the local Reynolds numbers for case 1 ($Re_0 = 29$). For both the baffled surface and the flat surface the local Reynolds number is more or less constant (apart from the outflow boundary), meaning that both flows remain in the fully laminar regime. Therefore, one can say that the wavy laminar regime only gets initiated from the transition Reynolds number threshold on-wards. This agrees to the theory that in the fully laminar regime, an instability dies out and the flow becomes steady. Whereas in the wavy laminar regime, an instability grows indefinitely, causing unsteady flow behavior. Therefore we can conclude that in case 1, although waves are present, the flow is not in the wavy laminar regime.

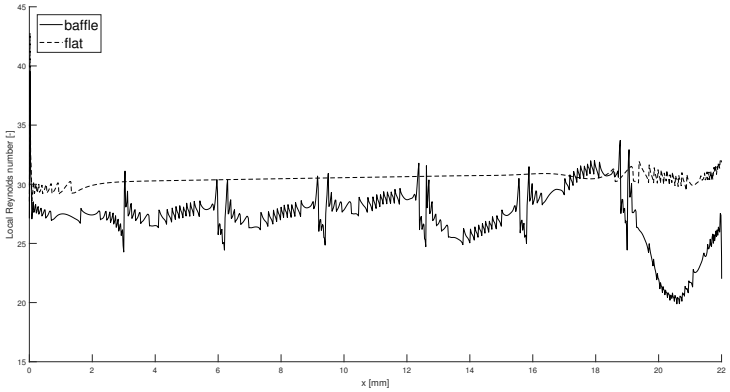

Figure 5.22: Case 1: $Re_0 = 29$. Local Reynolds number for baffled surface and flat surface

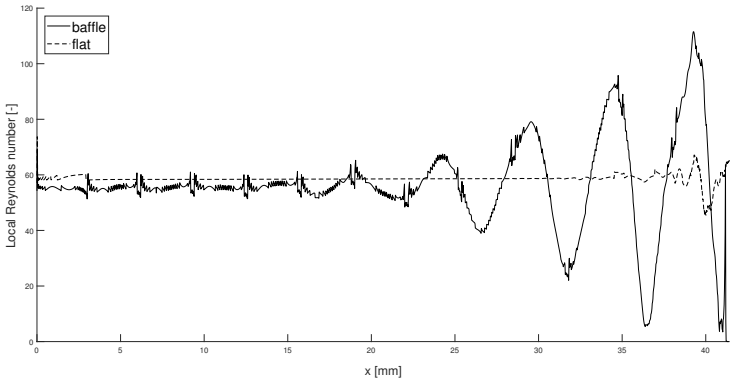

Figure 5.23: Case 2: $Re_0 = 57$. Local Reynolds number for baffled surface and flat surface

Figure 5.24 and Figure 5.25 show the local flow behavior and temperature contours for case 1 and case 2 respectively. Both domains are chosen so that the development length threshold (see 5.34) is reached. In addition, the mean film thickness over the domain, the mean heat transfer coefficient over the domain and the mean bulk velocity are stated in the figure description. First, the heat transfer coefficient of the flat surface in case 2, decreases with respect to the heat transfer coefficient of the flat surface in case 1. Since both flows are fully laminar, this can be attributed to Equation 5.32, which states that the heat transfer coefficient linearly decreases with increasing film thickness. However, the decrease in heat transfer coefficient is almost twice as much as would be expected. At this point, it is hard to think of an explanation. But, remembering the underprediction of heat transfer caused by mesh size (see section 5.4.3), the numerics of the phase change model might play a role again. When comparing baffled case 2 with baffled case 1, the heat transfer coefficient increases, even though the mean film thickness also increases. Therefore, one can conclude that heat transfer in not only governed by conduction, but that convection also plays a part.

The flow field for both case 1 and case 2 (Figure 5.24**b** & Figure5.25**b**) for a flat surface show to adhere to the Nusselt velocity profile. Only, at surface the velocity points a little bit into the domain, showing the effect of the outflow boundary on the velocity.

When comparing Figure 5.24**a** and Figure 5.25**a**, the flow field is more or less similar. The flow decelerates when approaching the baffle at $x \approx 15.5\ mm$ and $x \approx 31.5\ mm$, for case 1 and case 2 respectively. Subsequently, there exists a small region near the baffle lower left corner of quiescent fluid. Due to the quiescent fluid, the wave reaches it's local maximum before reaching the baffle. After the local maximum, the absolute film thickness decreases, causing the flow to accelerate over the baffle. Again, there exists a quiescent region of fluid on the right bottom corner of the baffle. In the flat film region, the velocity profile takes the parabolic shape of the Nusselt solution (see B.5).

Compared to case 1 only the mean bulk velocities increases for case 2. We know that for increasing velocity, the convective heat transfer increases. However, for the flat surfaces, also the mean bulk velocity increases for case 2 (compared to case 1), but heat transfer is not increased. Therefore, it sounds reasonable to believe that heat transfer is not enhanced by steady convection. In order to find the effects of the unsteady convection, one should study the time averaged behavior and heat transfer of the flow. In unsteady wavy laminar flow, the propagating waves can consist of local circulation zones, which enhance heat transfer. In high Prandtl number fluids, the heat transfer due to convection can amount to a considerable portion of the total heat transfer [92][103]. However, the Prandtl number used in this study is $Pr = 4$, which lies exactly in between the ranges that are referred to by Miyara (see section 5.2.1). In order to find the effect of convective heat transfer in wavy laminar flow, one should conduct a study to the unsteady behavior of the waves. Or in other words, use the method presented in section 5.3.3 to expose the circulation zones and other effects of unsteady convection in combination with a baffled surface as presented in this section. In addition, one should use a high Prandtl ($Pr > 10$) number fluid to ensure the convective effects are considerable.

The effect of unsteady convection can be seen when comparing the temperature contours of Figure 5.24**a** (case 1) & Figure 5.25**a** (case 2) at $x \approx 18.5\ mm$ & $x \approx 34.5\ mm$, respectively. The temperature contours of case 2 are more horizontally oriented compared to the temperature contours of case 1. This might be attributed to a small local circulation that pushes the contours to the bottom left, just

as was shown in section 5.3.3. Also, the density of the temperature contours of case 2 is higher than of case 1, indicating heat transfer enhancement. However, until the unsteady convection effects are exposed, the existence of a circulation zone remains an educated guess.

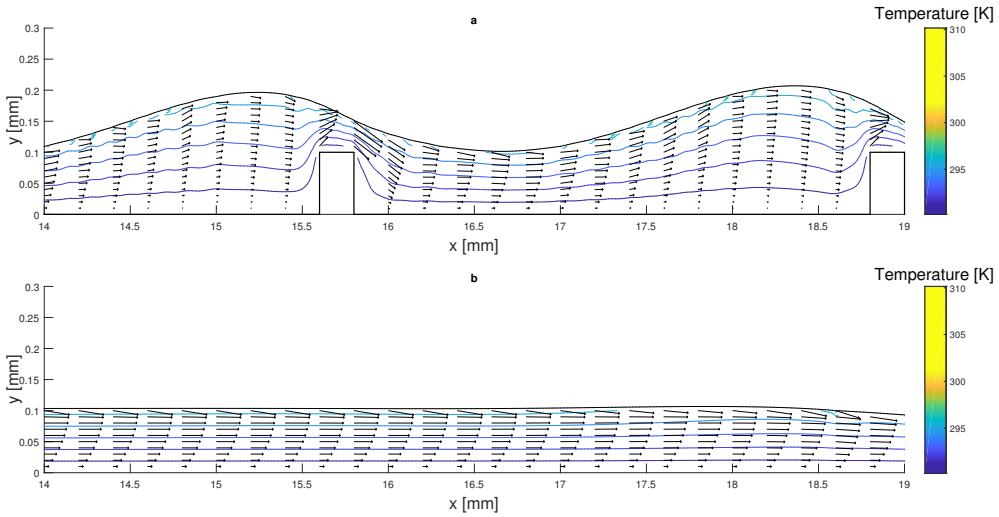

Figure 5.24: Case 1: $Re_0 = 29$. Vector plot with Temperature contours.
a: Baffled surface with $\overline{h}_{x=14-19\ mm} = 338\ W/m^2K$, $\overline{\delta}_{x=14-19\ mm} = 0.137\ mm$, $\overline{U}_{bx=14-19\ mm} = 0.042\ m/s$.
b: Flat surface with $\overline{h}_{x=14-19\ mm} = 530\ W/m^2K$, $\overline{\delta}_{x=14-19\ mm} = 0.104\ mm$, $\overline{U}_{bx=14-19\ mm} = 0.052\ m/s$

.

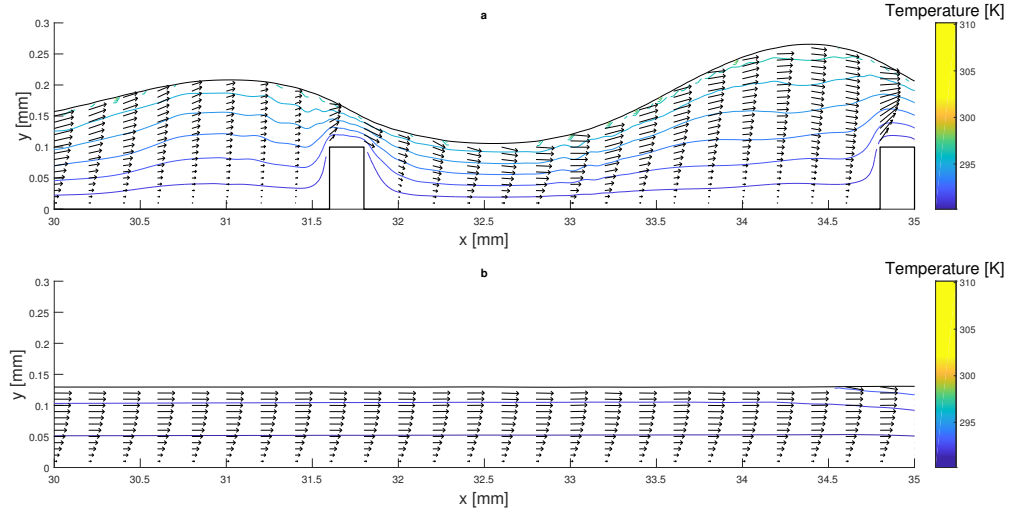

Figure 5.25: Case 2: $Re_0 = 57$. Vector plot with Temperature contours.
a: Baffled surface with $\overline{h}_{x=30-35\ mm} = 380\ W/m^2K$, $\overline{\delta}_{x=30-35\ mm} = 0.163\ mm$, $\overline{U}_{bx=30-35\ mm} = 0.065\ m/s$.
b: Flat surface with $\overline{h}_{x=30-35\ mm} = 195\ W/m^2K$, $\overline{\delta}_{x=30-35\ mm} = 0.130\ mm$, $\overline{U}_{b,x=30-35\ mm} = 0.080\ m/s$.

In conclusion one can say that the baffles induce an instability on the film flow, causing the film to enter the wavy laminar flow regime. In this flow regime, heat transfer is enhanced by convection. However, in this study the way that convection enhances heat transfer did not become clear. In order to find the underlying mechanism for convective heat transfer enhancement in baffled channels, one should conduct a time-dependent study to wavy laminar flow over a baffled surface.

5.5. Conclusion & Recommendations

The VOF model is able to properly predict the wave motion described by Stühltrager [89]. However, due to the underprediction of the film thickness by the condensation models, not all flow features were able to express their selves. Namely, no wave merger was observed. The VOF model is in this sense constrained by the condensation model. In other words, there is no reason to believe that the VOF model is not able to predict wave merger in a correct manner. In future work, it would be interesting to see if also the wave merging can be modeled by Fluent. By making use of a larger domain or a higher condensation frequency r this can be achieved. However, both the increase of the domain size or the condensation frequency will bring a considerate increase in computational effort.

One of the main conclusions by Stühltrager was partly validated and partly falsified. Namely, in the mimicked model the condensation seemed to indeed slow down the ripple waves. However, separation of flow in the control set up posed difficulties. Therefore, only three different Reynolds numbers could be tested, resulting in insufficient comparing material.

The next control set up was again tormented by flow separation. Yet, Fluent was able to reproduce the wave speeds induced by an artificial vibration reasonably. However, due to the error, the difference in wave speed with and without condensation could not be magnified.

Altogether, the VOF multiphase model of Fluent seems to be able to reproduce physical wave flow phenomena. However, due to the nagging effect of flow separation it was hard to thoroughly test the condensation models performance. Apart from the underprediction of the interface mass transfer and subsequently the film thickness, the condensation models seem to slow down the ripple waves. This was however not explicitly validated.

In terms of heat transfer, the condensation models are able to simulate the linear temperature slope typical for conduction driven heat transfer. However, when using the condensation models, the heat transfer is not entirely governed by the liquid film. Namely, the total heat transfer is governed by the liquid film and the two phase region created by the condensation model. As the condensation model underpredicts the mass transfer, also the heat transfer is underpredicted.

Interesting to see is that the total heat transfer decreases when wall-normal mesh count is increased. This was attributed to the definition of the mass transfer in the condensation model.

When simulating heat transfer problems, one should be aware of the thermal penetration depth. In this work it was found that the thermal penetration depth significantly constrains the modeling options. Namely, when increasing the Reynolds number, a much larger domain is needed. As the mesh count used in section 5.4 was already more than $2 \cdot 10^5$, enlarging the domain would, again, require a considerable amount of extra CPU effort.

By simulating fully laminar flow over a flat surface and a baffled surface, it was found that under laminar conditions, irrespective of waves, the heat transfer is fully governed by the liquid film thickness. This agrees to Nusselt's theory. Therefore, one can conclude that Fluent adheres to Nusselt's theory in the laminar flow regime. In addition, when the Reynolds number was increased above the transition Reynolds number, it was found that the baffles forced the film flow to enter the wavy laminar regime, whereas the film flow over the flat surface remained fully laminar. In the wavy laminar regime, the heat transfer seemed to be also governed by convection, rather than by conduction only. This was however not explicitly verified.

In terms of heat transfer, future work should focus on the heat transfer's dependency on the numerical interface. After these issues are solved, the investigation to the contribution of convection to heat transfer in the wavy laminar regime in baffled channels will be the next stage in understanding the heat transfer mechanism in plate heat exchangers.

6

Conclusions & Recommendations for future work

6.1. Conclusions

This study started with the investigation to the applicability of Computational Fluid Dynamics to the design of condensation plate heat exchangers. One of the most interesting articles on the topic of phase change modeling is the review by Kharangate & Mudawar [41]. By reading this article one is pointed in the right direction and has a vast source of references to consult with. After a thorough research of the available literature, it is concluded that significant progress is made in this field. However, one of the main problems remains the phase change model itself. The phase change model turned out to be the leading factor in the stability of the models and their accuracy. Moreover, the leading model used throughout literature makes use of an arbitrary constant. Therefore, the physical base of the model is questionable and the big advantage of CFD over empirical models is nullified. Namely, the arbitrary constant needs to be fine tuned for every particular application, thereby making it less appropriate for design purposes. Also it was found that studies have been restricted to simple geometries. For instance, no corrugated channels in combination with phase change have been modeled.

By analyzing the accuracy of the phase change models versus the real computation time needed, the practicality of the models was investigated. It was concluded that the accuracy of the classical Lee model [58] and the modification of the Lee model by Liu [10] increases linearly with increasing computation time. The Shen [6] modified Lee model showed an exponential relation between the real computation time and the film thickness accuracy. Therefore the Shen model is deemed most practical in the modeling of the Nusselt condensation problem. However, for all models heaps of time were needed to reach convergence. Taking into account that only a simple two-dimensional laminar flow was modeled, one can imagine that modeling a full plate heat exchanger will be impractical.

There is no reason to believe the multiphase VOF model is not able to track interfaces properly. Complicated flow phenomena such as wave evolution and local circulation were properly modeled. Yet, one should always be careful when using FLuent, since the set-ups are prone to non-physical flow separation. Condensation seemed to slow down the wave celerity, which is in accordance with the findings of Stühltrager [89]. However, due to the problem of flow separation, insufficient data was obtained to validate this conclusion. What is more, Fluent was able to to show the effect of a local circulation in wavy laminar film flow over a flat surface in accordance with the findings of Stühltrager[90] and Miyara[11].

A mesh independency study revealed that the heat transfer prediction by the condensation models is very dependent on mesh size. Even up to a mesh count of almost half a million cells, no mesh independent solution was obtained. This again underlines the constraints set by the condensation models. Increasing the mesh count in the wall normal direction leaded to a counter-intuitive decrease of the heat transfer accuracy. This was attributed to the way the mass transfer intensity depends on the local cell volume.

Due to slow heat diffusion, relatively large domains are needed if one wants to model beyond the fully laminar film flow regime. Together with the dense meshes needed to account for interfacial mass

and heat transfer, this was deemed impractical.

The effect of baffles on film flow in the fully laminar regime and in the wavy laminar regime was investigated. It was found that baffles impose an perturbation on the flow, causing the flow to enter the wavy laminar regime. For a flat surface, the film flow remained fully laminar, even though the flow's Reynolds number exceeded the wavy laminar transition Reynolds number. In the wavy laminar regime, heat transfer was not only governed by conduction, but also by unsteady convection. In addition, heat transfer increased with increasing film thickness, indicating that unsteady convection enhances heat transfer. However, the contribution of unsteady convection to heat transfer was not quantified.

In the end, CFD phase change models are not mature to enough overcome the stability issues. Until CPU performance increases significantly or the models mature, fundamental modeling of condensation flow will be restricted to simple geometries or particular cases. In other words, a fundamental CFD model encapsulating all flow features related to phase change in a plate heat exchanger is rather far away.

6.2. Recommendations

Until a huge improvement is made in either the stability issues of the models, or the CPU performance of present computer clusters, the modeling of a full plate heat exchanger with phase change and turbulent structures will be far away. Recommendations for future work are therefore directed to improvements in existing phase change models and developing new phase change models. The focus has to be on developing fundamental models that can cope with the almost discontinuous transition at the interface, which generates the instabilities. However, since the work of Lee (1980) no real alternatives have emerged. Therefore, the improvement of CPU performance seems more probable than the improvement of the fundamental phase change models. Consequently, one should think of other approaches to CFD modeling. For instance, by developing a code solely for condensation modeling, computational effort might be saved. Finally, the work of Aissa [87] has showed that CFD-simulations can be accelerated by using GPUs instead of CPUs. Therefore, efforts should be made to quantify the possible decrease in real computation time when GPUs are employed.

In terms of heat transfer, improvements can be made in developing phase change models that are able to estimate heat transfer independent of mesh size, while also the conservation of mass is satisfied.

The next stage in the understanding of heat transfer mechanism in plate heat exchangers is the modeling of wavy laminar film flows in corrugated channels. The study should focus on time-dependent convective heat transfer mechanism such as local circulation. The fluid Prandtl number should be more than 10, to make the effect of convection on heat transfer distinct. Additionally, the simulated domain should be large enough to account for the thermal diffusion. However, by doing so, the domain becomes computationally large, therefore limiting the the ability of modeling high Reynolds number flows.

From a practical point of view, if the fundamental flow structures are of secondary importance, one can think of using CFD only for heat transfer predictions. It would be interesting to see if the CFD models can reproduce the heat transfer from experiments. Since experimental data is available for Bluerise, this seems the most logical step towards using CFD as a predictive tool. Additionally, an interesting feature of CFD would be that it can properly predict trends in heat transfer and pressure drop for plate heat exchangers. With already available correlations, these trends can be verified. Therefore, future work should also focus on the prediction of trends, by CFD, in heat transfer and pressure drop in plate heat exchangers.

A

Extra information on numercial schemes

A.1. Geometric Reconstruction Scheme

The geometric reconstruction scheme adopted in Fluent was originally developed by Youngs (1998)[12]. In his method, the fluxes of volume fraction are determined using a geometric approach rather than an upwind, central or downwind difference interpolation method. Therefore, classical problems such as numerical diffusion are avoided. The *interface line* is reconstructed using data of 9 surrounding cells, as explained in Figure A.1. As can be seen in Figure A.1, the side volume fractions are deduced from

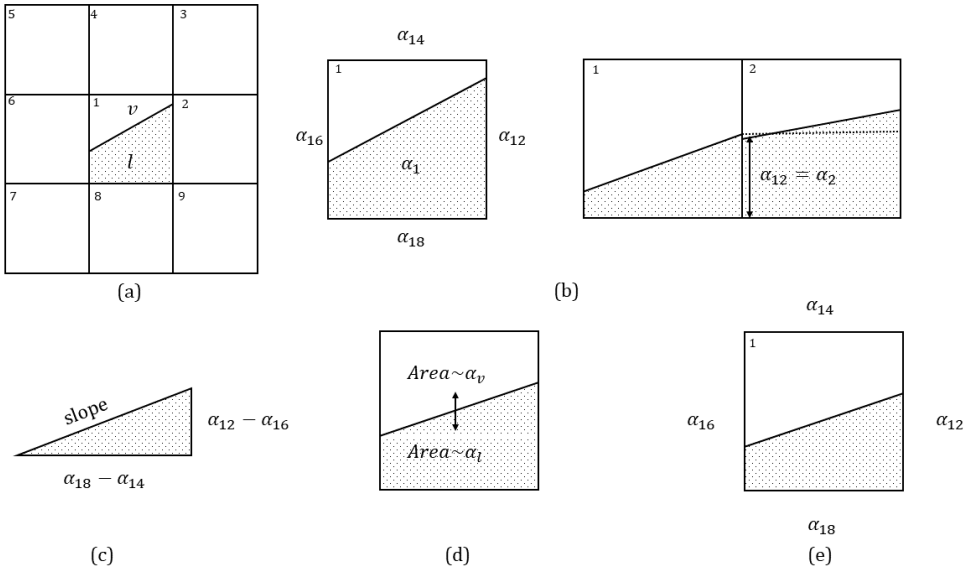

Figure A.1: (a) Cells used for reconstruction of the interface line of cell 1. (b) Side volume fractions are determined using cells 2,4,6,8. Corner cells are used to detect the interface line orientation. (c) The slope of the interface line is calculated. (d) The interface line position is altered to match respective liquid and vapor fraction. (e) Side volume fractions are known and volume fluxes can be determined. - Schematic representation adjusted from original representation of Youngs [12].

the neighbouring cells. Subsequently, using the side volume fractions, the shape and the position of the interface line is determined.

In another approach by Rider & Kothe [104], no neighbour volume fractions are needed. The interface line is reconstructed in an iterative process, using an initial guess for the interface line. Before the steps of this process will be discussed, a brief explanation of the geometric tools used in these steps will be presented. The first tool that is employed is *the line line intersection tool function*. This function

is used to find the intersection between cell edges and the interface line. *The point allocation function* is employed to determine what cell vertices lie in the considered phase. The third tool, *the polygon collection function*, collects all line segments that enclose the considered phase. Finally, *polygon area function* computes the area (in 2D) or volume (in 3D) of the polygon. Now lets define the interface line. The geometric reconstruction scheme assumes that an interface line is defined by Equation A.1.

$$\vec{n} \cdot \vec{x} + \Omega = 0 \tag{A.1}$$

Where $\vec{n}$ denotes the normal to the line segment, $\vec{x}$ represents any point on the line and Ω is the unique line constant. The interface line normal is determined using the gradient of the volume fraction according to Equation A.2.

$$\vec{n} = \frac{\nabla \alpha}{|\nabla \alpha|} \tag{A.2}$$

The iterative process starts with an initial guess for the interface line constant. Using this interface line, the mixture cell is truncated. Now the four geometric tools come into play. Together, the tools find the vertices and edges of the polygon and compute the area (2D). Subsequently the area or volume is checked with the known volume fraction. If they match, the interface line is considered reconstructed. Elsewise, a new guess for Ω is made and the procedure repeats itself. In short, the interface line constant is determined by checking volume conservation.

A.2. High Resolution Interface Capturing

For $\widetilde{\phi}_D = 1$, $\widetilde{\phi}_f$ yields 1. Therefore, the scheme can continuously switch between UDS and DDS. However, $\widetilde{\phi}_D = 0$ produces either $\widetilde{\phi}_f = 1$ or $\widetilde{\phi}_f = 0$. The arising problem is that the scheme now discontinuously switches between UDS and DDS which leads to stability issues [35]. For this reason, an alternate version of the NVD is introduced in Figure A.2, including an extra line, which defines the High Resolution Interface Capturing scheme (HRIC).

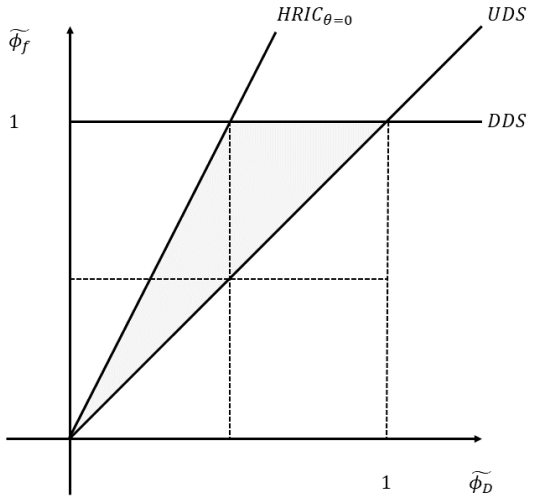

Figure A.2: Normalized Variable Diagram including HRIC scheme, grey area indicates CBC satisfaction.

The HRIC scheme was originally designed for the advection of the volume fraction by Muzaferija et al [35]. DDS may cause an artificial alignment of the liquid-vapor interface with the grid. To counter this problem, the angle θ between the normal of the interface and the cell face is included according to:

$$\widetilde{\phi}_f^* = \gamma_f \widetilde{\phi}_f + \widetilde{\phi}_D (1 - \gamma_f) \tag{A.3}$$

$$\gamma_f = \sqrt{|cos\theta|} \tag{A.4}$$

Where $\widetilde{\phi}_f^*$ represents the corrected normalized volume fraction and where γ_f is the blending factor.

Finally, to ensure continuous switching of the schemes not only in space, but also in time $\widetilde{\phi}_f^*$ is corrected with respect to the local Courant number C_f according to Equation A.5.

$$\widetilde{\phi}_f^{**} = \begin{cases} \widetilde{\phi}_f^* & \text{for } C_f < 0.3. \\ \widetilde{\phi}_D & \text{for } C_f > 0.7. \\ \widetilde{\phi}_D + (\widetilde{\phi}_f^* - \widetilde{\phi}_D)\frac{0.7-C_f}{0.7-0.3} & \text{for } 0.3 \leq C_f \leq 0.7 \end{cases} \tag{A.5}$$

A.3. Setting up the VOF model in Fluent

In the VOF model provided by FLUENT, either an explicit or implicit formulation for the volume fraction can be employed. While the implicit formulation is available for both steady and transient calculations, the explicit is only available for transient calculations. Because the implicit formulation depends on information of future time steps, it makes use of iteration. In addition, the unconditional stability allows you to use bigger time steps than with an explicit formulation. However, this will lead to less accurate results, due to numerical diffusion, and therefore first order upwind schemes should be avoided. When using the VOF model, multiple ways of interface modeling can be employed. FLUENT provides a sharp interface modeling, a dispersed interface modeling and a combination of both. Since the annular flow regime is assumed, a sharp interface between the vapor and liquid phase is expected. Therefore, the sharp interface model is chosen. When using the sharp modeling type, the option of interfacial anti-diffusion can be enabled. This option tempers the numerical diffusion originating from the volume fraction advection schemes and therefore enhances accuracy. However, using this treatment also leads to convergence problems. It is recommended by FLUENT to use the *implicit* body force formulation. This formulation will enhance convergence speed. In multiphase flows, often the body forces due to surface tension and gravity as well as the pressure gradient are large compared to the forces due to convection and viscosity. Therefore, most of the time the body forces are almost in equilibrium with the pressure gradient. Taking this partial equilibrium into account enhances convergence speed.

The explicit formulation of the volume fraction allows one to choose between five different ways of spatial discretization of the volume fraction namely: Geo-Reconstruct, CICSAM, Compressive and HRIC. The Donor-Acceptor scheme is only available by a text commend. As was pointed out earlier, these can be divided in schemes based on algebraic information and schemes based on geometrical information. In FLUENT the Geo-Reconstruct scheme is considered most accurate for reconstruction of the interface. In addition, it performs well on grids with poor quality. However, it is more computationally expensive than other volume fraction discretization schemes. Although FLUENT recommends the use of a diffusive interface discretization schemes with the Lee model (QUICK, HRIC, Phase localized Compressive scheme), many authors use the Geo-Reconstruct scheme ([38][60][10]). The Compressive Interface Capturing Scheme for Arbitrary Meshes (CICSAM) is mostly used in two-phase flows with high viscosity ratios. Also, it is able to display the interface almost as sharp as the Geo-Reconstruct scheme. Modified High Resolution Interface Capturing scheme is a scheme ,based on algebraic information, available in FLUENT for reconstruction of the interface. The faster convergence of this scheme is the main advantage compared to the Geo-Reconstruct scheme. In addition, it is more accurate than QUICK scheme and other second-order schemes. However, Geo-Reconstruct is considered to be more accurate [38]. When using the Evaporation-Condensation model in FLUENT (Lee model) with VOF, the Fluent user manual recommends to use a diffusive interface discretization scheme for the volume fraction . However, the diffusion of the interface brings other problems. Namely, surface tension modeling needs a sharp interface. When the interface is diffuse, the surface tension modeling might result in stability issues.

The Donor-Acceptor scheme is considered to be an ”out of date” scheme. However, no pros or cons are mentioned. The only limitation according to the user manual, is that it is only applicable to quad- and hexahedral meshes.

When one is interested in solving steady problems, the Bounded Gradient Maximization (BGM) scheme can be used. The yielded interface sharpness is comparable to interface produced by the Geo-Reconstruct scheme.

B

Nusselt Condensation Derivation

The theory of the vertical Nusselt condensation is taken from "Fundamentals of heat and mass transfer" by F. Incropera [9]. In order to arrive at the solution for the analytical film thickness four assumptions are made:

- The liquid film flow is laminar and the material properties of the liquid are constant throughout the film.
- The gas phase is assumed to be purely vapor. Moreover the temperature of the vapor is constant throughout the domain. So no temperature gradient is present. Energy transfer at the liquid-vapor interface is governed by condensation.
- The shear stress at the liquid-vapor interface is negligible. Together with the assumption of constant temperature in the vapor phase, the temperature and vapor boundary layer shown in Figure B.1a do not have to be considered.
- Due to the low film velocity, momentum and energy transfer by advection in the liquid film is negligible. Heat transfer only takes place through conduction in the liquid film. Therefore the temperature distribution is linear, as shown in Figure B.1b.

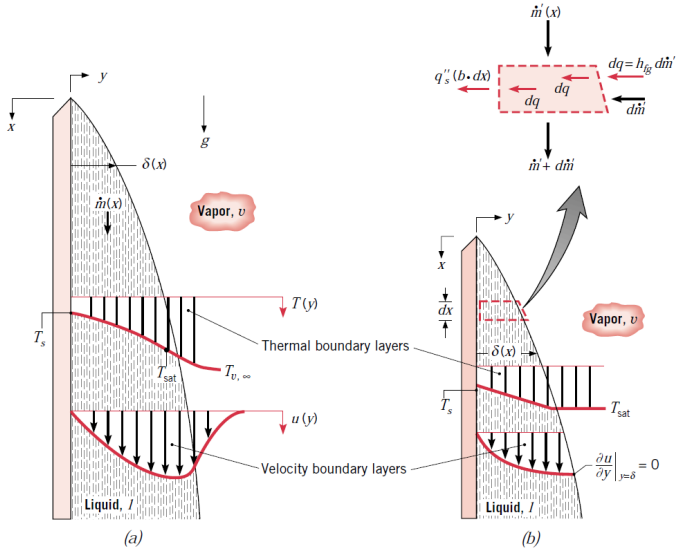

Figure B.1: Boundary layer effects in vertical film condensation without (a) assumptions, with (b) assumptions, from [9].

The laminar liquid film flow can be treated as a boundary layer flow. A boundary layer flow is assumed to be a steady two-dimensional flow of incompressible fluid with constant properties. In addition the following assumptions are made:

- The boundary layer pressure gradient in the streamwise direction $(+x)$ can be approximated as the free stream $(+x)$ pressure gradient : $\frac{\partial p}{\partial x} = \frac{dp_\infty}{dx}$
- The boundary layer (liquid film) is assumed very thin compared to the object (plate). Therefore the gradients along the plate are very small compared to the gradients normal to the plate: $\frac{\partial^2 u}{\partial x^2} << \frac{\partial^2 u}{\partial y^2}$

Now the boundary layer x-momentum equation becomes:

$$u\frac{\partial u}{\partial x} + v\frac{\partial u}{\partial y} = -\frac{1}{\rho_l}\frac{dp_\infty}{dx} + g + \nu_l\frac{\partial^2 u}{\partial y^2} \tag{B.1}$$

Where dp_∞/dx is the free stream pressure gradient in the quiescent region outside the boundary layer.
Using the fact that the velocity is zero in the vapor region the pressure gradient can be written as:

$$\frac{dp_\infty}{dx} = \rho_v g \tag{B.2}$$

The momentum advection terms can be neglected due to the low film velocity (assumption four). Now using appropriate boundary conditions the equation for the x-direction velocity profile $u(y)$ becomes:

$$\frac{\partial^2 u}{\partial y^2} = -\frac{g}{\mu_l}(\rho_l - \rho_v) \tag{B.3}$$

$$with \;\; u(0) = 0; \quad \partial u/\partial y|_{y=\delta} = 0 \tag{B.4}$$

$$u(y) = \frac{g(\rho_l - \rho_v)\delta^2}{\mu_l}\left[\frac{y}{\delta} - \frac{1}{2}\left(\frac{y}{\delta}\right)^2\right] \tag{B.5}$$

Integration of the velocity profile leads to a definition of the mass flow per unit width (b) $\Gamma(x)$:

$$\frac{\dot{m}'(x)}{b} = \int_0^{\delta(x)} \rho_l u(y) dy \tag{B.6}$$

$$\Gamma(x) = \frac{g\rho_l(\rho_l - \rho_v)\delta^3}{3\mu_l} \tag{B.7}$$

By means of an energy balance over the control volume shown in Figure B.1 the variation of Γ and hence of δ with x can be deduced. First, the rate of energy transfer into the liquid film must equal the amount of heat extracted from the vapor, i.e. the energy release due to condensation at the interface. Hence

$$dq = h_{fg} d\dot{m}' \tag{B.8}$$

Because advection is neglected the heat transfer to the surface (wall) must equal the heat transfer across the interface.

$$dq = q"_w(b \cdot dx) \tag{B.9}$$

In order to obtain the heatflux into the wall we can apply Fourier's law, since the temperature distribution in the liquid film is linear.

$$q"_w = \frac{kl(T_{sat} - T_w)}{\delta} \tag{B.10}$$

Now, combining Equation B.8, Equation B.9 and Equation B.10 leads to:

$$\frac{dm'}{b \cdot x} = \frac{k_l}{h_{fg}}\frac{T_{sat} - T_w}{\delta} = \frac{d\Gamma}{dx} \tag{B.11}$$

Next, the derivative of Γ with respect to x can be found by differentiating Equation B.7.

$$\frac{d\Gamma(x)}{dx} = \frac{g\rho_l(\rho_l - \rho_v)(\delta(x))^2}{\mu_l}\frac{d\delta(x)}{dx} \tag{B.12}$$

Finally, combining Equation B.11 and Equation B.12 and integrating with respect to x results in:

$$\delta^3 d\delta = \frac{k_l\mu_l(T_{sat} - T_w)}{g\rho_l(\rho_l - \rho_v)h_{fg}}dx \tag{B.13}$$

$$\delta(x) = \left[\frac{4k_l\mu_l(T_{sat} - T_w)x}{g\rho_l(\rho_l - \rho_v)h_{fg}}\right]^{1/4} \tag{B.14}$$

In order to account for thermal advection in the liquid film the definition of the latent heat was modified by Nusselt and Rohsenow according to

$$h'_{fg} = h_{fg} + 0.68C_{p,l}(T_{sat} - T_w) = h_{fg}(1 + 0.68Ja) \tag{B.15}$$

where Ja represents the Jacob number and is defined as the ratio of the sensible heat to the latent heat absorbed or released during the phase change process:

$$Ja = \frac{Cp(T_w - T_{sat}}{h_{fg}} \tag{B.16}$$

The local heat transfer coefficient can be expressed as

$$q"_w = h(T_{sat} - T_w) \tag{B.17}$$

Using Equation B.10 and Equation B.14 the local heat transfer coefficient can be deduced. Hence

$$h = \frac{k_l}{\delta} \tag{B.18}$$

$$h = \left[\frac{g\rho_l(\rho_l - \rho_v)k_l^3 h'_{fg}}{4\mu_l(T_{sat} - T_w)x}\right] \tag{B.19}$$

C

User Defined Functions in Fluent

The user defined subroutine environment of Fluent enables one to alter or add numerical models when needed. In this chapter a small guide based on experience is presented for the interested reader. For a full explanation of the capabilities of the UDF-environment one is referred to the Ansys Fluent UDF-manual [105].

C.1. Fluent UDF-interface

In Fluent 18.1, the UDF-environment is accessible trough the third tab in the top of the window. This is shown in Figure C.1.

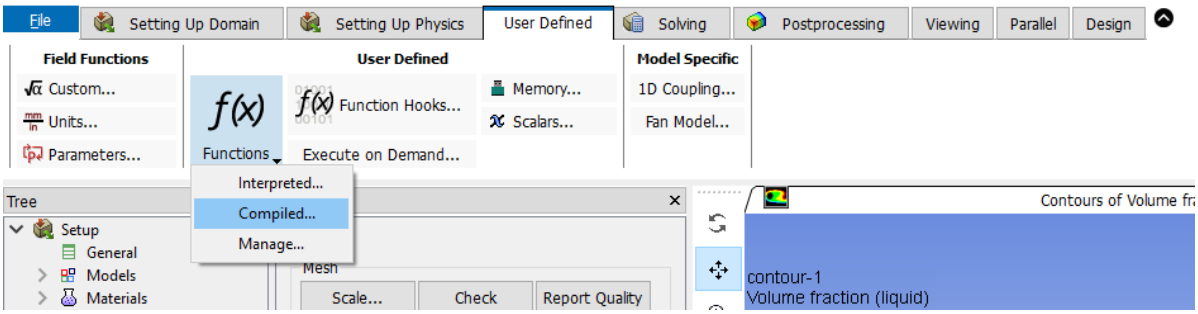

Figure C.1: Fluent's UDF interface

A user defined subroutine can either be *interpreted* or *compiled*. In practice the main advantage of interpreted UDFs over compiled UDFs is that they do not have to be compiled. Meaning no extra c-compiler is needed. However, the compiled UDFs execute faster than interpreted UDFs. This can be a major advantage when a UDF is for instance called every iteration.

For the windows platform, getting the right c-compiler can be a tedious exercise. To save you a lot of time, watch this video carefully and make sure that you use the *Microsoft visual studio 2012 professional* compiler.

Function Hooks are functions that are not directly related to flow solution itself. Using function hooks, one can for instance calculate a custom mean of every kind of variable and write it to a file. One of the most powerful function hooks is the *define adjust* general purpose macro. This macro can be used to dynamically adjust for instance flow variables or or compute integrals. The define adjust macro is called every iteration and is very convenient to use in conjunction with other UDFs. Namely, through the User Defined Memory, one is able to save the calculated data, and pass it to another UDF. Finally, the *User Defined Scalars* are used when one wants to solve a transport equation for a custom variable. In this work, for instance, the UDS subroutine was used to solve the smearing function by Hardt & Wondra [75]. By making use of the smearing function, the mass transfer intensity was smeared across several computational cells.

C.2. UDF-subroutines used in this work

The UDF-subroutines used in this work are presented in this section. The UDFs used for the Liu model and the Shen model are presented.

C.2.1. Liu - model subroutine

In the Liu model [10] the mass transfer is altered by adding an extra power to the vapor fraction term. Therefore the mass transfer has to be included trough a UDF. Before the UDF becomes accessible in the phase interaction panel, one needs to write certain text commands. These are listed below:

- solve/set/expert
- Linearized mass transfer? [yes] no
- Use alternate formulation for wall temperatures? [no]
- Save cell residuals for post-processing? [no]
- Keep temporary solver memory from being freed? [no]
- Allow selection of all applicable discretization schemes? [no]

The questions will pop up after the first expression is written in the text user interface. After completion one is now able to specify a *user-defined* mass transfer mechanism in the phase interaction panel. The code used to define the mass transfer intensity is shown in C.1.

Listing C.1: Liu c-code

```
/* UDF to define a simple mass transfer based on Saturation
   Temperature. The "from" phase is the gas and the "to" phase is the
   liquid phase.   */

#include "udf.h"
#include "math.h"

/* Define constant to account for Liu model */
#define   n 2./3.


DEFINE_MASS_TRANSFER(liq_gas_source, cell, thread, from_index, from_species_index, to_index, to_species_index)
{
   real m_lg;
   real T_SAT = 373.15;
   real r          = 5000.;
   Thread *gas = THREAD_SUB_THREAD(thread, from_index);
   Thread *liq = THREAD_SUB_THREAD(thread, to_index);

   m_lg = 0.;
   if (C_T(cell, liq) >= T_SAT)
     {
       m_lg = -r*pow(C_VOF(cell,liq),n)*C_R(cell,liq)*
              fabs(C_T(cell,liq)-T_SAT)/T_SAT;
     }
   if ((m_lg == 0. ) && (C_T(cell, gas) <= T_SAT))
     {
       m_lg = r*pow(C_VOF(cell,gas),n)*C_R(cell,gas)*
         fabs(T_SAT-C_T(cell,gas))/T_SAT;
     }
   return (m_lg);
}
```

C.2.2. Shen - model subroutine

The Shen model [6] is Incorporated in Fluent by altering the vapor thermal conductivity in the two-phase region. When the UDF is compiled one can select the user defined vapor conductivity in the materials panel. The UDF-code is shown in C.2.

Listing C.2: Shen c-code

```
/*********************************************************************
UDF for specifying a thermal conductivity. In this UDF the vapor
conductivity in the two-phase region is set to the liquid conductivity.
*********************************************************************/

#include "udf.h"


DEFINE_PROPERTY(cell_conductivity_g,cell,cell_thread)
{
       /* Variable fluid properties for water-vapor subcooling @353.15 K as defined by Mills */
    real T_SAT                                          = 373.15;
        real k_v                                                = 0.0248;
        real k_l                                                = 0.674;
        real ktc_;

        /* Enhancement factor n, as proposed by Shen. Enhances the energy transportation in the two-phase region. */
```

```
        real n                                                  = 10.;
        real gas                                                = 0.;


        /* Domain parameters */
        int                                                     phase_domain_index;
        Domain                                                  *subdomain;
    Domain                                                      *mixture_domain = Get_Domain(1);
        real temp                                               = C_T(cell,cell_thread);

        /* loop over all subdomains (phases) in the superdomain (mixture) */
    sub_domain_loop(subdomain, mixture_domain, phase_domain_index)
    {
       /* loop if primary phase  */
       if (DOMAIN_ID(subdomain) == 2)
           {
                   gas = C_VOF(cell,cell_thread);
           }

    }

        ktc_ = 0.;
        if ((temp < T_SAT) && (gas < 1.) && (gas > 0.))
        {
                ktc_ = k_l;
        }
        else
        {
                ktc_ = k_v;
        }

    return ktc_;
}
```

D

Set-up & validation condensate flow on a baffled surface

In this chapter, the set-up and validation study associated with the results presented in section 5.4 are presented. The validation refers to the work of Ishikawa [13].

D.1. Set-up

The domain, geometry and boundary conditions used in simulations of section 5.4 are schematically shown in Figure D.1. In case of a flat surface, only the baffles and the inlet platform are removed. The remaining set-up is exactly the same as in the baffled set-up. The bulk velocity referred to in Table 5.5, represent both the liquid velocity and vapor velocity. The liquid and vapor velocity are altered simultaneously in order to mitigate shear stress on the liquid film surface.

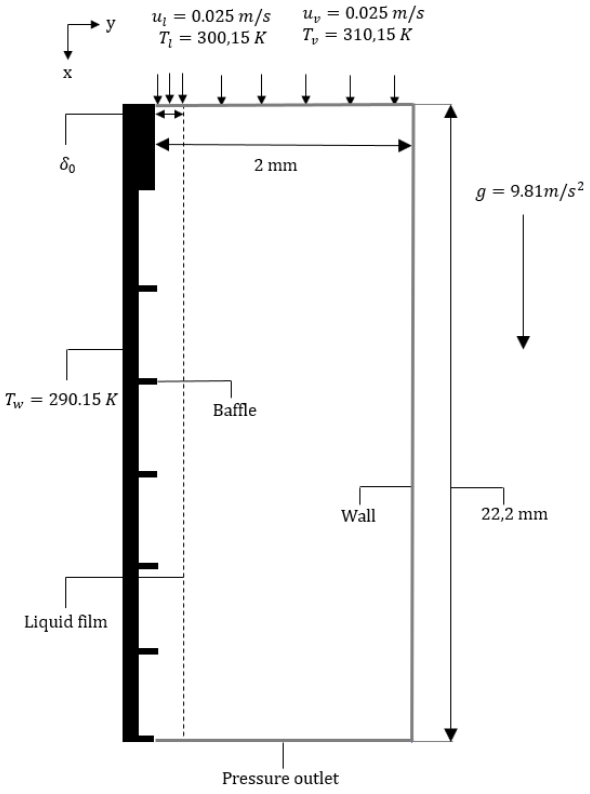

Figure D.1: Geometry, domain & boundary conditions used in simulations of section 5.4

Table D.1: Material properties (temperature related properties not used in validation study)

Methanol-liquid	
Density	$\rho = 785\ kg/m^3$
Specific heat	$C_p = 2483\ J/kg - K$
Thermal conductivity	$k = 0.203\ W/m - K$
Dynamic viscosity	$\mu = 0.00055\ kg/m - s$
Molecular Weight	$W = 32.032\ kg/kmol$
Standard State Enthalpy	$H = 0\ J/kg - mol$
Reference temperature	$T = 310.15\ K$
Methanol-vapor	
Density	$\rho = 0.47\ kg/m^3$
Specific heat	$C_p = 1490\ J/kg - K$
Thermal conductivity	$k = 0.00154\ W/m - K$
Dynamic viscosity	$\mu = 0.00001\ kg/m - s$
Molecular Weight	$W = 32.032\ kg/kmol$
Standard State Enthalpy	$H = 3.765496 \cdot 10^7\ J/kg - mol$
Reference temperature	$T = 310.15\ K$

Table D.2: Model Set-Up (condensation parameters not used in validation study)

General	
Pressure based, transient, 2D	
Multiphase VOF, Viscous Laminar, Energy On	
Multiphase model	
VOF	
Volume Fraction Parameters Formulation	Explicit
Volume Fraction Cuttof	1e-6
Courant Number	0.25
Body Force Formulation	Implicit Body Force
Interface Modeling	Sharp
Phase change parameters	
Phase Change model	Lee model & Shen model
Condensation coefficient	$r = 50000\ s^{-1}$
Surface tension model	Continuum Surface Force
Surface tension coefficient	$\sigma = 0.022\ n/m$
Solution Methods	
Pressure velocity coupling	
Scheme	PISO
Skewness Correction	1
Neighbor Correction	1
Skewness-Neighbor Coupling	On
Spatial Discretization	
Gradient	Least Square Cell Based
Pressure	PRESTO!
Momentum	QUICK
Volume Fraction	Geo-Reconstruct
Energy	QUICK
Transient Formulation	First Order Implicit
Under Relaxation	
Pressure	0.3
Density	1
Body Forces	1
Momentum	0.7
Vaporization Mass	1
Energy	1
Run calculation	
Fixed time step	$5 \cdot 10^{-6} s$
Max Iterations/Time Step	200

D.2. Validation

Figure D.2 shows the original figure of the film evolution in time by Ishikawa. The corresponding validation study results are depicted in Figure D.3. The film evolution in both figures agree very well. Only the outflow region differentiates from one another. This can be attributed to the different outflow boundary condition used. Where Ishikawa has used an outflow boundary condition, in this work a pressure outlet was chosen to represent the outflow boundary. Nevertheless, the remaining part of the figure agrees sufficiently to the work of Ishikawa to conclude that the solution is validated. In both Figure D.2 and Figure D.3 the contact angle between the phases was 10 degrees. Ishikawa has shown in his work that the wavy film flow is independent of contact angle.

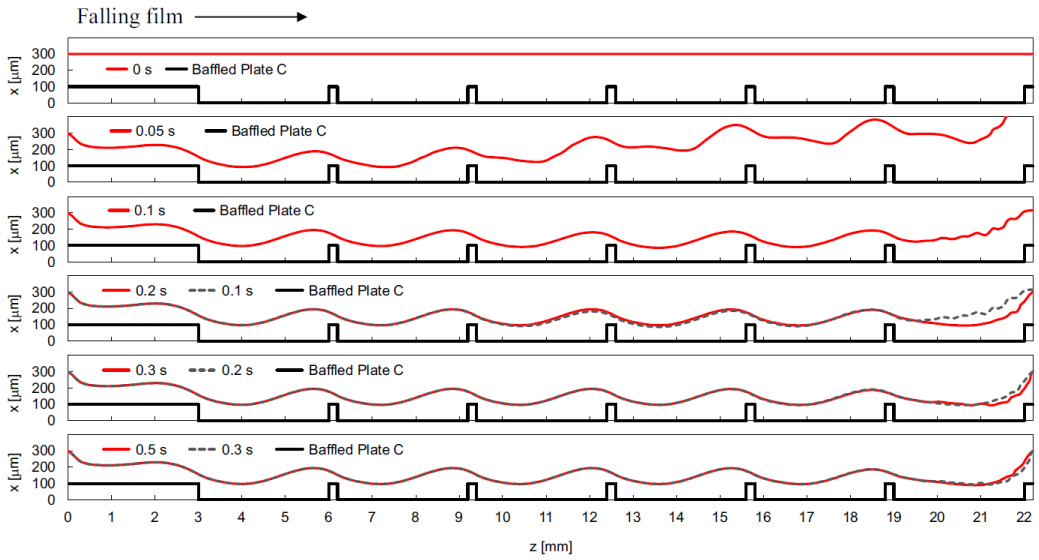

Figure D.2: Original film evolution in time by Ishikawa [13]

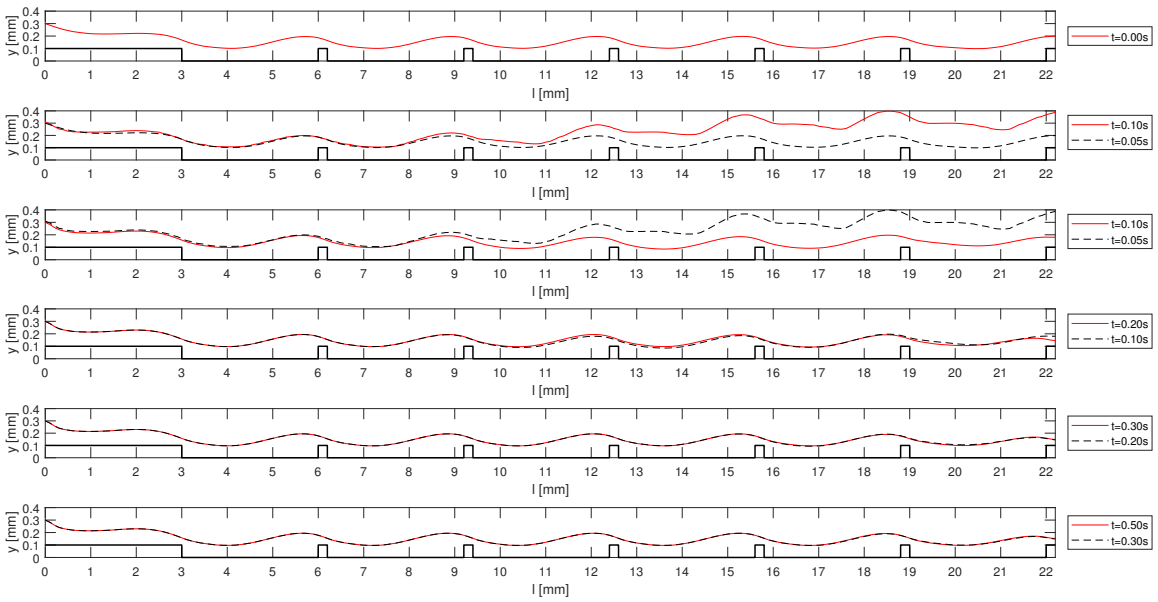

Figure D.3: Film evolution in time from this work

Bibliography

[1] Bluerise, *Schematic of ocean thermal energy conversion working principle,* (2014).

[2] G. F. H. George Yadigaroglu, *Introduction to Multiphase Flow: Basic Concepts, Applications and Modelling* (Springer, 2017).

[3] ANSYS®, *Academic Research Mechanical, Release 18.1, Fluent Theory Guide*, ANSYS, Inc.

[4] B. Andersson, R. Andersson, L. Håkansson, M. Mortensen, R. Sudiyo, and B. van Wachem, *Computational Fluid Dynamics for Engineers* (Cambridge University Press, 2011).

[5] P. Sharma, *Thermodynamics of liquid-vapor phase change processes,* (2006).

[6] Q. Shen, D. Sun, S. Su, N. Zhang, and T. Jin, *Development of heat and mass transfer model for condensation,* International Communications in Heat and Mass Transfer (2017), 10.1016/j.icheatmasstransfer.2017.03.009.

[7] A. S. Rattner and S. Garimella, *Simple Mechanistically Consistent Formulation for Volume-of-Fluid Based Computations of Condensing Flows,* Journal of Heat Transfer (2014), 10.1115/1.4026808.

[8] H. Ganapathy, A. Shooshtari, K. Choo, S. Dessiatoun, M. Alshehhi, and M. Ohadi, *Volume of fluid-based numerical modeling of condensation heat transfer and fluid flow characteristics in microchannels,* International Journal of Heat and Mass Transfer (2013), 10.1016/j.ijheatmasstransfer.2013.05.044.

[9] F. Incropera, *Fundamentals of heat and mass transfer*, Fundamentals of Heat and Mass Transfer No. v. 1 (John Wiley, 2007).

[10] W. Q. H. G. . M. L. Quan Liu, Jianzhi Yang, *Numerical study of the forced convective condensation on a short vertical plate,* Heat Transfer Engineering (2016).

[11] A. Miyara, *Flow Dynamics and Heat Transfer of Wavy Condensate Film,* Journal of Heat Transfer (2001), 10.1115/1.1370522.

[12] D. Youngs and D. L. Youngs, *Time-Dependent Multi-material Flow with Large Fluid Distortion,* .

[13] H. Ishikawa, S. Ookawara, and S. Yoshikawa, *A study of wavy falling film flow on micro-baffled plate,* Chemical Engineering Science (2016), 10.1016/j.ces.2016.04.021.

[14] R. Marek and J. Straub, *Analysis of the evaporation coefficient and the condensation coefficient of water, International Journal of Heat and Mass Transfer*, **44** (2001).

[15] B. J. Kleute, *System sensitivity and cold water pipe analysis of a 10MW Offshore OTEC-Ocean Thermal Energy Conversion plant,* (2014).

[16] J. Kirkenier, *Techno-economic optimization ofOrganic Rankine Cycles usingworking fluid mixtures for 10 to25 MW OTEC power plants*, Master's thesis, TU Delft (2014).

[17] S. Kakaç, H. Liu, and A. Pramuanjaroenkij, *Heat Exchangers: Selection, Rating, and Thermal Design, Third Edition* (Taylor & Francis, 2012).

[18] R. Sinnott and G. Towler, *Chemical Engineering Design: SI edition*, Chemical Engineering Series (Elsevier Science, 2009).

[19] H. D. Madhawa Hettiarachchi, M. Golubovic, W. M. Worek, and Y. Ikegami, *Optimum design criteria for an Organic Rankine cycle using low-temperature geothermal heat sources,* Energy (2007), 10.1016/j.energy.2007.01.005.

[20] J. R. García-Cascales, F. Vera-García, J. M. Corberán-Salvador, and J. Gonzálvez-Maciá, *Assessment of boiling and condensation heat transfer correlations in the modelling of plate heat exchangers,* International Journal of Refrigeration (2007), 10.1016/j.ijrefrig.2007.01.004.

[21] J. R. Thome, *Engineering Data Book III* (Wolverine Tube inc., 2004-2010).

[22] W. J and S. Y. KANG, *Flow pattern transitions in vertical and upwardly inclined lines,* Int, J. MultiphaseFlow **7**, 271 (1981).

[23] J. W. T. J. CRAWFORD, C. B. WEINBERGER, *Two-phase flow patterns and void fractions in downward flow part i: Steady-state flow patterns,* Int, J, Multiphase Flow **11**, 761 (1985).

[24] J. S. Junli Gou, Baojing Wang, *Development of an analytical model for pure vapor downflow condensation in a vertical tube,* Nuclear Engineering and Design **320**, 346 (2017).

[25] W. W. FOCKE and P. G. KNIBBE, *Flow visualization in parallel-plate ducts with corrugated walls,* J. Fluid Mech. **165**, 73 (1986).

[26] G. . Kottke, *Flow phenomena and local heat and mass transfer in corrugated passages,* Chem. Eng. Technol. **12**, 400 (1989).

[27] M. G. . M. Lebouché, *Two-phase gas-liquid flow in horizontal corrugated channels,* International Journal of Multiphase Flow **26**, 435 (2000).

[28] C. Tribbe and H. M. Müller-Steinhagen, *Gas/liquid flow in plate-and-frame heat exchangers - Part II: Two-phase multiplier and flow pattern analysis,* Heat Transfer Engineering (2001), 10.1080/01457630150215686.

[29] X. Tao, M. P. Nuijten, and C. A. I. Ferreira, *Two-phase vertical downward flow in plate heat exchangers: Flow patterns and condensation mechanisms,* International Journal of Refrigeration **85**, 489 (2018).

[30] ANSYS®, *Academic Research Mechanical, Release 18.1, Fluent User's Guide*, ANSYS, Inc.

[31] A. Mills and P. Education, *Basic Heat and Mass Transfer: Pearson New International Edition*, Always Learning (Pearson Education, Limited, 2014).

[32] A. PROSPERETTI and G. TRYGGVASON, *COMPUTATIONAL METHODS FOR MULTIPHASE FLOW* (Cambridge University Press, 2007).

[33] C. W. Hirt and B. D. Nichols, *Volume of fluid (VOF) method for the dynamics of free boundaries,* Journal of Computational Physics (1981), 10.1016/0021-9991(81)90145-5.

[34] O. Ubbink and R. I. Issa, *A Method for Capturing Sharp Fluid Interfaces on Arbitrary Meshes,* Journal of Computational Physics **153**, 26 (1999).

[35] P. T. S.Muzaferija, M.Peric, *A two-fluid navier-stokes solver to simulate water entry,* in *Twenty-Second Symposium on Naval Hydrodynamics* (1999).

[36] C. Hirsch, *Chapter 8 - general properties and high-resolution numerical schemes,* in *Numerical Computation of Internal and External Flows (Second Edition)*, edited by C. Hirsch (Butterworth-Heinemann, Oxford, 2007) second edition ed., pp. 337 – 409.

[37] B. P. Leonard, *Simple high□accuracy resolution program for convective modelling of discontinuities,* International Journal for Numerical Methods in Fluids (1988), 10.1002/fld.1650081013.

[38] Z. Liu, B. Sunden, and J. Yuan, *VOF MODELING AND ANALYSIS OF FILMWISE CONDENSATION BETWEEN VERTICAL PARALLEL PLATES,* Heat Transfer Research (2012), 10.1615/HeatTransRes.2012004376.

[39] J. U. Brackbill, D. B. Kothe, and C. Zemach, *A Continuum Method for Modeling Surface Tension*,* JOURNAL OF COMPUTATIONAL PHYSICS **100**, 335354 (1992).

[40] B. Lafaurie, C. Nardone, R. Scardovelli, S. Zaleski, and G. Zanetti, *Modelling merging and fragmentation in multiphase flows with surfer,* Journal of Computational Physics **113**, 134 (1994).

[41] C. R. Kharangate and I. Mudawar, *Review of computational studies on boiling and condensation,* (2017).

[42] A. Faghri and Y. Zhang, *Transport Phenomena in Multiphase Systems* (Academic Press, 2006).

[43] H. E. Mghari, M. Asbik, H. Louahlia-Gualous, and I. Voicu, *Condensation heat transfer enhancement in a horizontal non-circular microchannel Rectangular microchannel 375x187.5μm² square microchannel 250x250μm²,* (2014), 10.1016/j.applthermaleng.2013.12.003.

[44] B. A. Nichita and J. R. Thome, *A level set method and a heat transfer model implemented into FLUENT for modeling of microscale two phase flows,* .

[45] D. L. Sun, J. L. Xu, and L. Wang, *Development of a vapor-liquid phase change model for volume-of-fluid method in FLUENT,* International Communications in Heat and Mass Transfer (2012), 10.1016/j.icheatmasstransfer.2012.07.020.

[46] P. Rahimi, *Kinetics of evaporation: Statistical rate approach,* Int. J. of Thermodynamics **8**, 1 (2005).

[47] J. B. Young, *The condensation and evaporation of liquid droplets at arbitrary Knudsen number in the presence of an inert gas,* International Journal of Heat and Mass Transfer (1993), 10.1016/0017-9310(93)90112-J.

[48] R. Schrage, *A theoretical study of interphase mass transfer* (Columbia University Press, 1953).

[49] I. Tanasawa, *Advances in Condensation Heat Transfer*, Vol. 21 (Advances in Heat Transfer, 1991).

[50] J. Barrett and C. Clement, *Kinetic evaporation and condensation rates and their coefficients,* Journal of Colloid And Interface Science (1992), 10.1016/0021-9797(92)90205-Z.

[51] L. Berman, *Interface resistance in film condensation of low pressure steam,* Trudy Vsesojusnyj NaucÏno-Issledovatel'skii i Konstruktorskij Institut ChimicÏeskogo MasÏinostro- enija, Moskva, **36**, 66 (1961).

[52] L. B. K. Nabavian, *Condensation coefficient of water,* Chemical Engineering Science **18**, 651 (1963).

[53] R. S. A.F. Mills, *The condensation coefficient of water,* International Journal of Heat & Mass Transfer **10** (1967).

[54] D. P. D. W. D.W. Tanner, C.J. Potter, *Heat transfer in dropwise condensation at low steam pressures in the absence and presence of non-condensable gas,* International Journal of Heat & Mass Transfer **11**, 181 (1968).

[55] H. Wenzel, *On the condensation coefficient of water estimated from heat-transfer measurements during dropwise condensation,* International Journal of Heat & Mass Transfer **12**, 125 (1696).

[56] H. T. S. Hatamiya, *Drop-size distributions and heat transfer in dropwise condensation - condensation coefficient of water at low pressures,* Proceedings of the 8th International Heat Transfer Conference **4**, 1671 (1986).

[57] S. C. De Schepper, G. J. Heynderickx, and G. B. Marin, *Modeling the evaporation of a hydrocarbon feedstock in the convection section of a steam cracker,* Computers and Chemical Engineering (2009), 10.1016/j.compchemeng.2008.07.013.

[58] W. H. Lee, *Pressure iteration scheme for two-phase flow modeling,* IN" MULTIPHASE TRANSPORT: FUNDAMENTALS, REACTOR SAFETY, APPLICATIONS". , 407 (1980).

[59] E. D. Riva and D. Del Col, *Numerical Simulation of Condensation in a Minichannel,* .

[60] H. Lee, C. R. Kharangate, N. Mascarenhas, I. Park, and I. Mudawar, *Experimental and computational investigation of vertical downflow condensation,* International Journal of Heat and Mass Transfer (2015), 10.1016/j.ijheatmasstransfer.2015.02.037.

[61] G. D. Qiu, W. H. Cai, Z. Y. Wu, Y. Yao, and Y. Q. Jiang, *Numerical Simulation of Forced Convective Condensation of Propane in a Spiral Tube,* Journal of Heat Transfer (2015), 10.1115/1.4029475.

[62] A. Alizadehdakhel, M. Rahimi, and A. A. Alsairafi, *CFD modeling of flow and heat transfer in a thermosyphon,* International Communications in Heat and Mass Transfer (2010), 10.1016/j.icheatmasstransfer.2009.09.002.

[63] E. Da Riva, D. Del Col, A. Cavallini, S. Garimella, E. Da, and D. Del, *Simulation of condensation in a circular minichannel: Application of vof method and turbulence model,* (2010).

[64] E. Da Riva and D. Del Col, *Effect of gravity during condensation of R134a in a circular minichannel: VOF simulation of annular condensation,* Microgravity Science and Technology (2011), 10.1007/s12217-011-9275-4.

[65] E. Da Riva, D. Del Col, S. V. Garimella, and A. Cavallini, *The importance of turbulence during condensation in a horizontal circular minichannel,* International Journal of Heat and Mass Transfer (2012), 10.1016/j.ijheatmasstransfer.2012.02.026.

[66] S. Bortolin, E. Da Riva, and D. Del Col, *Condensation in a square minichannel: Application of the VOF method,* in *Heat Transfer Engineering* (2014).

[67] G. D. Qiu, W. H. Cai, S. L. Li, Z. Y. Wu, Y. Q. Jiang, and Y. Yao, *Numerical simulation on forced convective condensation of steam upward flow in a vertical pipe,* Advances in Mechanical Engineering (2014), 10.1155/2014/589250.

[68] S. Chen, Z. Yang, Y. Duan, Y. Chen, and D. Wu, *Simulation of condensation flow in a rectangular microchannel,* Chemical Engineering and Processing: Process Intensification (2014), 10.1016/j.cep.2013.12.004.

[69] Z. Yin, Y. Guo, B. Sunden, Q. Wang, and M. Zeng, *Numerical simulation of laminar film condensation in a horizontal minitube with and without non-condensable gas by the VOF method,* Numerical Heat Transfer; Part A: Applications (2015), 10.1080/10407782.2015.1023143.

[70] J. Zhang, W. Li, and S. A. Sherif, *A numerical study of condensation heat transfer and pressure drop in horizontal round and flattened minichannels,* International Journal of Thermal Sciences (2016), 10.1016/j.ijthermalsci.2016.02.019.

[71] J. Zhang and W. Li, *Numerical study on heat transfer and pressure drop characteristics of R410A condensation in horizontal circular mini/micro-tubes,* Canadian Journal of Chemical Engineering (2016), 10.1002/cjce.22554.

[72] C. R. Kharangate, H. Lee, I. Park, and I. Mudawar, *Experimental and computational investigation of vertical upflow condensation in a circular tube,* International Journal of Heat and Mass Transfer (2016), 10.1016/j.ijheatmasstransfer.2015.11.010.

[73] Z. Ke, J. Shi, B. Zhang, and C. L. Chen, *Numerical investigation of condensation on microstructured surface with wettability patterns,* International Journal of Heat and Mass Transfer (2017), 10.1016/j.ijheatmasstransfer.2017.08.121.

[74] R. Szijártó, A. Badillo, B. Ničeno, and H. M. Prasser, *Condensation models for the water–steam interface and the volume of fluid method,* International Journal of Multiphase Flow (2017), 10.1016/j.ijmultiphaseflow.2017.04.002.

[75] S. Hardt and F. Wondra, *Evaporation model for interfacial flows based on a continuum-field representation of the source terms,* Journal of Computational Physics (2008), 10.1016/j.jcp.2008.02.020.

[76] A. Badillo, *Quantitative phase-field modeling for boiling phenomena,* Physical Review E - Statistical, Nonlinear, and Soft Matter Physics (2012), 10.1103/PhysRevE.86.041603.

[77] J.-D. L. Huali Cao, *Computational Fluid Dynamics Simulations of Convective Pure Vapor Condensation Inside Vertical Cylindrical Condensers,* Journal of Heat Transfer (2017), 10.1115/1.4035711.

[78] Y. Zhang, A. Faghri, and M. B. Shafii, *Capillary Blocking in Forced Convective Condensation in Horizontal Miniature Channels,* Journal of Heat Transfer (2001), 10.1115/1.1351808.

[79] J. Yuan, C. Wilhelmsson, and B. Sundén, *Analysis of water condensation and two-phase flow in a channel relevant for plate heat exchangers,* in *WIT Transactions on Engineering Sciences* (2006).

[80] S. Nebuloni and J. R. Thome, *Numerical modeling of laminar annular film condensation for different channel shapes,* International Journal of Heat and Mass Transfer (2010), 10.1016/j.ijheatmasstransfer.2010.02.054.

[81] D. Sun, J. Xu, and Q. Chen, *Modeling of the evaporation and condensation phase-change problems with FLUENT,* Numerical Heat Transfer, Part B: Fundamentals (2014), 10.1080/10407790.2014.915681.

[82] N. Samkhaniani and M. R. Ansari, *Numerical simulation of bubble condensation using CF-VOF,* Progress in Nuclear Energy (2016), 10.1016/j.pnucene.2016.02.004.

[83] P. Datta, A. Chakravarty, K. Ghosh, A. Mukhopadhyay, and S. Sen, *Modeling aspects of vapor bubble condensation in subcooled liquid using the VOF approach,* Numerical Heat Transfer; Part A: Applications (2017), 10.1080/10407782.2017.1372673.

[84] S. E. D. Fertahi, T. Bouhal, Y. Agrouaz, T. Kousksou, T. El Rhafiki, and Y. Zeraouli, *Performance optimization of a two-phase closed thermosyphon through CFD numerical simulations,* Applied Thermal Engineering (2018), 10.1016/j.applthermaleng.2017.09.049.

[85] W. Nusselft, *Die oberthachenkondensation des wasserdampfes,* Z. Ver. Dt. Ing. , 541 (1916).

[86] V. E. Denny and A. F. Mills, *Nonsimilar solutions for laminar film condensation on a vertical surface,* International Journal of Heat and Mass Transfer (1969), 10.1016/0017-9310(69)90158-6.

[87] M. Aissa, *GPU-accelerated CFD Simulations for Turbomachinery Design Optimization,* 10.4233/uuid:1fcc6ab4-daf5-416d-819a-2a7b0594c369.

[88] V. Patnaik and H. Perez-Blanco, *Roll waves in falling films: An approximate treatment of the velocity field,* International Journal of Heat and Fluid Flow (1996), 10.1016/0142-727X(95)00075-2.

[89] E. Stuhltrager, *Flow dynamics and heat transfer of a condensate film on a vertical wall-I. Numerical analysis and flow dynamics,* **36**, 1677 (1993).

[90] E. Stuhlträger, A. Miyara, and H. Uehara, *Flow dynamics and heat transfer of a condensate film on a vertical wall—ii. flow dynamics and heat transfer,* International Journal of Heat and Mass Transfer **38**, 2715 (1995).

[91] S. Jayanti and G. F. Hewitt, *Hydrodynamics and heat transfer of wavy thin film flow,* International Journal of Heat and Mass Transfer (1996), 10.1016/S0017-9310(96)00016-6.

[92] A. Miyara, *Numerical analysis on flow dynamics and heat transfer of falling liquid films with interfacial waves,* Heat and Mass Transfer **35**, 298 (1999).

[93] L. Phan and A. Narain, *Nonlinear Stability of the Classical Nusselt Problem of Film Condensation and Wave Effects,* Journal of Applied Mechanics (2007), 10.1115/1.2198249.

[94] A. Miyara, *Numerical simulation of wavy liquid film flowing down on a vertical wall and an inclined wall,* International Journal of Thermal Sciences (2000), 10.1016/S1290-0729(00)01192-3.

[95] J. A. F.P. Stainthorp, *The development of ripples on the surface of liquid film flowing inside a vertical tube,* TRANS. INSTN. CHEM. ENGRS. **43** (1965).

[96] T. Nosoko, P. N. Yoshimura, T. Nagata, and K. Oyakawa, *Characteristics of two-dimensional waves on a falling liquid film,* Chemical Engineering Science (1996), 10.1016/0009-2509(95)00292-8.

[97] T. Kunugi and C. Kino, *DNS of falling film structure and heat transfer via MARS method,* Computers and Structures (2005), 10.1016/j.compstruc.2004.08.018.

[98] S. P. Aktershev and S. V. Alekseenko, *Nonlinear waves and heat transfer in a falling film of condensate,* Physics of Fluids (2013), 10.1063/1.4816644.

[99] D. Gao, N. B. Morley, and V. Dhir, *Numerical simulation of wavy falling film flow using VOF method,* Journal of Computational Physics (2003), 10.1016/j.jcp.2003.07.013.

[100] M. D. Savage, *Wave flow of liquid films. by s. v. alekseenko, v. e. nakoryakov & b. g. pokusaev. begell, 1994. 313 pp. isbn 1567800 0215.* Journal of Fluid Mechanics **363**, 348–349 (1998).

[101] V. V. Lel, F. Al-Sibai, A. Leefken, and U. Renz, *Local thickness and wave velocity measurement of wavy films with a chromatic confocal imaging method and a fluorescence intensity technique,* Experiments in Fluids **39**, 856 (2005).

[102] K. Argyriadi, M. Vlachogiannis, and V. Bontozoglou, *Experimental study of inclined film flow along periodic corrugations: The effect of wall steepness,* Physics of Fluids (2006), 10.1063/1.2163810.

[103] A. Leefken, P. Adomeit, and U. Renz, *Experimental and numerical investigations on wavy films,* (2000).

[104] W. J. Rider and D. B. Kothe, *Reconstructing Volume Tracking,* Journal of Computational Physics (1998), 10.1006/jcph.1998.5906.

[105] A. Inc., *ANSYS FLUENT UDF Manual*, Vol. Release 14.0 (ANSYS, Inc., 2011).